MEASUREMENT AND NUMERICAL SIMULATION OF HIGH TEMPERATURE LASER MATERIAL PROCESSING

by

Joonghan Shin

A dissertation submitted in partial fulfillment
of the requirements for the degree of
Doctor of Philosophy
(Mechanical Engineering)
in The University of Michigan
2010

Doctoral Committee:

Professor Jyotirmoy Mazumder, Chair
Professor Amit K.Ghosh
Professor Elijah Kannatey-Asibu, Jr.
Professor Ann Marie Sastry
Magdi N. Azer, GE Global Research

To my family

ACKNOWLEDGEMENTS

First and foremost, I wish to express my deepest thanks to my advisor, Professor Jyotrimoy Mazumder, for his inspiration, encouragement, and support for my doctoral study. His expertise and guidance throughout my entire study enabled this work.

I also truly appreciate my dissertation committee, Professor Amit K. Ghosh, Professor Elijah Kannatey-Asibu, Jr., Professor Ann Marie Sastry, and Dr. Magdi N. Azer. Their insights and critiques helped improve this dissertation.

I would like to express thanks to Dr. Magdi N. Azer from the GE Global Research and Dr. Todd Rockstroh from the GE Aviation for the continued financial support for this research. I also appreciate their valuable comments for my dissertation.

I would like to thank past and present CLAIM members whom I have had worthy discussions, encouragement, insight, and friendship.

Finally, I would like to express my heartfelt thanks to my parent and grandmother for their unconditional love and endless support throughout my life. I also thank my brother, sister, sister-in-law, and brother-in-law for their constant encouragement and guidance.

TABLE OF CONTENTS

LIST OF FIGURES

LIST OF TABLES

LIST OF APPENDICES

ABSTRACT

This research investigates high temperature laser material processing, focusing on the applications for the aerospace industry. This study looks at three representative processes with three different interactions of plasma: 1) pulsed laser deposition (PLD) process for thin coating deposition where material deposit occurs via plasma and vapor, 2) drilling process for material removal to create shaped holes for efficient cooling and 3) direct metal deposition (DMD) process (very weak plasma) to clad a thick layer.

In this study, thin coatings for two important turbine blade materials were produced by the PLD technique. Yttria-stabilized zirconia films produced by the PLD were very smooth and dense. The target stoichiometry was well preserved in films. The PLD technique was also used to deposit single crystal (SC) Ni-base superalloys on the substrates of the same material. The homoepitaxial growth of the SC Ni-base superalloy film was successfully obtained without re-melting of the substrate by the PLD process.

Laser drilling experiments were carried out to generate cooling holes in an aerospace material, Inconel 718. The effect of the process parameters and different drilling methods on the hole qualities were comprehensively investigated. Using both the helical drilling technique at a high duty ratio (10 %) and O_2 assist gas produces the best drilling performance under the acceptable drilling time (~5 s) for the industrial application. In this

study, a numerical simulation for pulsed laser drilling was also carried out to provide the fundamental understanding of the high power density laser process and to investigate the effect of pulse format on the drilling performance. It was found that a modulated beam using a short pulse width and a high beam intensity yielded better drilling performance than the conventional pulsed laser under the same average power.

Spectroscopic studies during laser drilling and DMD were carried out for the purpose of process diagnostics by employing the optical emission spectroscopy. The results indicate that plasma parameters can be used to monitor the drilling depth during laser drilling and the elemental composition created during the DMD.

CHAPTER 1

INTRODUCTION

1.1 Background

1.1.1 An overview of laser processing

A LASER (an acronym for Light Amplification by Stimulated Emission of Radiation) is a device which produces amplified light. The main characteristics of a laser are: (1) monochromaticity (single color or wavelength), (2) coherence (identical frequency and phase), and (3) directionality (single direction within a narrow divergence). In order to achieve the above conditions, a laser must have three basic components. These are an active medium (a means to amplify light), a pumping source (a means to excite the active medium to an excited state), and an optical resonator (a means to provide optical feedback). Depending on the active medium, lasers can be categorized as solid, semiconductor (diode), liquid, or gas lasers. Table 1.1 shows examples of commonly used industrial lasers.

Since the invention of the first working laser based on ruby (May 16th, 1960, Hughes Research Laboratories) [1], it has become an important tool in manufacturing industries as it continues to replace many conventional manufacturing processes. Figure 1.1 shows

Table 1.1 Classification of commonly used industrial lasers [2].

Active medium	Laser type	Operation wavelength (μ m)
Solid	Ruby	0.693
	Ti: sapphire	0.7 – 1.1
	Nd: silicate glass	1.06
	Nd: yttrium-aluminum-garnet (YAG)	1.064
Semiconductor (Diode)	Semiconductor (InGaP family)	0.549-0.763
	Semiconductor (GaAlAs family)	0.636-0.8562
	Semiconductor (InGaAsP family)	1.27-1.55
Liquid	Dye	0.40 – 0.48 (Stilbene 3) 0.57 – 0.65 (Rhodamine 6G)
Gas	N_2	0.3371
	Ar ion	0.351 – 0.5287
	Excimer (KrF, XeCl)	0.248 (KrF), 0.308 (XeCl)
	CO_2	10.6

an approximate distribution of laser-based processes employed in manufacturing industries.

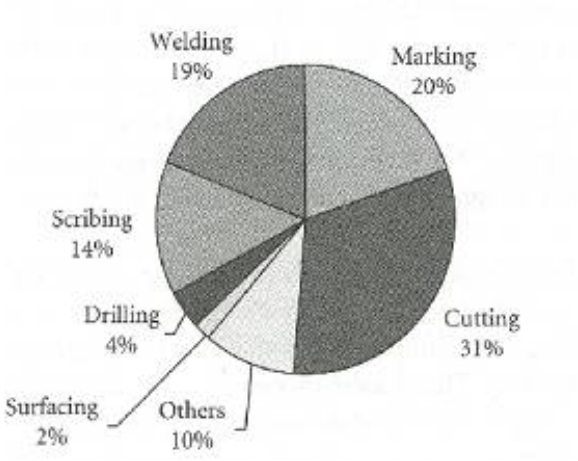

Figure 1.1: Industrial application of laser-based processes at the turn of the millennium (based on volume) [3].

The several common advantages of the laser processing are: (1) non-contact process, (2) processing of difficult-to-machine materials (i.e. brittle or hard materials), (3) flexible process (easy to automate and integrate), (3) high reproducibility, and (4) high processing speed and low operation cost. The above advantages make manufactures continue to seek and extend laser applications in diverse manufacturing processes.

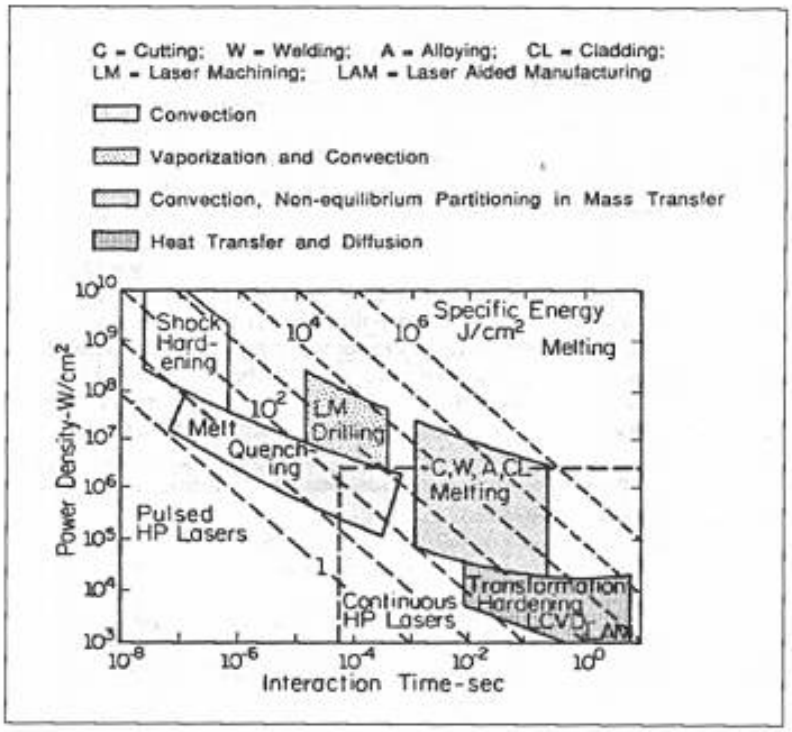

Figure 1.2: Operational regimes and associated transport phenomena for various processing techniques. [4].

Figure 1.2 shows various laser processing regimes as a function of power density and interaction time. A laser can be used for surface heat treatment to enhance surface hardness with minimal thermal distortion of the workpiece. It is also used for cladding and welding processes to deposit and join materials. With high power density and relatively short interaction time, the laser can be used to remove materials by cutting or

drilling via rapid vaporization and melt ejection. Thus, depending on the power density and interaction time, a single laser can perform various processes. This is one of the main reasons why lasers can be flexible machine tools in manufacturing systems.

1.1.2 Laser processes covered in this study

This research investigates high temperature laser processes with three different power density levels:1) pulsed laser deposition (> 10^8 W/cm^2) for thin coating deposition with a high peak power UV laser, 2) pulsed laser drilling (> 10^6 W/cm^2) for cooling hole generation with a diode pumped solid state Nd:YAG laser (DPSSL), and 3) direct metal deposition (> 10^5 W/cm^2) to clad a thick layer with a continuous wave (CW) CO_2 laser. A brief introduction of the laser processes covered in this research will be presented in the following sections.

1.1.2.1 Pulsed laser deposition (PLD)

Since the pioneering work led by Dijkkamp [5], the PLD technique has been intensively developed by the advent of a new laser technology and by the successful application in thin film deposition of a new class material. This process uses a laser ablation technique, which uses a high power density laser to ablate the coating material from a target, and deposit it on the surface to be coated. The target and a substrate holder are housed in a vacuum chamber. A motor-worm gear assembly is used to continually give a fresh target surface by providing a translational and rotational motion of the target during the ablation process. Alternately, a set of optical components can be used to focus

and raster a laser beam over the target surface. Figure 1.3 shows a schematic diagram of the PLD process.

Compared to other coating processes such as chemical vapor deposition (CVD) [6, 7], plasma-spray [8, 9], sol-gel synthesis [10], ion-beam-assisted deposition [11-13], and R.F. sputtering [14, 15], the pulsed laser deposition (PLD) [16-19] has been noted as an attractive method for creating thin coatings due to congruent evaporation (the tendency of the coatings to have the same stoichiometry as the material that serves as the target), the ease of process and its cost effectiveness. In addition, the decoupling of the vacuum system and the laser makes this technique so flexible that it is easily adaptable to different operational modes without constraints [20].

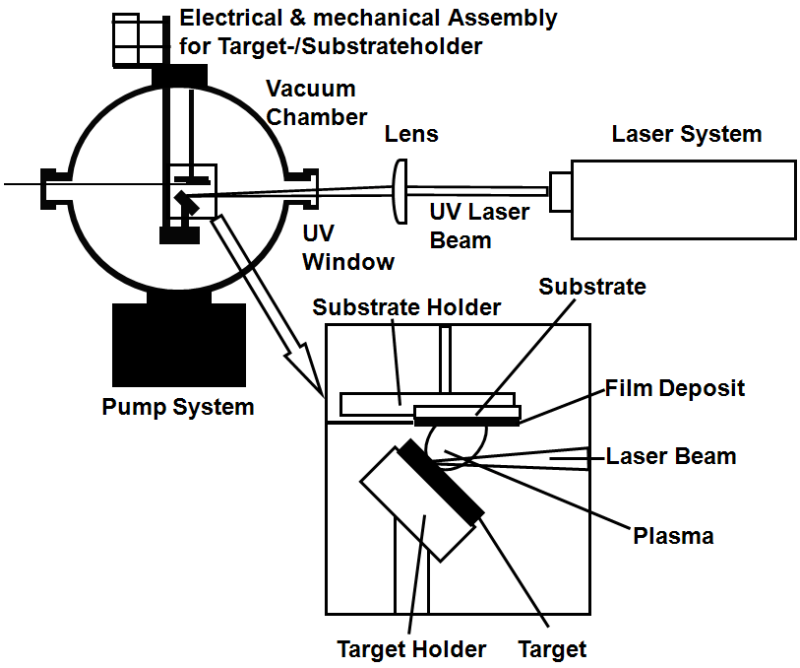

Figure 1.3: Schematic diagram of the pulsed laser deposition (PLD) process.

In this process, a UV laser (200-400 nm) with high peak power and short pulse width (fs to ns) is more effective than other lasers such as a Nd:YAG laser (1064 nm, ms pulses) or CO_2 laser (10600 nm, ms to cw pulse width). In general, the absorption coefficient of the target material can be increased with a shorter wavelength laser. This will reduce the threshold power required to ablate the material. In addition, the UV laser penetration depth in the target is shorter than that of lasers with longer wavelengths, which can produce a smoother target surface during the PLD process.

1.1.2.2 Laser drilling

Laser drilling to generate holes is one of the most important manufacturing processes used today. Holes serve a variety of functions including fasteners for assembly, weight reduction, cooling, access to other parts, and simply for aesthetics. In the aero-engine industry, the efficient operation of an aircraft engine at elevated temperature requires many cooling holes to be drilled in high-temperature superalloy components. There are conventional ways to produce holes in countless different materials. Those are punching, drilling by rotating twist drill bits and drilling by electrochemical machining (ECM) / electrical-discharge machining (EDM), which uses high current as a heat source. However, the punching or twist drilling turn out to be inefficient for superalloy material due to work-hardening characteristics of these alloys. The ECM and EDM are less dependent on the material properties of the material, but they are not free from the high cost of tools and long lead times [21].

For the last three decades, laser drilling, which uses highly intensified radiation energy as a heat source has been considered as an attractive method for drilling of various

materials. In this process, a target irradiated by a high intensity laser beam is quickly heated up to the melting or boiling temperature. Materials are then removed by vaporization and liquid expulsion due to high vapor pressure (or recoil pressure), and eventually a hole is produced. In particular, owing to the development of the pulsed solid state Nd:YAG lasers with high peak power, the laser drilling technique has increasingly becoming an efficient method to generate cooling holes in the aero-engine hot gas path components such as combustors, turbine blades, and nozzle guide vanes [22, 23]. Moreover, the abilities of the laser to drill holes in a non-contact and automated manner and with acceptable process time, cost, and hole quality are great advantages in the application of laser drilling for mass production in the aero-engine industry. Figure 1.4 shows the schematic diagram of laser drilling process.

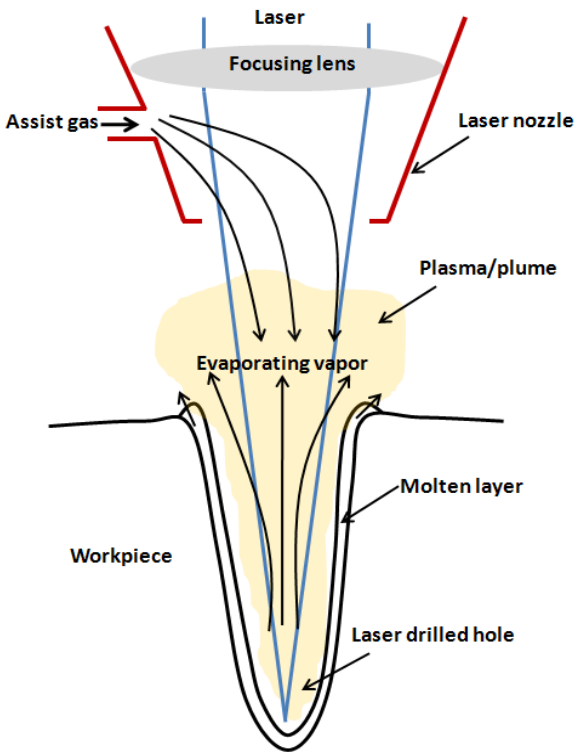

Figure 1.4: Schematic diagram of the laser drilling process.

1.1.2.3 Direct metal deposition (DMD)

Direct metal deposition (DMD) technology is an emerging laser-aided manufacturing technology compared to other laser-aided manufacturing processes such as laser cutting, drilling, and welding. It is essentially similar with laser cladding technology in that powdered metal or wire is delivered to a substrate, and it is melted and deposited on to the substrate by a laser beam. DMD is typically performed in an inert atmosphere. However, through integration of the laser cladding technology with the computer-aided design (CAD) technology, sensors, and control devices, it is possible to fabricate near net-shape products from the CAD model in the DMD process [24-26]. The potential for the DMD process is increasing.

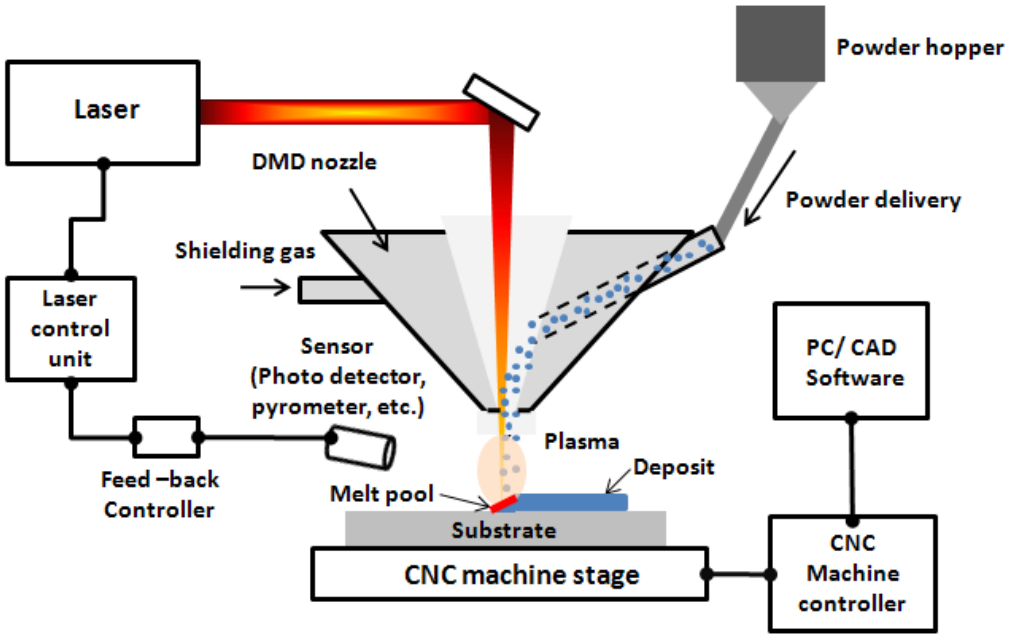

Figure 1.5: Schematic diagram of the DMD process.

Several well-known applications of the DMD process are the direct fabrication of molds and dies, repair of these parts and coating of metallic parts to improve the surface properties of the substrate. Recently, various applications have been explored for surgical instruments and military applications. Figure 1.5 shows schematic diagram of the DMD process.

1.1.3 Optical emission spectroscopy (OES) for plasma diagnostics

When a high power density laser beam irradiates a target, a plasma is formed near the target surface. Plasma produced in laser material processing is a partially ionized gas composed of atoms, ions, and electrons. In general, plasma acts as a shield against an incident laser beam, and the amount of the laser beam energy which is delivered to the target can be reduced due to the absorption of beam energy by the plasma. This is called the Inverse Bremsstrahlung (IB) effect [1, 27]. However, depending on the electron density distribution in the plasma, it can also focus the beam and enhance energy transfer.

Due to the close association between laser processes and plasmas, the plasma has acquired great interest as a source to diagnose laser processes. Optical emission spectroscopy (OES) is known as one of techniques widely used for the diagnostics of laser-induced plasmas [28]. The OES examines the wavelengths of photons emitted by atoms or ions while they transition from an excited state to a lower energy state. Each element emits a characteristic set of discrete wavelengths according to its electronic structure. By observing and analyzing these specific wavelengths (or emission lines) from an emission spectrum, the OES can give useful plasma information such as plasma temperature and particle density. Compared to absorption spectroscopy, which needs

more expensive facilities and more complicated procedures for analysis than OES, it is easily incorporated into a system using simple optics, a spectrometer, and data acquisition devices. This is why OES is a more acceptable method for real-time monitoring of plasmas in laser material processing.

1.2 Motivations and objectives of research

The motivation of this study is to explore the basic science for laser material processing in high temperatures (involving plasma generation) and high power densities (10^8 W/cm^2 to 10^5 W/cm^2). As mentioned earlier, three different processes are being studied in three power density levels:

1) Pulsed laser deposition (> 10^8 W/cm^2) of yttria-stabilized zirconia (YSZ) and Ni-base superalloy with congruent evaporation and texture control for two important turbine blade materials.

2) Pulsed laser drilling of Ni-base superalloy (> 10^6 W/cm^2) for an optimized process and diagnostics.

3) Direct metal deposition (> 10^5 W/cm^2) for online composition monitoring.

The detailed objectives for each process with different power density are discussed below.

1.2.1 Pulsed laser deposition of YSZ and Ni-base superalloy (> 10^8 W/cm^2)

Thin films (or coatings) have created considerable interest in the optical, electronic and aerospace communities, and a multitude of fabrication techniques are reported in the

literature. In general, smooth and uniform surfaces, stoichiometric balanced deposits, and superior thermo-mechanical properties are desirable in hard overcoats and protective coatings. Pulsed laser deposition (PLD) is generally known as one method that can satisfy the requirements mentioned above. In addition, it has been noted as one of the most technologically versatile and economically acceptable methods for deposition. In this study, the PLD technique is used to deposit yttria-stabilized zirconia (YSZ), which is used as a thermal barrier coating (TBC). The performance of the PLD technique to fabricate YSZ films of high quality is evaluated by investigating the properties of the YSZ films produced. Analysis for surface morphology, composition, and mechanical properties is carried out through characterization of the films produced.

Ni-base superalloys have been widely used as a base material in the aero-engine industry due to their excellent yield strength, good corrosion, and creep resistance. Most commercial Ni-base superalloys consist of a Ni matrix (γ phase) and an intermetallic Ni_3X (γ' phase, X denotes Al or other elements in alloys) phase. The γ'-phase is known to be the primary strengthening phase of the entire composite [29]. When a bulk Ni-base superalloy is produced to have a single crystal (SC) microstructure, this configuration can enhance creep strength and corrosion resistance at elevated temperatures. Because of the need for high temperature creep resistance, turbine blades operated at extreme temperatures require a SC microstructure. In most cases, this material degrades as a result of long time operation at elevated temperatures and pressures. Given the high cost required to replace engine-run parts, the repair and re-use of field-run blades is considered to be more acceptable for manufactures. Laser-assisted deposition processes could be a potential candidate for the treatment of the degraded Ni-base superalloy parts

by depositing materials on damaged area. In this research, the PLD technique is used for the deposition of thin Ni-base superalloy coating on single crystal (SC) substrates of the same material with the aim to produce the homo-epitaxially grown thin coating. The influence of the process parameters such as substrate temperature, pulse energy, pulse repetition rate, and deposition time on the crystallinity of coatings is analyzed.

1.2.2 Pulsed laser drilling of Ni-base superalloy (> 10^6 W/cm^2)

As mentioned earlier, laser drilling is becoming a leading technique in many manufacturing processes by replacing conventional drilling techniques such as ECM or EDM. In particular, generation of cooling holes in aero-engine components is the largest application of laser drilling. Reducing a drilling time for relevant aerospace applications of the laser drilling is a major task when considering that one jet engine generally needs over one million cooling holes [30]. In this research, a pulsed solid-state Nd:YAG laser (DPSSL) is used to drill holes with a shallow angle, 30^o to the surface, in Inconel 718, which is one of the commercial Ni-base superalloys used in the aero-engine industry. The main goals of this study are to systematically investigate the effect of process parameters on the hole quality such as drilling time, hole size, hole taper, and recast layer thickness and to find process conditions to improve drilling performance. This study also provides the strategy for systematic hole quality examination which could be effectively employed in the manufacturing industry.

Theoretical analysis of laser drilling is complicated by simultaneous interaction of heat and mass transfer, phase transition and fluid flow. When the high power density laser beam hits a solid target, it is either being reflected, transmitted, or absorbed. The

radiation energy absorbed by the target is converted to thermal energy, and then it is transferred through the target material. Due to the high thermal energy absorbed by the substrate material, it undergoes a melting and vaporization process when the temperature of the material exceeds that of the melting and vaporization. Recoil pressure generated by the vapor flux is the main driving force to eject liquid metal from the cavity created by the laser beam. As a result, materials are removed from the target in liquid and vapor forms [31]. In this study, a numerical simulation for pulsed laser drilling is carried out to enhance the fundamental understanding of the high power density laser process by using a model with relevant physics. The main objective of numerical simulation is to investigate the influence of different pulse formats on drilling performance as indicated by process time, hole size, and recast layer thickness.

Laser-induced plasmas have been comprehensively studied for various materials and different areas of laser material processing. However, no studies have reported how plasma parameters, including line intensity, electron temperature and number density, directly correlate with drilling performance as indicated by drilling depth. In this study, the correlation between the plasma parameters and the drilling depth is investigated as a means of improved process diagnostics during the laser drilling process.

1.2.3 Direct metal deposition for online composition monitoring (> 10^5 W/cm^2)

Direct metal deposition (DMD) is an emerging technology which shows great potential for direct manufacture of three-dimensional parts. In the DMD process, unstable factors (non-uniform powder feeding and laser power, non-uniform laser-plasma interaction, etc.) could affect composition of the deposits, which in turn, results in non-

uniform properties of the deposits. Uniform composition of the deposits is essential to maintain superior material properties of the products. Therefore, the development of a technique to monitor and control the composition of deposits in the DMD process is required.

The literature studying plasma observation in the DMD process is very limited. In addition, study for plasma of Ni-base superlloy (Inconel 718) in the DMD process has not been reported yet. In this study, spectroscopic data obtained from Inconel 718 plasmas is employed to monitor the compositional information of the deposit during the DMD process. An attempt to find a fundamental theory and a strategy to correlate spectral data with the composition created during DMD process is made by using optical emission spectroscopy (OES).

1.3 Dissertation outline

This chapter presents a general background on laser processing, laser processes covered in this study and the OES method. The motivations and objectives of this study have also been presented in this chapter. Chapter 2 reviews some of the past research related to this study. Chapter 3 describes the experimental procedures for the PLD, the laser drilling, and the plasma observation experiments during laser drilling and DMD. The theoretical background and strategy for numerical simulation is also presented in chapter 3. Chapter 4 includes the results and discussion for: (1) pulsed laser deposition of YSZ and Ni-base superalloy, (2) laser drilling of Inconel 718, (3) plasma diagnostics during laser drilling and DMD, and (4) numerical simulation of pulsed laser drilling. Finally, chapter 5 provides conclusions and future work.

CHAPTER 2

LITERATURE REVIEWS

2.1 Literature review on the deposition of yttria-stabilized zirconia (YSZ)

Thin films or coatings have been widely used in various applications either as functional coatings or as structural overcoats. The former case implies the application of thin films as optical coatings for mirrors and filters [32, 33] or as active or dielectric layers in semiconductor devices [34-36]. The latter case, for example, implies thin coatings on machine tools and mechanical parts such as gear, bearing, pump and engine components to reduce wear as hard overcoats [37, 38]. In addition, they can be considered as protective overcoats such as thermal barrier coatings (TBCs) to shield surfaces from an adverse environment [8, 39].

In applications as hard or protective overcoats, ytrria-stabilized zirconia (YSZ) has been reported as an attractive material. The superior mechanical properties of the YSZ enable the YSZ coatings to be used in various mechanical components to reduce wear of the base materials. Furthermore, excellent thermal properties such as low thermal conductivity and high coefficient of thermal expansion ensure that the YSZ coating is a

robust material for thermal shock when it is used as a topcoat of the thermal barrier coatings (TBCs) which are used to protect hot-section components of an aircraft engine.

There have been many studies on the deposition of YSZ coatings by different techniques, and various characteristics (mechanical, structural, morphological and compositional property) of these have been investigated. An electron beam directed vapor deposition technique was used to grow YSZ coatings [40]. All YSZ coatings deposited by this method exhibited a columnar structure with many elongated pores that extended from the substrate to the top of the coating.

Laser-glazed plasma spraying has also been used to produce YSZ thermal barrier coatings [9]. It was found that surface roughness and porosity were significantly reduced after laser surface treatment. Maximum reduction (from 14 μm to 2 μm) in the average surface roughness was obtained at the lowest scanning speed (5000 mm/min) and the highest laser energy density (14 J/mm^2). The thermo-mechanical properties of nanostructured YSZ coatings developed by plasma spraying were also studied [41]. According to results, the measured micro hardness, 8.6 GPa, is about 1.6 times as large as that of traditional zirconia coating due to the fine grain size (30–110 nm) of the deposits.

Poulston *et al*. [42] reported the characteristics of YSZ coatings fabricated on alumina substrates by the sol-gel synthesis technique. The average surface roughness was approximately 100 nm. Rounded particles of 1–3 μm size were uniformly distributed throughout the coating surface. Ion-beam-assisted deposition was carried out to produce YSZ thin coatings from a metallic zirconium target and from a compound zirconia target [43]. The coatings from the zirconia target appeared harder than those from the zirconium

target due to either the higher O/Zr ratio or the closer to ideal stoichiometric state of the coatings.

Iijima *et al*. [12] also used the ion-beam-assisted technique to deposit thin YSZ coatings. Smooth surfaces with the surface roughness of several nano meters were obtained, and a ripple surface morphology was found. Smooth and dense YSZ coatings were also produced using the PLD technique [44-46]. Biaxially aligned and dense YSZ coatings were produced on glass substrates at the room temperature [44]. Very smooth YSZ thin coatings with 1-2 nm surface roughness were obtained [45]. However, the thickness of the deposits was only 40–225 nm. Also, the surface roughness tended to increase with the thickness of coatings. Dense YSZ thin coatings were deposited on glass and CeO_2 –Sm_2O_3 substrates by the PLD technique using a XeCl laser [46]. The hardness of YSZ coatings was found to be in the range of 11.7-12.7 Gpa, independent of substrate temperature, target-substrate distance and the annealing process. The composition of deposits was fairly close to that of the target material. Other characteristics (thermo-physical, electrical and optical properties) of YSZ coatings were presented in [14, 47-50].

2.2 Literature review on the deposition of nickel-base superalloys

One of the most suitable superalloys in the aero-engine industry is a Ni-base superalloy. Ni-base superalloys are composed of various elements including nickel, chromium, iron, cobalt, titanium, tungsten, molybdenum, aluminium, and other rare metals. Ni-base superalloys generally consist of a Ni matrix (γ-phase) and an intermetallic Ni_3X (γ'-phase, where X is Al or other elements in alloys) phase which coherently precipitates in the Ni-base matrix as an ordered cuboidal, spherical, or

irregular form. It is well known that outstanding mechanical properties of the Ni-base superalloys at elevated temperatures are provided by intermetallic γ' phase [29, 51, 52].

When Ni-base superalloys are cast to have a single crystal (SC) microstructure, their creep strength and corrosion resistance at high temperature can be further enhanced compared to a polycrystalline microstructure by removal of the grain boundaries, which have weak bonding and high chemical activity. Due to this fact, SC Ni-base superalloys have been used as a material for turbine blades in aircraft engines [53]. However, in most cases degradation of these materials is unavoidable after extended operation due to cyclic temperature gradients and high corrosion and oxidizing atmosphere. The life of these high cost components is mainly limited by defects such as cracks and erosion generated by operating in an extreme environment, and techniques to repair damaged parts receive a great deal of attention for economic interest.

Laser-assisted deposition processes could be a candidate to repair the damaged area of the Ni-base superalloy by filling up the damaged parts with the same material. In these processes, the epitaxial growth of deposits, which take on a lattice structure and orientation identical to those of the substrate (especially it is called the homoepitaxial growth when the epitaxial growth occurs on a substrate of the same material), should be achieved to obtain the same structural characteristics as that of the base material.

So far, only a few investigations have been reported for epitaxial deposition of Ni-base superalloy. Gäumann *et al*. [54] developed a process called epitaxial laser metal forming (E-LMF) to achieve the homoepitaxial growth of the Ni-base superalloys on the SC Ni-base superalloy substrates. Important conclusions leading to the SC deposition

were as follows: (1) the small temperature gradient in the melt pool, and (2) the sufficient re-melting of the substrate for epitaxial growth.

Felberbaum *et al*. [55] also used the E-LMF technique to obtain Ni-base SC superalloy deposits on the same material (CMSX-4). The laser-clad material was grown epitaxially onto the CMSX-4 substrate. They tailored process parameters according to solidification theory, described in [54], to sequentially produce epitaxial layers onto the substrate. Thermal fatigue test showed that thermal fatigue resistance of the epitaxially deposited layers was similar to that of the virgin base material.

Bezencon *et al*. [56] deposited MCrAlY alloys (where the M stands for Ni or Co) on a SC Ni-base superalloy substrate (CMSX-4) by laser cladding to produce SC oxidation resistant coatings. Four MCrAlY alloy powders with different compositions were selected. The influence of the primary solidification phase (γ-Ni, γ'-Ni_3Al or β-NiAl) on epitaxial or non-epitaxial growth was discussed. The epitaxial growth only occurred when the primary phase to solidify was γ (Ni).

The vapor–state deposition of Ni-base alloys has been investigated by several researchers [57-61]. Singh et al. [57] used the pulsed laser deposition (PLD) technique to produce Ni-Al and Ni_3-Al films on silicon substrates at varying substrate temperatures up to 400 ^{o}C. These films were characterized by small randomly oriented grains exhibiting polycrystalline structures. The Ni/Ni_3Al multilayers were sputter-deposited on NaCl (001) substrates at ambient temperatures and at 450 ^{o}C [58]. The multilayers deposited at 450 ^{o}C grew epitaxially and exhibited a <001> preferred orientation. Almeida et al. [59] used r.f.-magnetron co-sputtering to deposit Ni_3Al thin films on SC Ni substrate. The heteroepitaxial (epitaxial growth on a substrate of different material) growth of Ni_3Al

films occurred on heated (110) SC Ni substrates. To date, all the deposition studies were performed for a binary alloy system (Ni-Al), where the depositing materials were different from the materials used for the substrates. Only two studies [60, 61] (Ref. 61 is from this study) reported the use of the PLD technique for the homoepitaxial growth of Ni-base superalloys on the SC Ni-base superalloy substrates. In these studies, the effect of process parameters including substrate temperature and pulse energy on the structural characteristics of deposits was investigated.

The mechanism to govern the grain structure of vapor deposited metallic films has also been reported [62]. This work studies a range of the substrate temperature and characterizes the grain structure of the resultant films. When the substrate temperature is less than $0.3T_m$ (melting point), very fine equiaxed grains are formed, and these grains are frequently separated by boundaries containing a high density of pores or voids. In this temperature range, the mobility of the adatoms is low, and the incoming deposit atoms stay where they land. When the substrate temperature is between $0.3T_m$ and $0.5T_m$, the mobility of deposit atoms increases so that they can take up vacant lattice sites at the grain surface. This phenomenon was referred as granular epitaxy in the study to point out the role of the first grains in controlling the final grain structure of the film. In this regime, initial grains with local epitaxy continue to grow as the film thickens, and they form a uniform columnar grain structure. In the temperature range above $0.5T_m$, more bulk grain growth occurs through the coalescence of neighboring grains due to the increased mobility of grain boundaries and bulk diffusion at high temperature. This result suggests that a monolithic film with the epitaxial growth is more likely to be formed under the high substrate temperature ($> 0.5T_m$).

Moazed [63] proposed that low supersaturation in the vapor deposition process is also an important factor for the epitaxial growth of deposits. According to his study, at low supersaturation only preferred sites can act as nucleation sites to form a particular orientation for the epitaxial growth while at high supersaturation, random nucleation is more likely. The effect of the orientation of the initial nuclei on the final orientation of the deposit is described in [64]. It is suggested that the initial occurrence of a large number of one type of nuclei with a high growth rate may dominate the final deposit orientation leading to epitaxial growth. It is also mentioned that preferred recrystallization during the coalescence could have an influence on the epitaxial growth of deposits.

As described above, studies for the homoepitxial deposition of the SC Ni-base superalloy are very limited. Furthermore, most of these studies are based on laser cladding involving re-melting of the substrate. One study [60] reported the homoepitaxial deposition of the SC Ni-base superalloy by the pulsed laser deposition (PLD) technique. However, only the substrate temperature was considered as the independent process parameter in the study. In this present study, the process for homoepitaxial deposition of SC Ni-base superalloy is developed based on PLD. Four independent process parameters (substrate temperature, pulse energy, pulse repetition rate, and deposition time) are considered to investigate the effect of various process parameters on the structural characteristics of deposits.

2.3 Literature review of laser drilling

Laser drilling is extensively used in industry for making hole in various materials. Exploring the role of various process parameters in the laser drilling process is important to enhance the quality of the laser-produced holes. To date, a number of studies for the laser drilling process have been reported. The relationship between geometrical characteristics of the hole such as hole size, circularity of hole, and hole taper versus process parameters was tested [65-68]. Ghoreishi *et al*. [65] investigated the effect of the focal position on the hole geometry. According to their study, the effect of focal position on the hole taper was most significant compared to other variables (peak power, pulse width, pulse frequency and assist gas pressure). Positive focal position (above the workpiece surface) produced holes with less taper (due to enlargement of exit hole size) because a beam diameter at the hole exit was larger than that for a zero (on the workpiece surface) or negative (below the workpiece surface) focal position.

Bandyopadhyay *et al*. [66] also investigated the effect of process parameters, mainly pulse energy, on the hole taper. Higher pulse energy was found to lead to lower taper, which is similar to the results shown in [65]. High pulse energy generally produced larger entrance diameters. It also produced larger exit hole diameter, primarily because by enhancing material vaporization it reduced the possibility of re-solidification of molten materials in the hole. The increase in assist gas pressure also led to a decrease in the hole taper. Once the laser beam broke through the exit side, high gas pressure helped molten material to be ejected from the exit side as well as the entry side. This promoted the increase of exit hole diameter, consequently resulting in hole straighter holes [68].

The metallurgical characteristics, such as recast micro-cracks, and spatter deposition of laser-drilled holes was also investigated [69-73]. The effect of process parameters on the recast and micro-cracking was investigated in [69]. The recast layer was generally thicker at the entrance side than at any other point along the depth of a hole. The assist gas pressure, peak power and focal position were the parameters that exerted the most significant influence on the recast layer thickness. The increase of peak power, the decrease of the trepanning speed and the focal position on the working surface led to a reduction in the recast thickness. A higher assist gas pressure generally tended to minimize the recast layer. However, an excessive gas pressure promoted rapid cooling of molten material, and therefore inhibited the removal of the molten material. The largest micro-cracks was located at the hole entrance, which was most exposed to rapid cooling.

Li *et al*. [70] presented a novel high peak power pulse burst laser for drilling. They used a Q-switch pulse laser operated at a 400 KW peak power and a 5-50KHz repetition rate burst for a percussion drilling experiment of Cu and Ni-alloys. A hole diameter of 200 μm was obtained. A recast layer was about 10 μm, and there was no micro-cracking observed with SEM. Corcoran *et al*. [71] studied about laser drilling of multi-layer aerospace material systems. The multi-layer system used in the experiment was a René 80 substrate coated with a thermal barrier coating (TBC). High pulse energy reduced the level of micro-cracking in the holes. Low pulse energy, however, reduced the level of adherent re-melt material remaining on the edge of holes. Also, shorter pulse widths reduced the severity of micro-cracking and delamination between the TBC and bond coat significantly. The effect of process parameters on spatter deposition was shown in [72, 73]. Short pulse width, lower peak power, and higher pulse frequency generally

resulted in a reduction of spatter deposition [72]. The spatter bonding strength was found to decrease with the use of oxygen and oxygen-containing assist gases [73].

Many researchers have employed a design-of-experiment (DOE) during laser drilling experiments to systematically investigate the effect of process parameters on laser drilling performance. Cocoran *et al*. [71] used the Taguchi method containing an L18 ($2^2 \times 3^3$) orthogonal array design. The effects of percussion laser drilling on the material interface, bond strength, re-melt layer, and micro-cracking were investigated, and optimal process parameters were determined. Tam *et al*. [74] also reported the use of the Taguchi method for optimization of the laser deep hole drilling of Inconel 718 to minimize drilling time. Ghoreishi *et al*. [65] used the central composite design (CCD) in their study to investigate the effect of parameters on hole taper, circularity, and interactions among the six controllable variables. The effect of material properties was also assessed.

The above research has provided the considerable knowledge about the laser drilling process; however, most of these studies have been devoted to holes drilled at 90^o to the specimen surface and all holes were produced by either percussion drilling or laser trepanning. In this study, cooling holes angled at 30^o to the workpiece surface were produced to mimic real holes in a turbine blade by three different drilling modes including helical, percussion, and trepan drilling. The effects of the process parameters and drilling modes on the hole quality and drilling performance have been comprehensively investigated. This study also provides a systematic strategy for hole quality examination which can be usefully employed in industry.

2.4 Literature review on plasma diagnostics during laser material processing

Laser-induced plasmas have been widely investigated in the various areas of laser material processing. In particular, the optical emission spectroscopy of laser-induced plasmas has become a powerful tool for the process monitoring and material analysis, as well as means to study the fundamentals of laser-material interaction. Li *et al*. measured the spatially and temporally resolved temperature of the during laser percussion drilling using optical emission spectroscopy [75]. In their experiments, SAE 52100 steel was drilled with a diode-pumped Nd:YAG laser. Helium and oxygen gas were used as the shield gases. The results indicated that the plasma electron temperature increased as the average power increased and decreased as delay time for data acquisition increased. A nearly constant plasma cooling rate of ~4×10^9 K/s was obtained for most of process conditions. The plasma temperature was higher with oxygen than with helium. Drilling time decreased as laser power increased, although this decrease in drilling time was not proportional to the increase in power. M. Li *et al*. considered that more absorption of laser energy by the plasma at higher plasma temperatures was responsible for non-proportional decrease. Spatial and temporal characteristics of laser-induced plasmas for different materials such as aluminum [76] and $LiNbO_3$ [77] have also been reported by other researchers.

Kumar *et al*. [78] studied the effect of background gas on excimer-laser-produced copper plasmas. It was shown that the intensity of spectral lines increases in presence of a background gas (argon and neon gas). This was because the background gas collided with the plasma, thereby confining it to a small region.

Electron number density and temperature during the early phase (< 300 ns) of a laser–induced plasma produced by a pulsed Nd:YAG (266 nm) were investigated [79]. It was observed that in the early stage of plasma evolution, 30-300 ns, the electron temperature was very high; it dropped rapidly from ~70,000 K to ~15,000 K while the electron number density fell from 4×10^{19} cm^{-3} to 5×10^{18} cm^{-3} for irradiance in the range of 2-80 GW/cm^2. After 300 ns, both temperature and electron number density decreased much slowly.

A pulsed Nd:YAG laser (532 nm) was used for ablation of silicon in air [80]. Electron temperatures in the range of 6,000 to 9,000 K and ion temperature in the range of 12,000 to 17,000 K with an electron number density of $\sim10^{18}$ cm^{-3} were observed for pulse energy in the range of 0.12 to 46 mJ. The size and shape of a silicon plasma was also characterized as a function of laser energy and delay time.

Shaikh *et al*. [81] reported the spectroscopic study of a zinc plasma produced in air by a Q-switched pulsed Nd:YAG laser operating at 1064, 532, and 355 nm. It was shown that electron temperature and number density were maximum near a target surface, and they decreased as the distance from the target increased. In addition, it was shown that the electron temperature of plasma increased with laser wavelength because the plasma absorbed more beam energy at longer wavelengths.

Lacroix *et al*. [82] investigated characteristics of a laser-induced plasma during the laser-welding process of stainless steel and other materials (iron and chromium). A pulsed Nd:YAG laser with average powers from 300 to 900 W and pulse durations between 1.5 and 5 ms was used. Eight neutral iron atom lines (523.94-544.69 nm) were used to calculate electron temperature. The electron temperature varied in the range of

4,500-7,100 K. The absorption of a laser beam in the plasma was calculated using Inverse Bremsstrahlung (IB) theory. For the electron temperature of 4,000-7,100 K, the IB absorption coefficient varied between 0 and 0.4 m^{-1}.

Tewari [83] observed the plasma produced during laser cladding to correlate spectral data with elemental compositions in clad. Integrated average emission line intensities and their ratios for Nb and Hf atoms and Al ions were used to estimate a relative composition of elements in plasma. The quantitative correlations between line intensity ratios ($I_{Nb\text{-}I}/I_{Al\text{-}II}$ and $I_{Nb\text{-}I}/I_{Hf\text{-}I}$) and the Nb concentration in the clads were obtained for different laser powers. The relationship between among plasma temperature, line intensity, intensity ratio, composition, and clad thickness were also investigated.

Onge *et al*. [84] reported the use of laser-induced plasma spectroscopy for the quantitative analysis of Al, Cu, Fe, Pb and Sn in solid zinc alloys. A Q-switched Nd:YAG laser operating at 1064 nm was used to ablate solid zinc alloys of several different compositions. They obtained calibration curves estimating compositions of different alloying elements by studying the ratio of various emission line intensities. Zhang *et al*. [85] also presented a similar method to analyze atomic concentration ratios of La and Sr in CoO_3 ferroelectric films. In their study, ratios of emission line intensity were related with atomic concentration ratios to find the coefficients for quantitative correlations. The results obtained from plasma spectroscopy were almost in agreement with the corresponding values obtained by traditional compositional analysis techniques.

As described above, the plasma in laser material processing has been widely studied to date; however, a study for the direct relationship between plasma parameters and drilling depth has not been reported yet. In addition, no research has reported the plasma

observation of aerospace material (Inconel 718) in the DMD process. In this study, the plasma of Inconel 718 is investigated for the purpose of monitoring laser drilling and DMD. In laser drilling, spectral data is correlated to the drilling depth to predict the drilling depth during the process. In the DMD process, plasma information is correlated to the elemental composition for the online monitoring of the composition created during the process by employing optical emission spectroscopy (OES) method.

2.5 Literature review on theoretical study of laser drilling

The modeling of laser drilling necessitates an interdisciplinary approach involving heat transfer, fluid flow, and phase change, as well as the tracking of the liquid-vapour interface. For a reasonable prediction of the process, modeling all the relevant physics is necessary. Allmen *et al*. [86] developed a simplified one-dimensional laser-material interaction model. The model calculated material removal rate as a function of the absorbed intensity; however, the effect of the phase transformation was not considered in the model. Chan *et al*. [31] developed a one-dimensional steady-state model which can describe material removal by vaporization and liquid expulsion. Simple one-dimensional fluid flow and the Knudsen layer were considered in the model.

Kar *et al*. [87] reported a two-dimensional model for laser drilling. The phase transformation was included in the model by employing the Stefan condition at solid-liquid and liquid-vapor interface; however, the shape of the laser induced crater was intentionally assumed to have a parabolic form to simplify the model. The influence of the liquid flow and conduction heat loss were not considered in the model. The effect of

the multiple reflections of laser beam inside the cavity was taken into account in the later version of the model [88].

An analytical laser-material interaction model was also reported [89]. The attenuation of a laser beam within the vapor was taken into account in the model. A singular perturbation technique was used in order to find solutions for pre-vaporization and post-vaporization; however, the evaporation physics were overly simplified, and melting was not considered in the model. Cheng *et al*. [90] developed a three-dimensional heat flow model using the finite difference method (FDM). In the model, phase change involving melting and vaporization was considered by using the enthalpy of transformation. Similar two-dimensional heat flow models using the finite element method (FEM) and the finite volume method (FVM) were reported in [91, 92].

Vaporization, melting and heat conduction during laser drilling were investigated by Zhang *et al*. [93]. The locations of phase transition were obtained by solving the energy conservation equation at the phase transition interfaces. The relationship between the temperature and pressure of the evaporating surface was obtained by using the Clausius-Clapeyron equation, but liquid flow was not considered in the model. A two-dimensional axisymmetric laser drilling model considering heat transfer and fluid flow was developed by Ganesh *et al*. [94]. In this model, the surface of laser melted pool was treated as a deformable free surface by employing the volume of fluid (VOF) approach, and pressure and temperature on the evaporating surface was provided using a gas dynamics model. However, the effect of the multiple reflections of the laser beam inside cavity was not considered in the model.

A novel laser drilling model was reported in [95, 96]. A mathematical technique, called the level-set method, was implemented to capture a liquid-vapor interface self-consistently. Unsteady heat transfer and fluid flow phenomena were modeled, considering the thermo-capillary effect and the recoil pressure. A kinetic Knudsen layer was considered to simulate evaporation phenomena at the liquid-vapour interface. Also, the homogeneous boiling phenomenon near the critical point was modeled, and the multiple reflections of laser beam in the cavity were considered in the model. In this study, the above model is developed further for studying the process of pulsed laser drilling (see section 3.5). The original model [95, 96] was developed to simulate CW laser drilling process. Therefore, it cannot be directly used to simulate the pulsed laser drilling. In the current study, numerical algorithms and relevant physics associated with the pulsed drilling process were incorporated in the model to simulate the pulsed laser drilling process.

CHAPTER 3

PROCEDURES

3.1 Pulsed laser deposition (PLD) of yttria-stabilized zirconia (YSZ)

The schematic diagram of the PLD apparatus is shown in figure 3.1. The PLD experiment was carried out in a stainless vacuum chamber using oxygen as a fill gas, and YSZ was deposited at room temperature. A hot pressed ZrO_2 target (stabilized with 5 wt% Y_2O_3, Pure Tech, Inc.) and glass (Fisherbrand cover glass, Fisher Scientific International, Inc.) substrates were used in this study. The glass substrates were ultrasonically cleaned in an acetone bath before depositions. A KrF excimer laser (Lambda Physik, 201 MSC) with a wavelength of 248 nm was operated to ablate the YSZ target at a repetition rate of 10Hz and a pulse duration of ~20 ns. The UV laser beam entered the chamber through a fused-silica UV window via an optics system composed of two UV mirrors and one spherical lens (focal length equals 50 cm). The laser was focused to a 3 mm^2 area on the target surface at a ~40^o angle of incidence. The fluence of the laser beam was 2 J/cm^2. The distance between an ablation point and the center of the substrate was ~2 cm.

The stainless steel spherical chamber of 18" diameter has two 10" flanges on its top and bottom and eight small flanges (one 4", four 2.75" and three 1.75" flanges) on its

sides. The top flange of the chamber provides the drive shaft for target holder and feedthroughs for thermocouple and electrical connections. The bottom flange of the chamber is connected to a vacuum pump system via a gate valve which separates the chamber and the pump system.

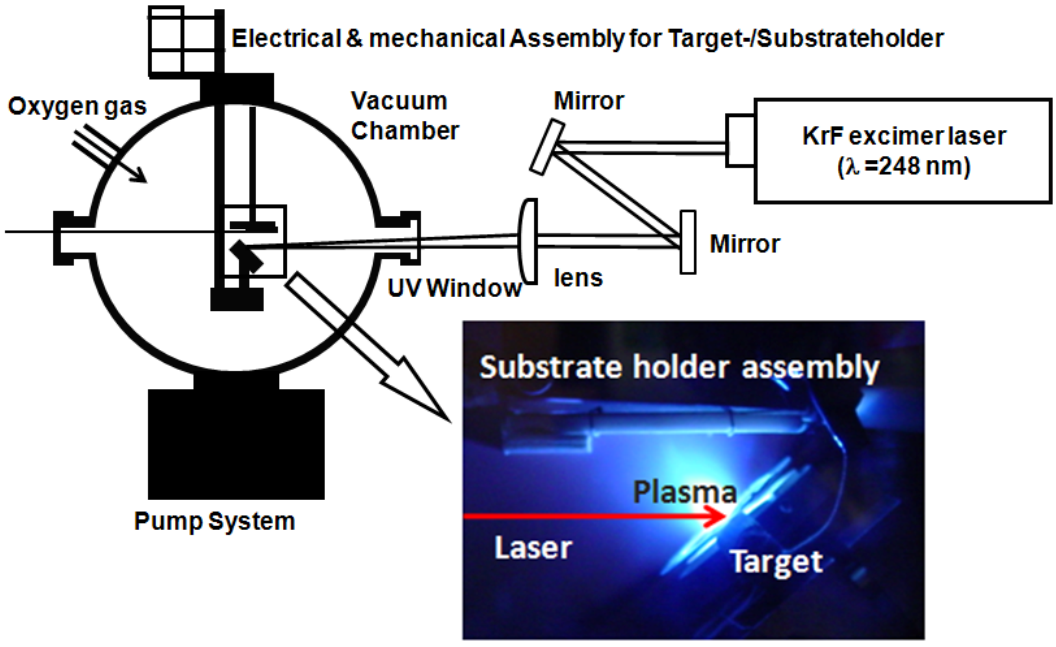

Figure 3.1: Schematic diagram of the PLD setup in this study.

Before the PLD process, the chamber is evacuated to an appropriate vacuum level required for deposition process. The vacuum chamber is first pumped down by a mechanical pump (Welch vacuum Thomas, Model 8920) to ~0.133 Pa. After that, a turbo molecular pump (Sargent-Welch Scientific Company, Model 3122) is operated along with the mechanical pump to reach a lower vacuum state. The pressure inside the chamber is measured with three different pressure gauges which are located at the end of

side flanges. A capacitance pressure gauge (MKS BARATRON, type 122 B) is used to measure the pressure above 1 Pa. A thermocouple pressure gauge (Varian, type 0531) measures the pressure 0.1 Pa to 1 Pa. An ion pressure gauge (Kurt J. Lesker, G100F) is used to measure the pressure for high vacuum (< 0.1 Pa). Figure 3.2 shows major equipments used in the PLD process.

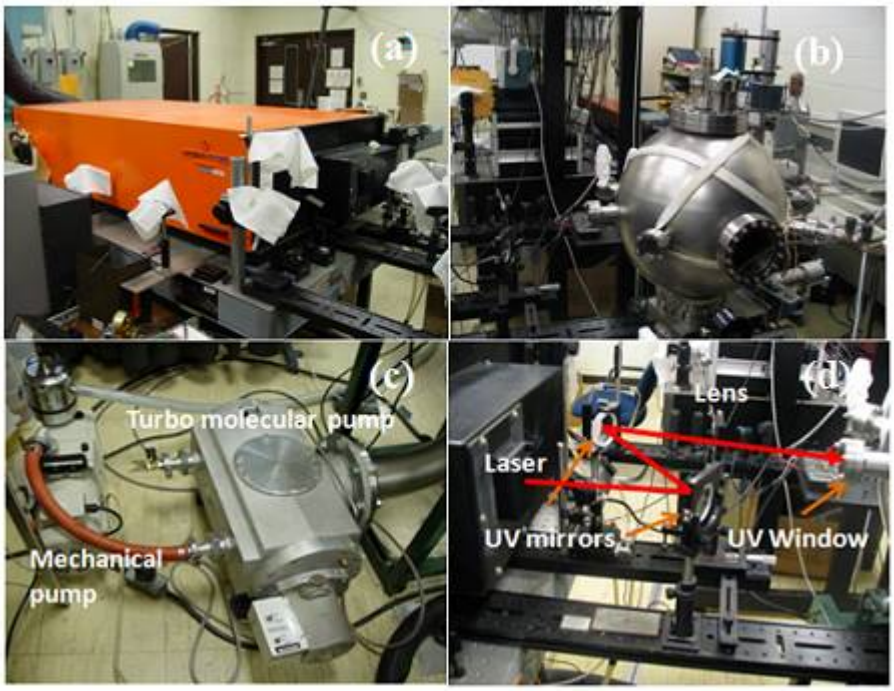

Figure 3.2: Major equipments used in the PLD process: (a) KrF-Excimer laser, (b) Stainless steel vacuum chamber, (c) Assembly of the turbo molecular and mechanical pump and (d) Optical system.

Surface morphology information was determined by scanning electron microscopy (SEM, Phillips XL 30FEG) and atomic force microscopy (AFM, Digital instruments Nanoscope IIIa). A nano-indentation test (NANO INDENTER® II) was carried out to measure the hardness and Young's modulus of YSZ thin coatings based on a load-depth

curve. A diamond Berkovich tip (3-sided pyramidal tip) was used as an indenter. The maximum load applied for the indentation test was 60000 μN. The crystal structure of deposits was identified by X-ray diffraction (XRD, Miniflex) using a Cu-K radiation source. Finally, an electron probe micro-analyzer (EPMA, CAMECA SX100) was used to investigate the elemental composition.

3.2 Pulsed laser deposition of Ni-base superalloy films

The same PLD setup described in section 3.1 was used for deposition of Ni-base superalloy films; however, the substrate temperature was varied to study the effect of temperature on crystallinity of the deposit. The PLD experiment was carried out under a background pressure of ~ 0.007 Pa. Both target and substrate were prepared from a cylindrical single crystal (SC) Ni-superalloy ingot produced by a production-scale Bridgman furnace [97]. The elemental composition of the SC Ni-superalloy ingot is shown in Table 3.1. The SC ingot with a diameter of 15 mm was cut perpendicular to the cylinder axis, which was aligned along <100> direction, to prepare thin ~ 1 mm substrates using a diamond saw. The cut surfaces of the substrates were polished with 2000 grit SiC papers and polished with a diamond powder suspension down to grain size 1 μm. The polished substrates were ultrasonically cleaned in an acetone bath prior to the deposition experiments.

Table 3.1: Elemental composition of SC Ni-base superalloy ingot.

	Ni	Al	Cr	Co	Ta	W	Mo	Re
wt %	62.7	5.6	7.0	7.5	8.4	4.5	1.5	2.8

A commercial pyrolitic boron nitride (PBN) / pyrolitic graphite (PG) heater (HTR1001, Momentive Performance Materials, Inc.) was used to heat the substrate. The heater was connected to the AC-power supply (3PN2210B, Staco Energy Products Co.) via an electrical feedthrough on the top flange of chamber. Heat control was achieved by manual regulation of the AC-power supply to reach a uniform deposition temperature. The temperature was monitored by a K-type thermocouple located at the circumference of the substrate. The ends of the thermocouple were also connected to a temperature monitor via an electrical feedthrough on the top flange of chamber. Ceramic (Al_2O_3) bolts and nuts were used to assemble the support plate, heater, substrate, and cover plate as shown in figure 3.3.

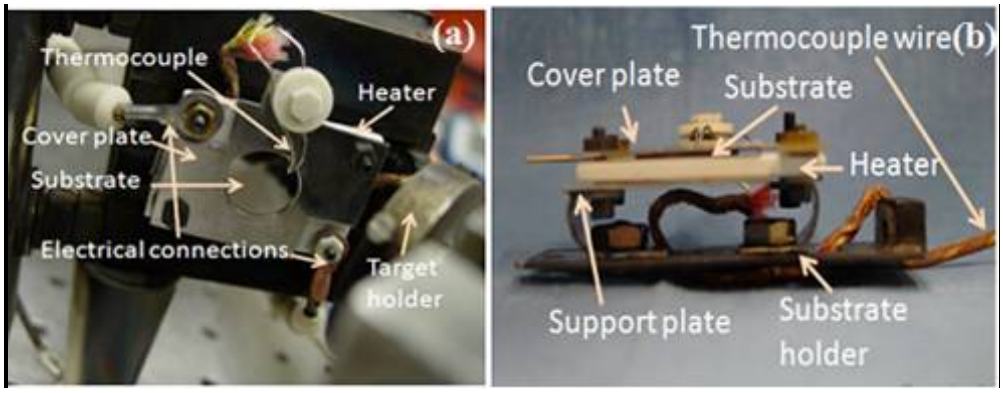

Figure 3.3: Figure of (a) PLD processing area and (b) substrate holder with integrated heater.

The chemical etching for the microstructure investigation was carried out with a chemical reagent composed of hydrofluoric acid (HF), acetic acid (CH_3COOH), hydrochloric acid (HCl) and nitric acid (HNO_3). The composition of each chemical is 1%,

33%, 33% and 33% by volume, respectively. A Taguchi experiment was designed based on an L9 orthogonal array to assess the effect of different processing parameters on the process. Process parameters for each experiment are shown in Tables 3.2 and 3.3.

Table 3.2: Deposition parameters and their levels.

Factors	Levels		
	1	2	3
Temperature (^{o}C)	850	900	950
Pulse energy fluence (J/cm^2)	2	3	4
Deposition time (min)	90	120	150
Pulse repetition rate (Hz)	10	20	30

The crystal structure of the deposits was determined by X-ray diffraction (XRD, Rigaku Rotating Anode) using a Cu-K radiation source. Microstructure and surface morphology were investigated by a scanning electron microscopy (SEM, Phillips XL 30FEG) and atomic force microscopy (Digital instruments Nanoscope IIIa), respectively.

Table 3.3: Experimental layout based on an L9 (4 factors and 3 levels) Taguchi matrix.

	Temperature (°C)	Pulse energy fluence (J/cm^2)	Deposition time (min)	Pulse repetition rate (Hz)
L1	850	2	90	10
L2	850	3	120	20
L3	850	4	150	30
L4	900	2	120	30
L5	900	3	150	10
L6	900	4	90	20
L7	950	2	150	20
L8	950	3	90	30
L9	950	4	120	10

3.3 Drilling of Inconel 718 by a diode-pumped solid state Nd:YAG laser

3.3.1 Laser drilling facilities and details of process

The laser used for drilling experiment was a high-average power diode-pumped solid-state Nd:YAG laser (DPSSL, model DP-11), manufactured by Northrop Grumman (formerly known as TRW), Space & Electronics, Redondo Beach, CA. In this study, the laser was operated at 1064 nm and two different duty cycles: 7.5 % (500 Hz pulse repetition rate and 150 μs pulse duration) and 10 % (500 Hz pulse repetition rate and 200 μs pulse duration). The duty cycle (the pulse duration divided by the pulse period) is the fraction of time that a system is in an "active" state. In this study, two different duty cycles were prepared by adjusting the duration of the pulse. In order to enhance drilling performance, the laser is modulated so that one pulse can have 17 (for 7.5 % duty cycle) and 20 (for 10 % duty cycle) small spikes with a high peak power. The full width half maximum of each spike was ~200 ns. The laser beam was focused through a lens with a 100 mm focal length. The laser was incorporated into an ANORD AD 4-axis CNC machine for precise control of the relative position between the laser beam and workpiece. An assist gas jet was introduced co-axially to the laser beam through a conical nozzle with the orifice of ~3.8 mm diameter. Ar and O_2 were employed as the assist gases in this study. Gas pressure shown in this study was the one measured at outlet port of the gas cylinder not in front of the laser nozzle.

In this study, holes at angled 30^o to the workpiece surface were laser-drilled. In order to drill a hole at angled 30^o to the surface, Inconel 718 plates 3 mm thick, 5 mm wide, and 25 mm long were positioned on the wedge slanted by 60^o with respect to the horizontal; therefore, the actual depth to be laser-drilled was 6 mm due to the relative

angle (30^o) between the laser beam and the workpiece surface. A schematic diagram of the experimental set-up is shown in figure 3.4. The DP-11 setup used in this study is shown in figure 3.5.

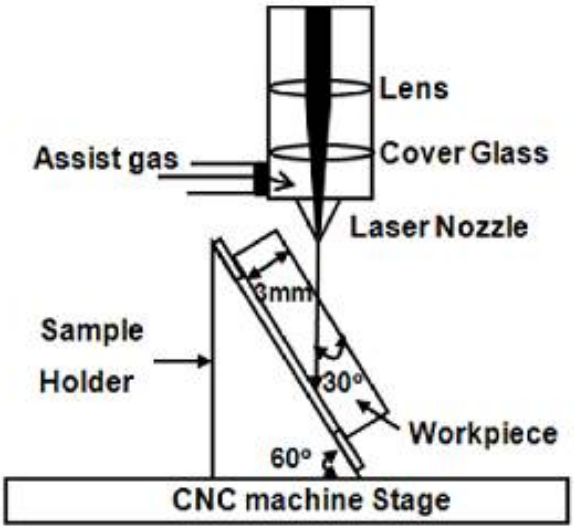

Figure 3.4: Schematic diagram of laser drilling experiment.

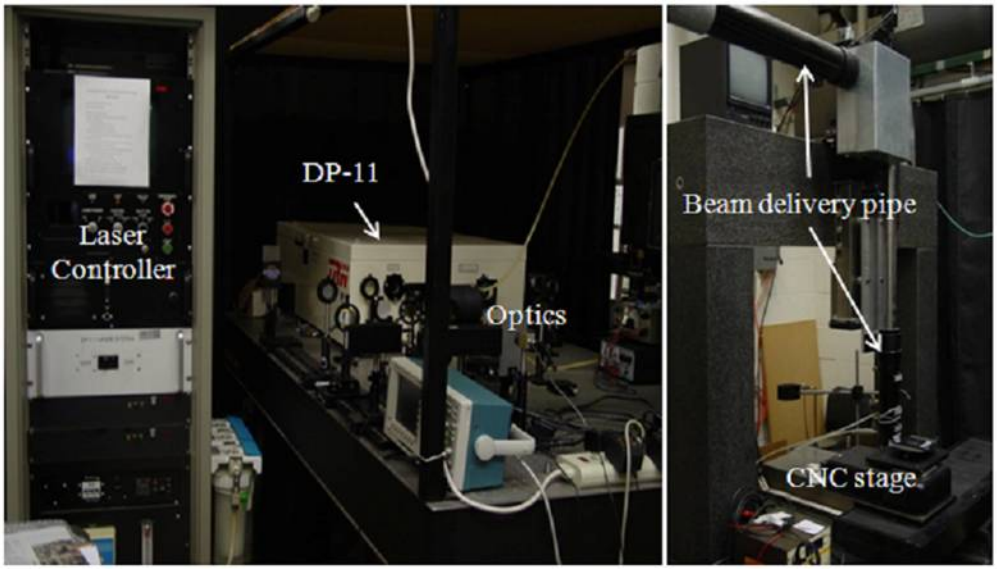

Figure 3.5: DP-11 laser used in drilling experiment.

In the first stage of the study, a set of experiments designed using a Taguchi L16 orthogonal array was conducted to investigate the relationship between the process parameters and the hole quality. In these experiments, a helical drilling technique and a 7.5 % duty cycle laser setting were used. The helicall drilling used is similar to the laser trepanning, but the key difference is that the laser beam path for helical drilling technique is composed of circles with 6 different sizes as illustrated in figure 3.6 (c). The laser beam first moves along the circle 6, the largest one (radius 230 μm), and then it follows the circle 5 (radius 200 μm), circle 4 (radius 170 μm), circle 3 (radius 140 μm), circle 2 (radius 110 μm), and finally circle 1 (radius 80 μm). Once the laser beam completes one sequence of the beam path (from circle 6 to circle 1), the beam path is repeated until it meets the experimental condition given. The number of drilling passes for helical drilling is the number of passes multiplied by the number of sequences. For example, the number of passes: 30 = 6 (passes per sequence) × 5 sequences. In these experiments, we tested 5 parameters and 4 levels as summarized in Table 3.4. Table 3.5 shows the experimental layout.

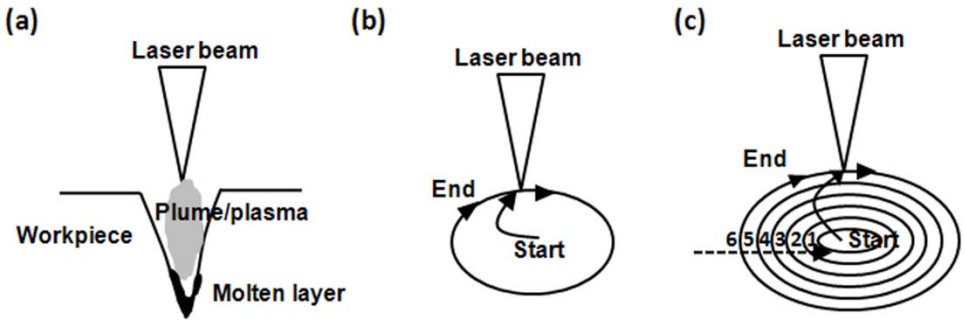

Figure 3.6: Schematic representation of (a) percussion drilling, (b) trepan drilling and (c) helical drilling.

Table 3.4: Helical drilling parameters and their levels.

Factors	Levels			
	1	2	3	4
Laser power (W)	55	60	65	70
Focal position (mm)[a]	0	-1	-2	-3
Speed (mm/s)	2	4	6	8
Ar assist gas pressure (KPa)	0	60	80	100
No. of passes	36	42	48	54

[a] - = Beam focus below the workpiece surface
0 = beam focus at the workpiece surface

In the second stage of the study, the performance of the helical drilling process was compared to percussion drilling and laser trepanning. A schematic description of the three drilling methods used in this study is shown in figure 3.6. The performance of different drilling methods was evaluated in terms of the exit hole size and the drilling time. This study also included trials to enhance the drilling performance by using O_2 assist gas, adjusting the focal position, and adjusting the duty cycle of the laser.

Table 3.5: Experimental layout based on an L16 (5 factors and 4 levels) Taguchi matrix.

Exp. No.	Laser power (W)	Focal position (mm)	Speed (mm/s)	Ar assist gas pressure (KPa)	No. of passes
1	55	0	2	0	36
2	55	-1	4	60	42
3	55	-2	6	80	48
4	55	-3	8	100	54
5	60	0	4	80	54
6	60	-1	2	100	48
7	60	-2	8	0	42
8	60	-3	6	60	36
9	65	0	6	100	42
10	65	-1	8	80	36
11	65	-2	2	60	54
12	65	-3	4	0	48
13	70	0	8	60	48
14	70	-1	6	0	54
15	70	-2	4	100	36
16	70	-3	2	80	42

3.3.2 Hole quality examination

After the laser drilling experiments were completed, the geometrical and metallurgical characteristics of laser-drilled holes were examined to investigate the effects of process parameters on the hole quality and evaluate the drilling performance. The four hole quality factors that were included were the drilling time, the exit hole diameter, the hole taper, and the recast layer thickness.

For each set of parameters, the drilling time was the time taken to complete the drilling process, and in this study, it was measured using a stopwatch. Hole size was measured using an optical microscope (Nikon OPTIPHOT) and software (Adobe Photoshop CS2) for image processing. The schematic representation of the entry and exit holes is shown in figure 3.7.

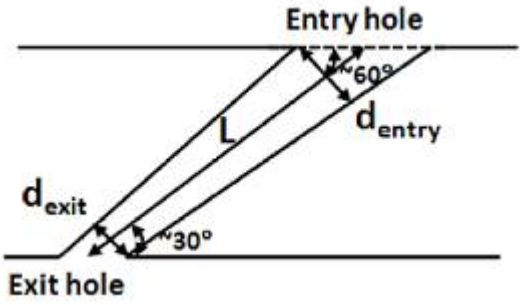

Figure 3.7: Schematic representation of the hole cross section (d_{entry}, entry hole diameter; d_{exit}, exit hole diameter; L, hole length).

The procedure measuring the entry and exit hole diameter was as follows. The image files of the entry and exit hole are first created by software incorporated into the optical microscope. The areas of the hole at the entry and exit surfaces are calculated using the image files and software for image processing. Once the hole areas at the top and bottom

surface were obtained, they were projected onto a plane which is perpendicular to drilling direction.

It is assumed that these projected areas at the entry and exit side are those of the perfect circles. Then, the projected hole areas are used to calculate the diameters of the entry and exit hole using the following equation, projected hole area = (πd^2)/4, where d is the average diameter of the hole.

Based on the entry and exit hole diameter, hole taper is calculated as follows:

$$Taper(\theta) = tan^{-1}\left[\left(d_{entry} - d_{exit}\right)/(2L)\right], \qquad (3\text{-}1)$$

where θ is the taper angle, d_{entry} is the entry hole diameter, d_{exit} is the exit hole diameter and L is the length of the hole. After the geometrical measurements were completed, the laser drilled holes were sectioned using a precision diamond saw and ground to the centre of the hole. During the grinding process, the cross section of the hole was carefully checked to confirm that the cross section was at the middle of the entry and exit hole.

Polished samples were chemically treated with a chemical reagent composed of hydrochloric acid (HCl), nitric acid (HNO_3) and glycerol for several minutes in order to measure recast thickness. The composition of each chemical was 50%, 16.7% and 33.3% by volume, respectively. The procedure to measure the recast thickness is similar to the one for the entry and exit hole diameter. An image file of hole cross section is created by the software incorporated into the optical microscope. Then an area of recast region is calculated by the image processing technique as before. It is assumed that the cross section of the recast has a rectangular shape. Then, the calculated area is the

multiplication of the short side and long side of the rectangular, and the length of the short side of the rectangular (long side of the rectangular is a hole length) is considered as the average thickness of the recast. Since the recast layer was not generally uniform for the whole cross section, the direct measurement of the recast layer thickness at the random locations could give incorrect information; therefore, the whole area of the recast region was considered to quantify the recast layer thickness in this study. The elemental composition of the at recast was analysed using an energy dispersive spectrometer (EDS) attached on the scanning electron microscope (SEM, Phillips XL 30FEG).

3.4 Plasma diagnostics in laser drilling and DMD process

3.4.1 Plasma diagnostics in laser drilling process

The laser used for spectroscopic study was the DP-11 laser described earlier. Argon gas was used as an assist gas. Holes were produced by the laser trepanning. The laser drilling experimental conditions used were shown in Table 3.6.

Table 3.6: Experimental conditions for laser drilling.

Laser power (W)	Speed (mm/s)	Focal position (mm)	Assist gas pressure (KPa)	Radius of beam path (μm)
30, 40, 50	2, 4, 8	0	50	100

Emission spectra of Inconel 718 were recorded from the plasma plume generated during the drilling process using a high resolution USB fiber optic spectrometer (Ocean Optics, HR 2000+) fitted with a 1200 groove/mm grating and entrance slit size of 10 μm. The spectrometer uses a linear charged coupled device (CCD) array (Sony ILX 511) with

2048 pixels (pixel size: 14 μm × 200 μm) to detect spectra. The spectrometer was connected to the PC with a software to operate the spectrometer for data acquisition. Plasma light was imaged on the entrance of an optical fiber (50 μm diameter) through a 10 mm focal length fused silica collimating lens. The output of the optical fiber was focused on the entrance slit of the spectrometer. In the experiment, spectra were taken over a wavelength range of 470-670 nm. Integration time of the spectral data was 20 ms. Figure. 3.8 shows the schematic diagram of experimental setup.

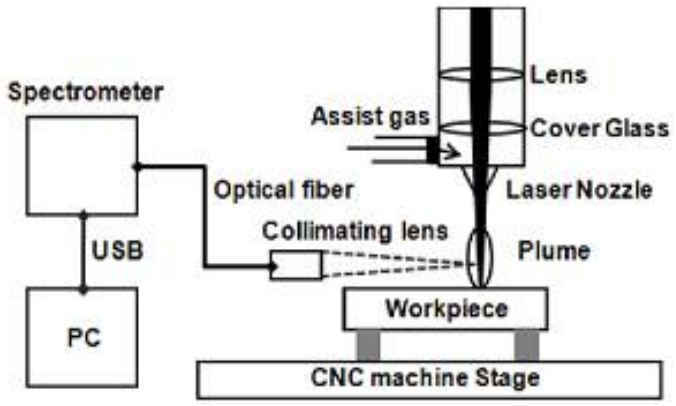

Figure 3.8: Schematic diagram of experimental setup for plasma diagnostics during laser drilling.

After the laser drilling experiments were completed, the laser drilled holes were sectioned using a precision diamond saw and ground to the centre of the hole to measure the hole depth. The hole depth was measured using the software incorporated into the optical microscope (Nikon OPTIPHOT). For each case, five holes with different hole depths were produced by varying the number of drilling passes from 1 to 5 while the other process parameters were constant.

Emission spectra were also collected during the each drilling process as shown in figure 3.9. From the emission spectra recorded, temporal histories of plasma parameters such as the line intensity, electron temperature, and electron number density were obtained (see section 4.4.1). These spectra were collected at different times, and they correspond to different drilling depths reached during the process.

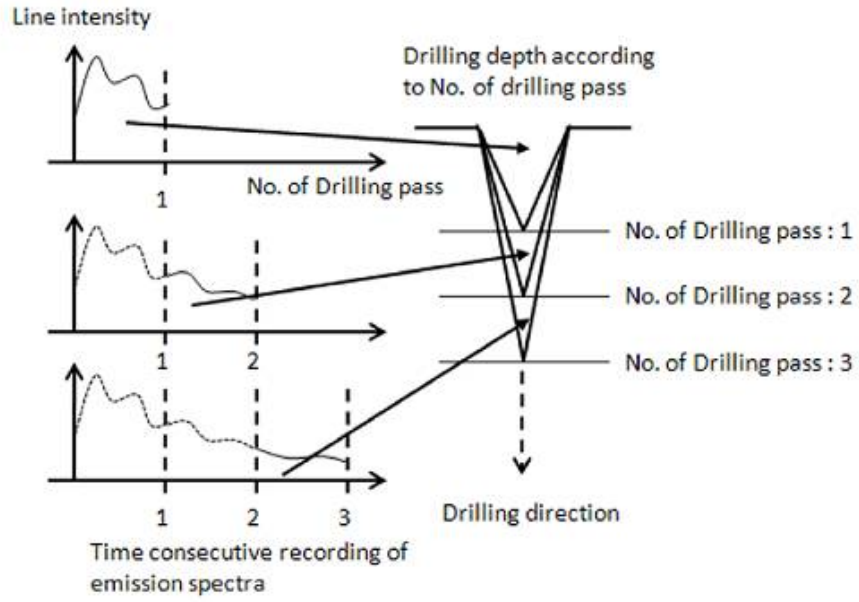

Figure 3.9: The emission spectra collected at different times correspond to different drilling depths.

3.4.2 Plasma diagnostics during the DMD process

In the DMD process, producing a uniform composition of the deposits is essential to maintain superior material properties of the deposits; therefore, the development of a technique to monitor and control the composition of deposits in the DMD process is

required. In this study, spectroscopic data obtained during the DMD process is employed to monitor the compositional information during deposition.

The laser used in DMD experiment was a 6 kW CO_2 laser (TRUMP Inc.). The laser beam was focused via a copper turning mirror and gold coated focusing mirror. The laser was incorporated into an Allen-Bradley 3-axis CNC machine for precise control of the relative position between the laser beam and substrate. Gas-atomized Inconel 718 powder (PRAXAIR Surface Technologies, Inc., NI-202, -125 μm/+45 μm) and Inconel 718 plate (52 mm × 52 mm × 7 mm) with the same composition as that of the powder were used as filler material and the substrate, respectively. The elemental compositions of Inconel 718 powder is shown in Table 3.7. Ar and He were used as a shielding and powder carrier gases, respectively. A shielding gas jet was introduced co-axially to the laser beam through a conical DMD nozzle with the orifice of ~5 mm diameter. Powder was fed from the hopper located above the laser head. The powder feed rate (PFR) was controlled by the speed of a motor to rotate the rod plugging up the bottom part of the hopper. Powder was delivered onto the substrate through 4 small metallic pipes connecting the hopper and DMD nozzle. Powder eventually reached the nozzle and was melted and deposited on the substrate by the CO_2 laser beam. Figure 3.10 shows the experimental set-up for the DMD process. DMD experiments were carried out at various process conditions by varying the laser power, scanning speed, and powder feed rate. Table 3.8 shows the DMD process conditions used in this study.

Table 3.7: Element compositions of Inconel 718 powder.

	Ni	Cr	Fe	Nb+Ta	Mo	Ti	Al
wt %	53.5	19	18	5	3	1	0.5

Table 3.8: DMD process conditions for spectroscopic study.

Exp No.	Laser power (W)	Laser scanning speed (in/min)	Powder feed rate (g/min)	Shielding gas pressure (Psi)
1	400	12	3.2	30
2	500	12	3.2	30
3	600	12	3.2	30
4	500	12	4.8	30
5	500	12	6	30
6	500	9	3.2	30

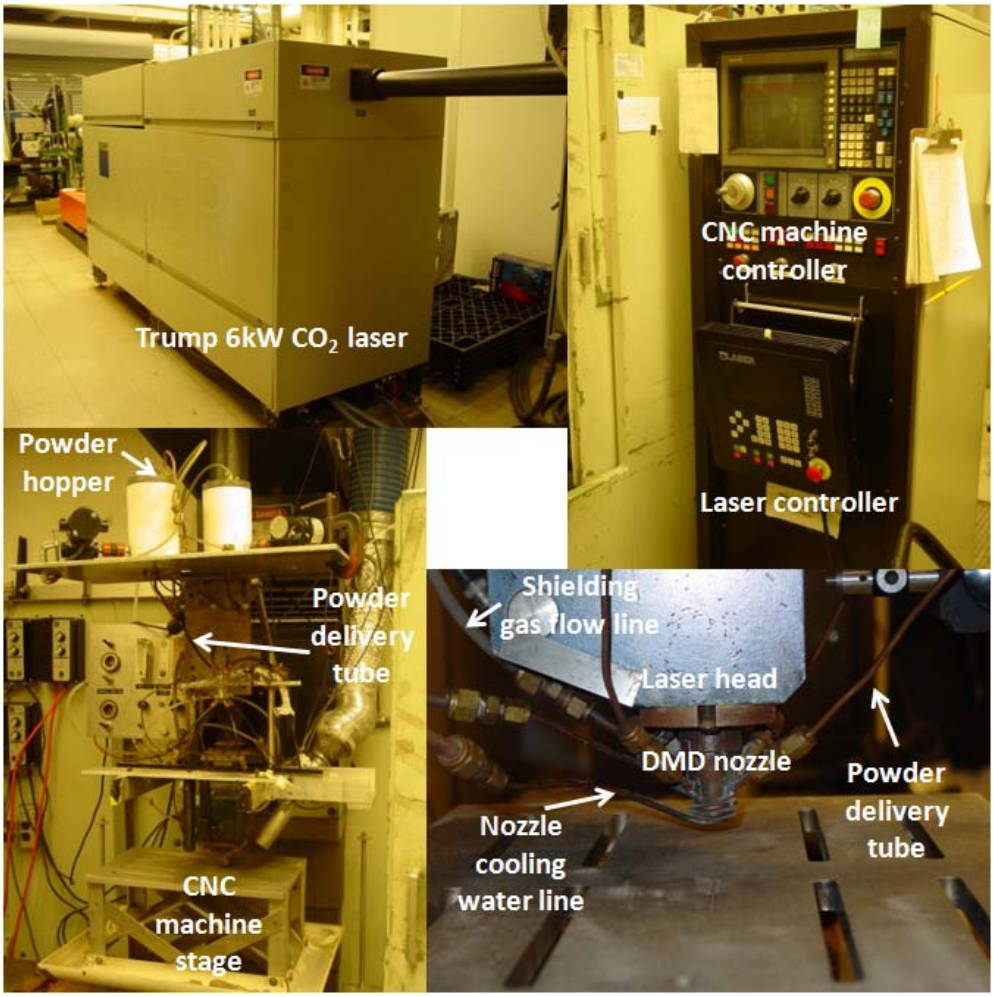

Figure 3.10: Experimental set-up for the DMD process.

A similar emission spectroscopy set-up as described in the laser drilling section (section 3.4.1) was used again; however, the spectrometer used in the DMD process covered a wavelength range of 270-470 nm. The collimating lens was positioned ~ 22 cm away from the center of the laser nozzle. The direction of the plasma observation was normal to the moving direction of the substrate. The center of the collimating lens was located just above the substrate. Single layers of ~2.5 cm length were deposited on the substrate. During the deposition process, emission spectra were consecutively recorded with a 20 ms integration time until the process was completed. Figure 3.11 shows the schematic diagram of the experimental setup used for plasma diagnostics in the DMD process.

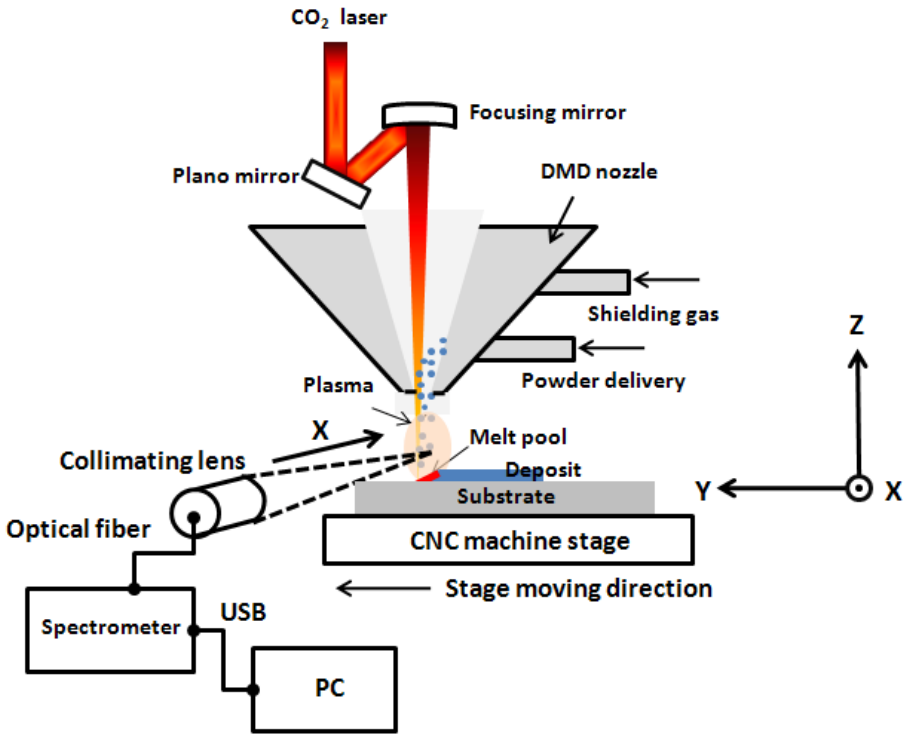

Figure 3.11: Schematic diagram of the experimental set-up for plasma diagnostics during the DMD process.

For monitoring the composition, the ratio of emission line intensities obtained from the DMD plasma were correlated to the ratio of the elemental composition of deposits. The correlations of two parameters: 1) the ratio of line intensity, and 2) the ratio of elemental composition, were developed by employing a dimensionless number composed of the process parameters and material property of Inconel 718 (see section 4.4.2). The line intensity used to determine the quantitative ratio is described in figure 3.12. The value of the intensity was obtained by subtracting the continuum intensity from the peak value of the spectral line. The average of the intensity obtained at two ends of the spectral line was considered as the continuum intensity associated with the peak.

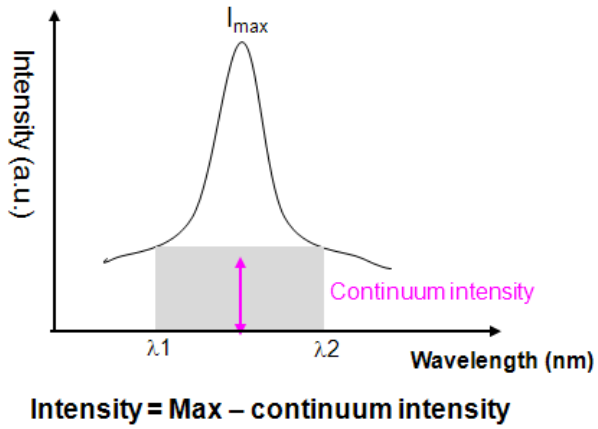

Figure 3.12: Definition of the line intensity used to determine quantitative ratios.

After experiments were completed, the top sides of DMD samples were ground to obtain the compositional data of deposits. Elemental composition data of the samples was acquired by an energy dispersive spectrometer (EDS) attached on the scanning electron microscope (SEM, Phillips XL 30FEG). An EDS scan was carried out every 0.5 mm along the deposited layer with an electron beam of 15 eV energy.

3.5 Numerical simulation of pulsed laser drilling

As mentioned previously, laser-material interaction involves a series of complicated phenomena. The relevant laser-material interaction model with associated physics is necessary to predict interaction phenomena correctly. Over the past three decades, many laser-material interaction models have been developed by many researchers from around the world; however, most models overly simplified important process physics.

A novel self-consistent laser drilling model based on the two-dimensional axisymmetric condition was first developed by Ki at the University of Michigan [95, 96]. This model considered heat transfer, liquid flow, multiple internal reflections of laser beams, and transient motion of the liquid-vapor interface. In this model, the evolution of the liquid–vapor interface is self-consistently traced by employing a mathematical technique called, the level-set method. The key idea of this model is to use all important mass loss mechanisms as the source to capture a drilled-hole profile.

In this research, the model is developed further for studying the process of pulsed laser drilling. The model by Ki was originally developed to simulate CW laser drilling process by assuming a semi-steady-state condition because the time to reach the melting point is generally very small compared to the whole drilling time, and the process is continuous. As a result, the liquid layer bounded by two interfaces, the solid/liquid interface and the liquid/vapor interface, always exists for the entire drilling process; however, in pulsed laser-material interaction, the time to reach the melting point may not be small enough compared to the laser irradiation time because of the short pulse width; therefore, the semi-steady-state condition used in the CW laser drilling process is not applicable in the pulsed laser drilling process. In addition, the solidification due to rapid cooling may

occur between the pulses, depending on the process parameter. The contribution of this study is that the numerical algorithms associated with the pulsed drilling process are incorporated in the model. The following is an overview of fundamental governing equations, details of their implementation, and modifications made for the current study.

3.5.1 Level-set method to track the liquid and vapor (L/V) interface

During laser-material interaction, the L/V interface is formed when temperature exceeds the boiling point of material. The shape of the L/V interface is sharp, unlike the solid-liquid (S/L) interface, and it is affected by physical factors such as surface tension, thermo-capillary forces, and recoil pressure. In order to account for the interaction between the interface shape and the process physics, a method to track the free surface (L/V interface) accurately is needed.

Tracking the moving L/V interface is a difficult task. Geometric complexities such as merging and splitting of multiple surfaces is very difficult for some well known front tracking methods such as the volume of fluid (VOF), the particle or node tracking method, and the cell and marker method; however, the level-set method developed by Osher and Sethian [98] has been very successful in tracking complex free surface movement. This method was adopted by Ki [95, 96] to track the L/V interface in his work.

The great advantage of the level-set method is that it transforms an interface tracking problem into a partial differential equation. Since the solution algorithms for partial differential equations are generally well known, the implementation of this method is relatively easy. In addition, geometric properties such as the surface normal and curvature can be easily obtained from the level-set values. This is very important since the surface

normal and curvature are the factors determining physically important variables at the L/V interface. Technical details and ideas are summarized below.

In order to implement this method, an interface shape function, level-set function, ϕ is defined over the entire domain as follows,

$$\phi = \phi(x,y,z,t) = \pm d, \tag{3-2}$$

where d is the constant value denoting the distance from the interface of interest (i.e. the L/V interface). d is zero for the L/V interface (zero level set, ϕ_o). The positive and negative signs denote above and below (or outside and inside for a closed interface) the interface, respectively. Figure 3.13 shows an example of the level set function.

Since d is a constant, the material derivative of the level set function has the following form.

$$\frac{D\phi}{Dt} = 0 = \frac{\partial \phi}{\partial t} + \mathbf{u} \cdot \nabla \phi \tag{3-3}$$

.

The normal to the L/V interface, **n**, is calculated as $\mathbf{n} = \frac{\nabla \phi}{|\nabla \phi|}$. Rearranging the above equation with **n**, the Eq. 3-3 becomes

$$\frac{\partial \phi}{\partial t} + \mathbf{u} \cdot \mathbf{n} |\nabla \phi| = 0 \tag{3-4}$$

.

Here, $\mathbf{u}\cdot\mathbf{n}$ is the force function (or speed function) acting in the normal direction of the L/V interface and is written as F. Thus, we have

$$\frac{\partial \phi}{\partial t} + F\left|\nabla \phi\right| = 0 \tag{3-5}$$

In high power density laser-material interactions such as laser drilling, the motion of the L/V interface can be affected by two factors. First, evaporation causes the L/V interface to recede in the normal direction, and its contribution is noted as F_e. Also, the melt flow can change the L/V interface to satisfy mass conservation. The effect from this is expressed as F_f. Thus, the final form of the level set equation for laser drilling is

$$\frac{\partial \phi}{\partial t} + \left(F_e + F_f\right)\left|\nabla \phi\right| = 0 \tag{3-6}$$

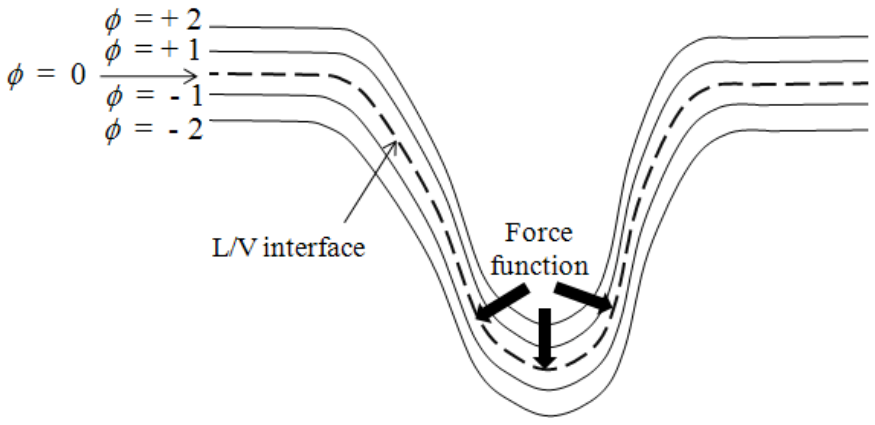

Figure 3.13: Level set method to track L/V interface.

3.5.2 Mass and energy balance

Figure 3.14 shows a schematic diagram of the mass and energy balance used in this model.

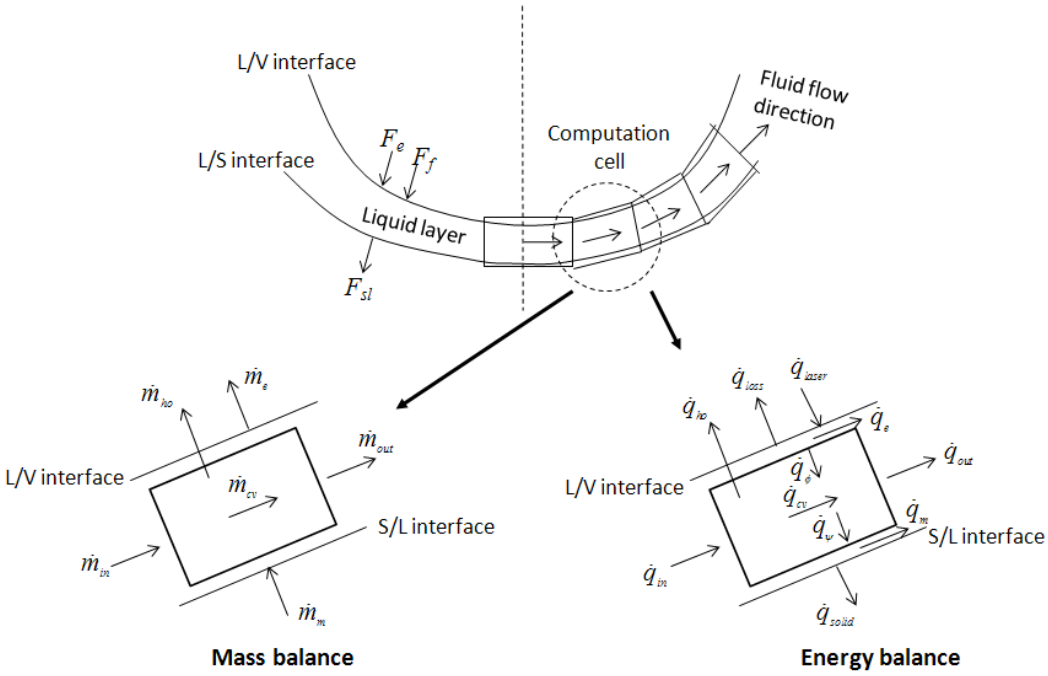

Figure 3.14: Mass and energy balance over a cell.

The mass balance can be expressed as

$$\dot{m}_{\mathrm{cv}} = \left(\dot{m}_{\mathrm{m}} + \dot{m}_{\mathrm{in}}\right) - \left(\dot{m}_{\mathrm{out}} + \dot{m}_{\mathrm{e}} + \dot{m}_{\mathrm{ho}}\right), \tag{3-7}$$

where $\dot{m}_{in}$ and $\dot{m}_{out}$ are the mass flow rates due to fluid flow at the entrance and exit of the computational cell, respectively. They are obtained from the fluid flow equation (section 3.5.5). $\dot{m}_{ho}$ is amount of mass loss due to homogeneous boiling, which will be

discussed in section 3.5.4. $\dot{m}_m$ is the mass flux into the liquid layer due to melting and can be expressed as

$$\dot{m}_m = \rho_s A F_{sl}, \tag{3-8}$$

where ρ_s, A and F_{sl} are the solid density, the bottom area of the cell, and melting speed, respectively. $\dot{m}_e$ is the evaporation mass flux at the L/V interface and is expressed as

$$\dot{m}_e = \rho_l A F_e, \tag{3-9}$$

where ρ_l is the liquid density and F_e is the speed function due to evaporation. $\dot{m}_{\text{cv}}$ is the mass accumulation rate in the computational cell and can be expressed as

$$\dot{m}_{cv} = \rho_l A \dot{d}, \tag{3-10}$$

where $\dot{d}$ is the rate of increase in the liquid layer thickness.

The energy balance for a cell has the same form as the mass balance and is written as

$$\dot{q}_{\text{cv}} = \left(\dot{q}_\phi + \dot{q}_{in}\right) - \left(\dot{q}_\psi + \dot{q}_{out} + \dot{q}_{ho}\right), \tag{3-11}$$

where $\dot{q}_{in}$ and $\dot{q}_{out}$ are the energy fluxes at the inlet and outlet of a cell due to fluid flow, respectively. $\dot{q}_{ho}$ denotes the heat loss due to homogeneous boiling. $\dot{q}_{\phi}$ is the heat transmitted to the liquid layer through the L/V interface and can be expressed by employing Stefan's condition to describe discontinuity in energy flow due to latent heat at the L/V interface

$$\dot{q}_{\phi} = -k_l \left.\frac{\partial T_l}{\partial n}\right|_{\phi} = \dot{q}_{loss} + \dot{q}_e - \dot{q}_{laser} = \dot{q}_{loss} + \rho_l L_v F_e - \dot{q}_{laser} \quad (3\text{-}12)$$

where L_v and $\partial/\partial n$ are the latent heat of vaporization and the directional derivative normal to the surface, respectively. $\dot{q}_{laser}$ is the laser energy applied to the L/V interface and is expressed as follows by assuming the Gaussian beam profile.

$$\dot{q}_{laser} = I(r) = I_o exp\left(-\frac{2r^2}{R_b^2}\right), \quad (3\text{-}13)$$

where I_o and R_b are the centerline laser intensity and the beam radius, respectively. $\dot{q}_{loss}$ is the heat loss to the atmosphere due to the radiation and convection.

Stefan's condition at the S/L interface can be written as follows

$$\dot{q}_{\psi} = -k_l \left.\frac{\partial T_l}{\partial n}\right|_{\psi} = \dot{q}_m + \dot{q}_{solid} = \rho_s L_m F_{sl} - k_s \left.\frac{\partial T_s}{\partial n}\right|_{\psi}, \quad (3\text{-}14)$$

where L_m is the latent heat of fusion, and $\dot{q}_{solid}$ denotes the heat loss to the solid region. The temperature profile of the solid region can be modeled using an analytical solution for a semi-infinite solid with a moving boundary as follows [95, 96].

$$T(n) = T_o + \left(T_m - T_o\right) exp\left(-\frac{F_{sl}}{\alpha_s} n\right) . \tag{3-15}$$

Therefore, $\dot{q}_{solid}$ is expressed as

$$\dot{q}_{solid} = -k_s \left.\frac{\partial T_s}{\partial n}\right|_{\psi} = k_s \left(T_m - T_o\right) \frac{F_{sl}}{\alpha_s} . \tag{3-16}$$

$\dot{q}_{cv}$ is the heat accumulation rate in the cell which accounts for the temperature variation with time and can be expressed as

$$\dot{q}_{cv} = \rho_l A d C_{pl} \frac{\mathrm{d}T_{mean}}{\mathrm{d}t} , \tag{3-17}$$

where $\mathrm{d}T_{mean}/\mathrm{d}t$ is the time rate of mean liquid temperature increase and C_{pl} is the specific heat for liquid. Since the temperature profile in the liquid layer is determined from four values such as the L/V and S/L interface temperatures and the temperature gradients at the liquid side of both interfaces, a cubic polynomial is assumed to interpolate the temperature profiles. From this, the following relation is obtained

$$\left.\frac{\mathrm{d}T}{\mathrm{d}t}\right|_{\phi} = 2\frac{\mathrm{d}T_{mean}}{\mathrm{d}t} \quad (3\text{-}18)$$

Eq. 3-18 is used to update the L/V interface temperature continuously.

3.5.3 Evaporation at the L/V interface

When temperature at the L/V interface reaches a boiling point, evaporation begins to occur. A very thin layer of several mean free paths, called a kinetic Knudsen layer, exists just outside the L/V interface. Across this layer, the continuum hypothesis is not valid any more, and a steep change in temperature, pressure, and density occurs. In order to describe this mathematical discontinuity, Knight [99] derived jump conditions with back pressure and Ki adopted this in his previous work [95, 96].

According to [95, 96], net mass loss due to evaporation is

$$\dot{m}''_{evap} = \rho_s\sqrt{\frac{RT_s}{2\pi}} - \rho_v\sqrt{\frac{RT_v}{2\pi}}\beta F_{-}(m) = \rho_l F_{evap}\,, \quad (3\text{-}19)$$

where

$$\beta = \frac{2(2m^2+1)\sqrt{\frac{T_v}{T_s}} - 2\sqrt{\pi}m}{F_{-} + \sqrt{\frac{T_v}{T_s}}G_{-}} \quad (3\text{-}20)$$

$$F_{-} = \sqrt{\pi}m(-1 + erf(m)) + \exp(-m^2) \quad (3\text{-}21)$$

$$G_{-} = (2m^2+1)(1 - erf(m)) - \frac{2}{\sqrt{m}}m\exp(-m^2)\,. \quad (3\text{-}22)$$

R is ideal gas constant. F_{evap} is the force function acting on the L/V interface due to evaporation. More detailed information on this topic can be found in [95, 96].

3.5.4 Homogeneous boiling

When the laser intensity is high enough, the L/V interface temperature far exceeds the normal boiling temperature and it approaches a maximum temperature (called the "critical point temperature") that a liquid metal can attain. Right beneath the L/V interface, homogeneous boiling starts to occur when the interface temperature reaches approximately 80 % of the critical point. As a result, the homogeneous boiling process acts as a heat sink, causing the liquid metal temperature to saturate. [95, 96].

During boiling, the critical radius of a bubble, r_e, can be calculated from the following expression

$$r_e = \frac{2\sigma}{P_{sat}(T_l)\exp\left[v_l\left(P_l - P_{sat}(T_l)\right)/RT_l\right] - P_l}. \tag{3-23}$$

Here, T_l, P_l, v_l, σ and R are the liquid temperature, the liquid pressure, the specific volume of liquid, the surface tension and the gas constant, respectively. $P_{sat}(T_l)$ is saturation pressure at T_l, and calculated from the Clausius-Claperyron equation [100]:

$$P_{sat}(T_l) = P_{atm}\exp\left[\frac{L_v\left(T_l - T_b\right)}{RT_bT_l}\right], \tag{3-24}$$

where P_{atm} and T_b are the atmospheric pressure and boiling temperature, respectively.

The pressure inside the bubble, P_v and the specific volume of the bubble, v_v, can be found from

$$P_v = P_l + \frac{2\sigma}{r_e} \tag{3-25}$$

$$P_r = \frac{8T_r}{3v_r - 1} - \frac{3}{v_r^2}\,. \tag{3-26}$$

Here, $P_r=P_v/P_{cr}$, $T_r=T_v/T_{cr}$ and $v_r=v_v/v_{cr}$. The subscript *cr* denotes the critical point state.

The homogeneous evaporation rate, which is the number of bubbles with critical radius per unit time per unit volume of liquid, can be computed from

$$J = N_l \left[\frac{6\sigma}{\pi m \left(2 - P_l/P_v\right)} \right]^{1/2} \exp\left[\frac{-4\pi r_e^2 \sigma}{3k_B T_l} \right], \tag{3-27}$$

where N_l, m, k_B are the number of liquid molecules per unit volume, the mass of one molecule, and the Boltzmann constant (k_B=1.3807×10^{-23} J/K), respectively.

The number of molecules in the bubble, n_e, and the volume of the bubble, V_d, are expressed as

$$n_e = \frac{V_d N_A}{v_v \overline{M}} \tag{3-28}$$

$$V_d = \frac{4}{3}\pi r_e^3, \tag{3-29}$$

where N_A is Avogadro's number, and $\overline{M}$ is the molecular mass. Mass loss, $\dot{m}'''_{homo}$, and energy loss, $\dot{q}'''_{homo}$, due to homogeneous bubble generation near the critical point are expressed as follows:

$$\dot{m}'''_{homo} = Jn_e m_m \tag{3-30}$$

$$\dot{q}'''_{homo} \cong Jn_e\left(\frac{3}{2}k_B T + m_m L_v + \frac{4}{3}\pi\sigma r_e^2\right), \tag{3-31}$$

where m_m is the atomic mass. Finally, the contribution of the force function (or surface recession speed) due to the homogeneous boiling is determined by

$$F_{homo} = \frac{\dot{m}'''_{homo} d\Omega}{\rho_l d\Gamma}, \tag{3-32}$$

where $d\Omega$ and $d\Gamma$ are the volume and area elements of the computational cell contributing to homogeneous boiling.

3.5.5 Fluid flow model

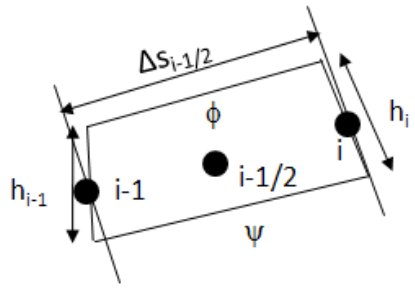

Figure 3.15: Computational cell for deriving the velocity.

Fluid flow is one of the most difficult parts to model in laser material processing. In the case of the high power density laser-material interaction, the liquid layer produced is generally very thin and the fluid model can be simplified by applying the boundary layer approximation. A simplification on the fluid flow in the liquid layer was made by integrating the Navier-Stokes equation over a computational cell along the liquid layer as follows (see figure. 3.15).

$$\frac{\partial u_s}{\partial t} ds + \frac{\partial}{\partial s}\left(\frac{1}{2} u_s^2\right) ds = -\frac{1}{\rho}\frac{\partial p}{\partial s} ds + \left(\nu \nabla^2 u\right) ds \,. \tag{3-33}$$

The above equation is a simplified transient equation for fluid velocity. The discretized form of the equation is shown below.

$$\frac{1}{\lambda}\frac{\overline{\mathrm{d}v}}{\mathrm{d}t}\bigg|_{i-1/2}^{n+1} = \frac{1}{2}\rho_{i-1/2}\left(\overline{\left(v_{i-1}^n\right)}^2 - \overline{\left(v_i^n\right)}^2\right) + \left(p_{i-1}^n - p_i^n\right)$$

$$+\frac{\Delta s_{i-1/2}^{n}}{h_{i-1/2}^{n}}\left[\mu_{i-1/2}\left.\frac{\partial u}{\partial n}\right|_{\phi,i-1/2}^{n}-\mu_{i-1/2}\left.\frac{\partial u}{\partial n}\right|_{\psi,i-1/2}^{n}\right], \tag{3-34}$$

where $\lambda=\dfrac{1}{\rho_{i-1/2}\Delta s_{i-1/2}^{n}}$. (3-35)

Here, the superscript *n* and subscript *i* are used for time and space, respectively. The bars over each variable denote average values across the liquid layer. The velocity gradient at the L/V interface is expressed as

$$\mu_{i-1/2}\left.\frac{\partial u}{\partial n}\right|_{\phi,i-1/2}^{n}=\left.\frac{d\sigma}{dT}\right|_{i-1/2}^{n}\left.\frac{dT}{ds}\right|_{i-1/2}^{n}, \tag{3-36}$$

where σ denotes surface tension. The velocity gradient at the S/L interface and the averaged velocity in Eq. 3-34 can be obtained by assuming the velocity profile in the liquid layer to be a quadratic polynomial as follows:

$$v(n)=\frac{1}{2h_{i}^{n}}\left[\left.\frac{du}{dn}\right|_{\phi,i}^{n}-\left.\frac{du}{dn}\right|_{\psi,i}^{n}\right]n^{2}+\left.\frac{du}{dn}\right|_{\psi,i}n. \tag{3-37}$$

Then, the velocity at the center of the cell can be updated from the following relationship:

$$\overline{v_{i\text{-}1/2}^{n+1}}=\overline{v_{i\text{-}1/2}^{n}}+\left.\frac{\overline{dv}}{dt}\right|_{i-1/2}^{n+1}\Delta t. \tag{3-38}$$

Here, Δt is the time step.

3.5.6 Modifications made for the current work

As mentioned earlier, the original model [95, 96] was developed to simulate a continuous wave (CW) laser drilling process. In this model, the process is continuous, and material continuously melts without solidification. A thin liquid layer is assumed to exist at the start point of the process; therefore, it cannot be used directly to simulate the pulsed laser-material interaction where the process is not continuous any more. In this study, the original model has been modified so that it can describe pulsed laser drilling. In pulsed laser, the time to reach the melting point may not be small enough compared to the laser irradiation time depending on process parameters; therefore, assuming the existence of the thin liquid layer at the start point of the process as was done for the CW laser drilling process would be inappropriate. In this case, considering transient heat conduction process will be necessary during the initial heating stage of the material. The following analytic solution [101] is used to find the temperature history in the solid surface before melting occurs

$$T = T_o + \frac{q''_{laser} 2\sqrt{t/D}}{\sqrt{\pi \rho_s C_{ps} k_s / D}}, \tag{3-39}$$

where D is the pulse width. Once the surface temperature reaches the melting point, equations presented in section 3.5.2 are used to solve the mass and energy balance problems continuously.

During a pulse-off period, the melted area cools rapidly, and the liquid zone could fully solidify depending on process parameters. In this work, algorithms during the pulse-

off period have been incorporated into the model. The mass and energy balance equations presented in section 3.5.2 are used to update the temperature field during the cooling process when the temperature is higher than the melting point. During cooling, the solidification process is assumed to be complete when the temperature is less than the melting point. In the solidification process, the S/L and L/V interfaces merge together to form a new solid/vapor (S/V) interface.

When the temperature drops below the melting point, cooling could still occur in the solid region. The equations presented below are used to describe the cooling history due to radiative and convective heat loss in the solid region [101].

$$A_1 ln\frac{(\tau - r_1)}{(1-r_1)}2 + A_2 ln\frac{(\tau - r_2)}{(1-r_2)} + \frac{A_3}{2} ln\frac{(\tau-\eta)^2+\phi^2}{(1-\eta)^2+\phi^2} + \frac{A_4}{\phi}\left(tan^{-1}\frac{\tau-\eta}{\phi} - tan^{-1}\frac{1-\eta}{\phi}\right) = MF \quad (3\text{-}40)$$

,

where

$$\tau = T/T_i \quad (3\text{-}41) \qquad F = \alpha t/\delta^2 \quad (3\text{-}42) \qquad M = \sigma\varepsilon T_i \delta/k \quad (3\text{-}43)$$

$$A_1 = \frac{1}{8\sqrt{\nu-\eta^2}\left[\eta\sqrt{\nu-\eta^2} + \left(\nu/2+\eta^2\right)\right]} \quad (3\text{-}44)$$

$$A_2 = \frac{1}{8\sqrt{\nu-\eta^2}\left[\eta\sqrt{\nu-\eta^2} - \left(\nu/2+\eta^2\right)\right]} \quad (3\text{-}45)$$

$$A_3 = \frac{\eta}{\nu^2+8\eta^4} \quad (3\text{-}46) \qquad A_4 = \frac{\nu/2-\eta^2}{\nu^2+8\eta^4} \quad (3\text{-}47)$$

$$r_1 = -\eta - \sqrt{\nu-\eta^2} \quad (3\text{-}48) \qquad r_2 = -\eta + \sqrt{\nu-\eta^2} \quad (3\text{-}49)$$

$$\phi = \sqrt{\nu + \frac{\kappa}{4}} \quad (3\text{-}50) \qquad \eta = \frac{\sqrt{\kappa}}{2} \quad (3\text{-}51) \qquad \nu = \sqrt{N_2^4 + \frac{\kappa^2}{4}} \quad (3\text{-}52)$$

$$\kappa = \left(\frac{S^2}{2} + \sqrt{\frac{S^4}{4} + \frac{64}{27} N_2^{12}} \right)^{1/3} + \left(\frac{S^2}{2} - \sqrt{\frac{S^4}{4} + \frac{64}{27} N_2^{12}} \right)^{1/3} \qquad (3\text{-}53)$$

$$S = \frac{h}{\sigma \varepsilon T_i^3} \qquad (3\text{-}54) \qquad N_2 = \left(\left(T/T_a \right)^4 + S\,T/T_a \right)^{1/4} \qquad (3\text{-}55)$$

Here, T_i is the initial surface temperature (melting temp), T_a is the environment temperature, t is the time, α is the thermal diffusivity, k is the thermal conductivity, h is the convection coefficient, σ is the Stefan Boltzmann constant, ε is the emissivity, and δ is the thickness of the material. Eq. 3-40 is a non-linear equation. In order to obtain temperature data at a given time, an iterative root-finding method (the bisection method) is employed. The material selected for numerical study is: Inconel 718. Thermophysical properties for this material are listed in Table 3.9. For high temperatures, some important properties are extrapolated to the critical point using the experimental data and theoretically known material behavior from various references [31, 102-105].

Table 3.9: Material properties for Ni superalloy (Reference [31, 102-105]).

Property, symbol (unit)	Value
Melting temperature, T_m (K)	1728
Boiling temperature, T_b (K)	3188
Critical point temperature, T_{cr} (K)	9100
Critical point pressure, P_{cr} (Pa)	9.0E8
Solid thermal conductivity, k_s (W/m-K)	23.57
Liquid thermal conductivity, k_l (W/m-K)	24.32
Solid density, ρ_s (kg/m^3)	7681.71
Density for liquid and vapour, ρ_{lv} (kg/m^3) [102]	(1) 0.058028154/(8.02441E-6 + 1.01702E-9(T-1620.78)) + 34.9 for $T<T_b$ (2) 8497.75596 - 0.79419T+(6.8935E-6)T^2 for $T_b \leq T < T_{cr}$
Solid constant-pressure specific heat, C_{ps} (J/kg K)	596.9
Liquid constant-pressure specific heat, C_{pl} (J/kg K)	743.1
Solid thermal diffusivity, α_s (m^2/sec)	5.14 E-6
Latent heat of fusion, L_m (J/kg)	2.92 E5
Latent heat of vaporization, L_v (J/kg)	6.4 E6
Viscosity, μ (kg/sec-m)	4.644773 E-3
Surface tension, σ (N/m) [102, 105]	(1) 0.001(1798.33-0.4(T-1650)) for $T < T_b$ (2) 2.54433 -4.70355E-4T+1.10948E-8T^2+1.08679E-12T^3 for $T_b \leq T < 0.9T_{cr}$ (3) (1.-1.0989E-4T)$^{3/2}$ for $0.9T_{cr} < T \leq T_{cr}$
Laser absorptivity for flat surface, A_o	0.27
Liquid enthalpy, h_l (J/kg) [102]	791275.87 + 734.0953(T-1620.78)

CHAPTER 4

RESULTS AND DISCUSSIONS

This chapter presents the results and discussion for this study.

4.1 Pulsed laser deposition of yttira-stabilzed zriconia (YSZ)

4.1.1 Investigation of the surface morphology

Figure 4.1 shows AFM surface images of the YSZ films deposited at different oxygen pressures from 6.67×10^{-1} to 133.32×10^{-1} Pa. Images on the left hand side of this figure show 2-dimensional AFM images of the film surfaces, and images on the right hand side are the surface profiles at the cross sections marked by solid lines in the figures on the left. The YSZ film surfaces shown in the figures have a distinct peak and valley structure, though the shape and size of the peaks and distribution of peaks and valleys of each film sample are different.

The morphological features of the film could be explained by the film growth mechanism introduced in reference [64]. Initially, monomers from the plasma of the evaporated plume are adsorbed and condensed on a substrate, and they play as seeds for nucleation at energy-favorable sites. As theses nuclei grow, neighboring nuclei combine

with each other to form clusters. Subsequently, these clusters grow together to form larger three-dimensional clusters or islands, which produces a wave-like film surface structure. When these islands eventually coalesce, they form a continuous film. These morphological features of the YSZ film surface were also observed in high magnification SEM image as shown in figure 4.2.

The relative height difference between peaks and valleys shown in the cross sections in figure 4.1 is generally 10–30 nm. The film formed under an oxygen gas pressure of

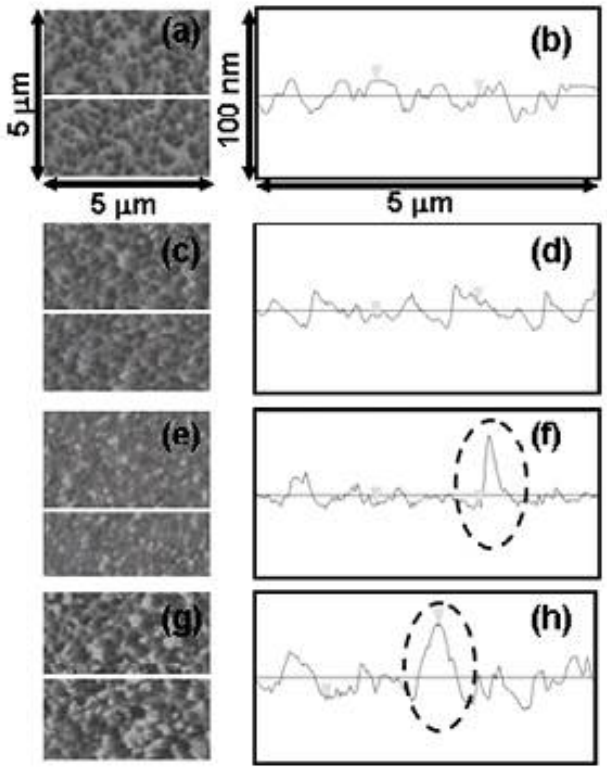

Figure 4.1: Top view of the film surface (left) and surface profile (right) at the sections marked by solid lines in (a), (c), (e) and (g): (a) and (b) O_2 pressure of 6.67×10^{-1} Pa, (c) and (d) O_2 pressure of 26.66×10^{-1} Pa, (e) and (f) O_2 pressure of 66.66×10^{-1} Pa and (g) and (h) O_2 pressure of 133.32×10^{-1} Pa.

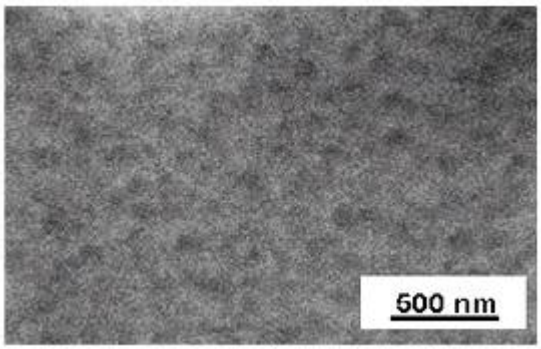

Figure 4.2: High magnification SEM image of the YSZ film surface (deposited at O_2 pressure of 66.66×10^{-1} Pa, magnification: 40,000×).

66.66×10^{-1} Pa has the smoothest surface profile as shown in figure 4.1(f); however, there are some peaks in the surface profiles shown in figure 4.1 that much higher than the rest of the films. These high peaks are enclosed by circles in the figure 4.1. The relative height difference of theses high peaks is approximately 50–60 nm. Since theses high peaks can locally increase the roughness of the film surface, they could contribute to a lower film quality; therefore, these peaks need to be reduced by selecting appropriate processing parameters. Local deposition of particulates, which results from liquid expulsion during laser ablation[20] can produce particle from several tens to several hundreds of nano-meters, could lead to these high peaks. In addition, deposition of condensed particles could be another possible source to form high peaks. In this study, these high peaks were found at relatively high oxygen gas pressure above 66.66×10^{-1} Pa. This indicates that high peaks are more likely produced by deposition of

the condensed materials due to the enhanced interaction between vapor particles and oxygen gas at high pressures.

Figure 4.3 shows the root mean square roughness of surfaces of the four film samples deposited as a function of oxygen gas pressure. The measured roughness is in the range of 3.5–6.5 nm which is ~ 1% of the film thickness (600–1000 nm). The roughness initially tends to decrease as oxygen gas pressure increases and has the lowest point at 66.66×10^{-1} Pa O_2 pressure. However, a significant increase occurs at an oxygen gas pressure of 133.32×10^{-1} Pa. This result is consistent with the AFM results shown in figure 4.1.

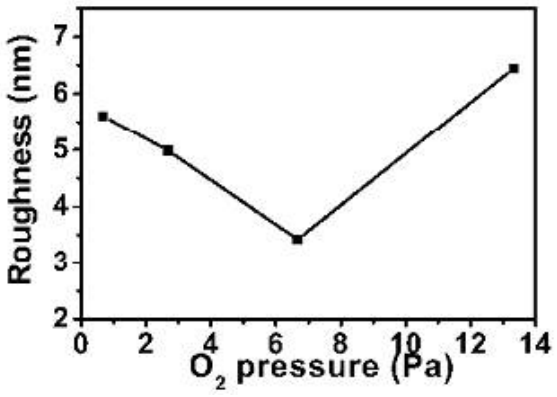

Figure 4.3: Surface root mean square roughness of the YSZ films deposited at different O_2 pressures.

As shown in figure 4.1, the surface of the film produced at low oxygen pressure has relatively big islands, leading to larger roughness than other samples; however, the size of the peaks and the number of distributed peaks tend to decrease with increasing oxygen gas pressure. Compared to the films shown in figure 4.1 (b) and (d), the film developed at

oxygen gas pressure of 66.66×10^{-1} Pa does not show a clear distinction between peaks and valleys. It seems that this film has a quite smooth surface on the whole. As shown in figure 4.3, the film produced at this pressure actually has the smallest roughness, and section analysis for this film (figure 4.1 (f)) also shows the smoothest surface profile with the exception of one high peak.

The increase of the roughness at the highest oxygen pressure, 133.32×10^{-1} Pa, is attributable to deposition of condensed materials. Yamamoto [106] reported that above 1.0 Torr (133.32×10^{-1} Pa), larger particles were deposited at higher pressure due to enhanced condensation of vapor particles. In general, as ambient gas pressure increases, zirconium ions and evaporated atoms in the plasma plume collide more frequently with oxygen molecules because of the reduced mean free path of gas particles. Above some threshold value of ambient gas pressure, evaporated particles lose their kinetic energy rapidly and are cooled down below a certain temperature due to the enhanced collision process, which results in condensation of vapor before it arrives at the substrate. The fine materials formed by this condensation mechanism within the plasma plume are finally deposited on the substrate together with evaporated atoms and ions. The film with great surface roughness was to be the result of the increased production of theses large particles.

4.1.2 Investigation of mechanical properties

Nano-indentation testing for the samples developed under different oxygen gas pressures was carried out. The applied maximum load for indentation was 60,000 μN. Six independent tests were conducted for each film. Figure 4.4 shows the indentation test results of the films deposited at different oxygen pressures. The Young's modulus and

hardness of the films were determined to be approximately 86–95 GPa and 10–11 GPa, respectively. The hardness of the YSZ films shown in this study is larger than that of the YSZ coatings produced by the plasma-spraying (8.6 GPa [107] and 5–11 GPa [37]). The superior mechanical properties of YSZ films produced by PLD are attributed to the dense microstructure of the deposited materials without pores and microcracks, which are normally present in plasma-sprayed YSZ coatings [9]. The microstructure of the YSZ film produced in this study can be seen in an SEM image of the film cross-section (figure 4.5).

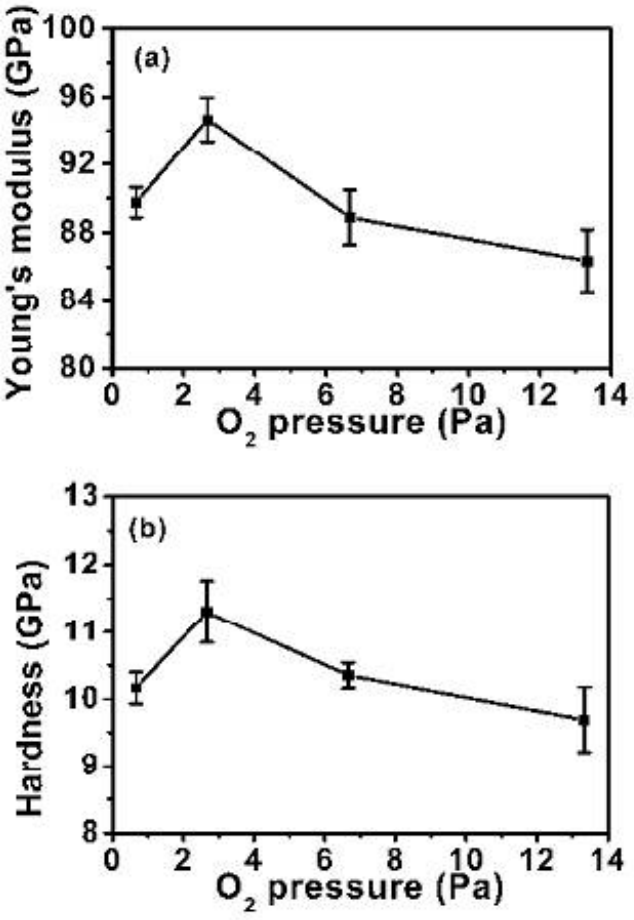

Figure 4.4: Mechanical properties of the YSZ films deposited at different O_2 pressures: (a) Young's modulus and (b) hardness.

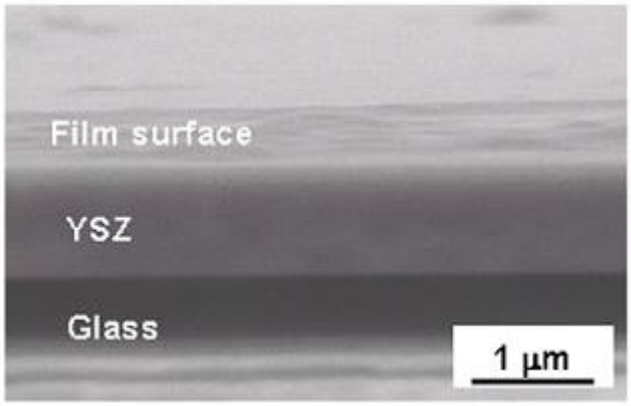

Figure 4.5: Cross-sectional SEM image of the YSZ film (deposited at O_2 pressure of 26.66×10^{-1} Pa, magnification: 2418×).

4.1.3 Composition analysis

The elemental composition of the deposited films was analyzed by electron probe micro-analyzer (EPMA). Figure 4.6 shows the O/Zr ratio of the films deposited at different oxygen gas pressures. The result is average values of O/Zr ratios measured at five different sites on the films. It is revealed that O/Zr of the target material is generally well preserved in the films. In particular, the O/Zr ratio (O/Zr ratio is determined by the atomic percentage of O and Zr in the film) of the films deposited for oxygen pressures between 6.67×10^{-1} and 66.66×10^{-1} Pa is quite close to that of the target material (difference within $\sim 1.5\%$); however, $\sim 4.5\%$ increase of O/Zr ratio compared to the target material is observed for the film deposited at the highest oxygen pressure of 133.32×10^{-1} Pa. Increase in oxygen content in the films with increasing oxygen pressure could be ascribed to enhanced oxygen diffusion on the deposition surface and an increase in amount of deposited oxides due to activated gas phase interactions between

zirconium ions/atoms and oxygen molecules at high O_2 pressures. According to the results from analysis of variance (ANOVA), the variance (0.012462) between levels (levels of oxygen pressure) is much larger than that (0.000164) within levels (see ANOVA table in APPENDIX A). This supports that the increase in oxygen content in the film is resulted from not a statistical difference but the enhanced oxygen diffusion at high oxygen pressures.

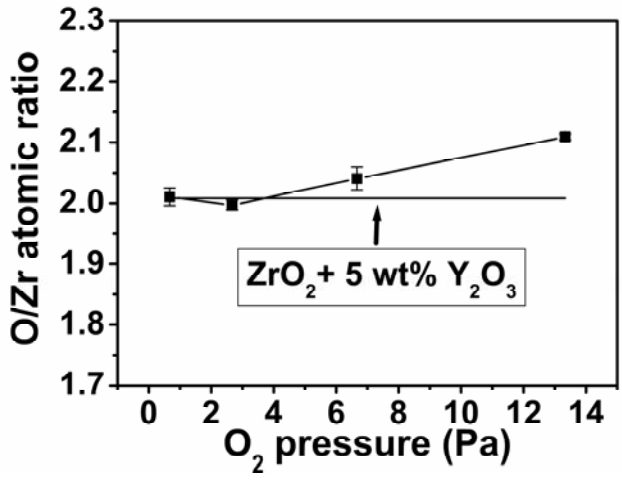

Figure 4.6: The O/Zr ratios (at%) of the YSZ films deposited at different O_2 pressures.

4.1.4 Analysis of structural characteristics

Structural characteristics of the YSZ films deposited at different oxygen pressures were determined by x-ray diffraction (XRD). From the investigation, it is revealed that the films produced in the range of oxygen gas pressure of 6.67×10^{-1}–133.32×10^{-1} Pa have three XRD peaks, where (200) is the 1st peak, (220) is the 2nd peak and (400) is the 3rd peak for cubic crystal structure. The inset of figure 4.7 shows the XRD peak pattern of one of the YSZ film samples. Figure 4.7 shows measured intensity ratios of (200) to

(220) peaks and (200) to (400) peaks for films produced at different oxygen pressures. Depending on the change in the oxygen pressure, the ratio of (200) to (400) peaks, $I_{(200)}$ /$I_{(400)}$, changes slightly and a clear difference is not seen over the measured oxygen pressures. This is probably due to the characteristic of crystal structure that (200) and (400) planes are parallel to each other. When a strong intensity peak of the (200) plane is detected by the XRD detector, there is also the chance that a strong signal of the (400)

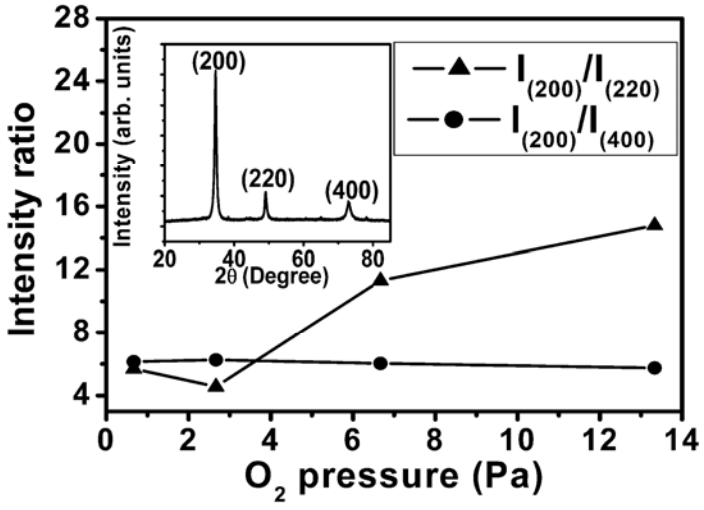

Figure 4.7: Intensity ratios of the 1st peak (200) to the 2nd (220) and 3rd (400) peaks of XRD $\theta/2\theta$ scan for the YSZ films deposited at different O_2 pressures. The inset shows XRD $\theta/2\theta$ scan for the YSZ film produced at an O_2 pressure of 26.66×10^{-1} Pa.

plane is detected. In other words, the intensities of peaks for these two planes from XRD should be proportional and consistent. On the other hand, the ratio of (200) to (220) peaks, $I_{(200)}/I_{(220)}$, varies significantly as oxygen gas pressure changes. In figures 4.6 and 4.7, it is seen that the behavior of the variation in the O/Zr ratio is analogous to that of the $I_{(200)}/I_{(220)}$ ratio. This suggests that elemental composition in the film have an effect on structural characteristics. The dependence of the measured mechanical properties (figure

4.4) with the $I_{(200)}/I_{(220)}$ ratio (figure 4.7) predicts that an increase of the (220) crystallographic orientation in the films has an influence on the enhancement of the mechanical properties. In this study, little effort to find clear reasons for the variation of the mechanical properties of the films deposited under different oxygen gas pressures has been made; however, results from the XRD and analysis of the elemental composition and mechanical properties imply that element composition have an effect on structural characteristics and mechanical properties of the YSZ films produced by PLD, and film properties can be easily changed by adjusting gas pressure in a chamber during the process.

4.2 Pulsed laser deposition of Ni-base superalloy

4.2.1 X-ray diffraction (XRD) analysis

The crystal structure of the Ni-base superalloy films deposited at different experimental conditions was analyzed by XRD in the scan range of 20-80°. Figure 4.8 shows XRD scan results of the films and the single crystal (SC) substrate. The deposited films generally exhibit a stronger polycrystalline characteristic as the substrate temperature and pulse energy increase. The (100) and (200) planes of the γ'-Ni_3Al phase with a fcc structure were observed in the SC substrate as shown in figure 4.8 (a). The XRD peak pattern obtained in the SC substrate was observed for the film deposited at the L1 condition as shown in the figure 4.8 (a). This suggests that the deposits at the L1 condition grow homoepitaxially on the SC substrate. In addition to the main γ'-Ni_3Al phase, the small peak from Ni_3Ta phase was detected in films deposited at the L2 and L3

condition which have the same substrate temperature as the L1 condition but have higher pulse energy and repetition rate than the L1 condition (see figure 4.8 (a)). In the L3 condition, the γ'-Ni_3Al phase which grows to (111) and (110) orientation was also observed.

From figure 4.8 (b), it is seen that the Ni_3Ta phase grows further in the films deposited at L4, L5 and L6 conditions. In particular, the small diffraction peaks were additionally found at 2θ angle of ~ 69.5° and ~ 73.3° in the films deposited under the L5 and L6 conditions. These are attributable to the Ni_4W, Ni_4Mo, or Ni_3Ta phase. Since the 2θ location and *d*-value of these three phases from standard data are quite close to values measured in this study, it is difficult to exactly identify these diffraction peaks. Figure 4.8 (c) and (d) show the XRD scan results of the films deposited at L7, L8 and L9 conditions. Figure 4.8 (d) is an enlarged view of the rectangular region in figure 4.8 (c). Very small peaks from the Cr_3Ni_2 phase were observed for the films deposited at the L8 and L9 conditions. These peaks were not seen in the films deposited at L1 through L7 condition.

To better understand this, it may be important to understand the effect of the substrate temperature. The role of the substrate temperature during the vapor deposition of metallic films has been previously investigated [62]. According to [62], the range of the substrate temperature used in this study corresponds to the high temperature regime (Zone III, substrate temperature > $0.5T_{melting}$) where the epitaxial growth of the deposits in the vapor-state deposition process is favorable; however, the epitaxial growth ((100) oriented growth) of the deposit only occurred at one condition (L1, 850 ^{o}C) in this study. The further increase of the substrate temperature resulted in the growth of the γ'-Ni_3Al phase with a different orientation and other phases which are not seen in the single crystal

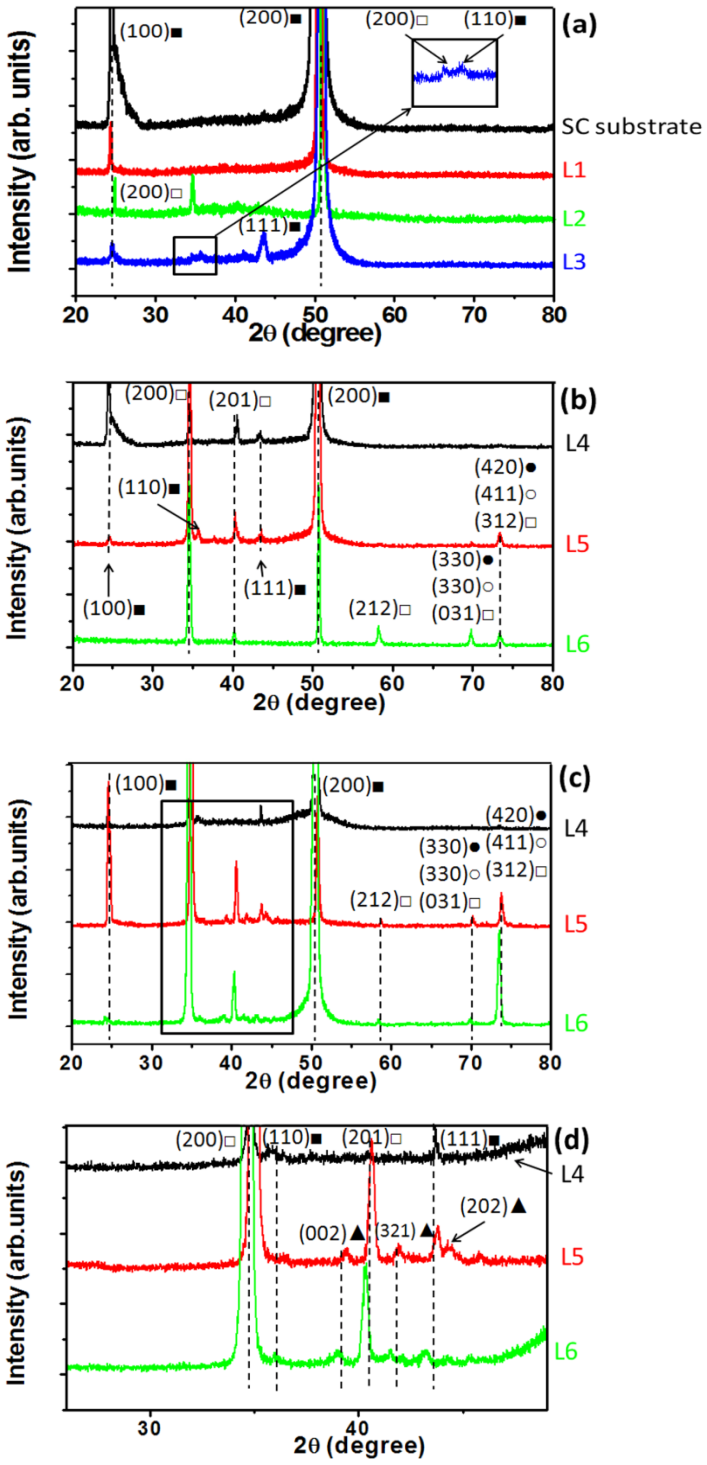

Figure 4.8: XRD $\theta/2\theta$ scan results: (a) SC substrate and films deposited at L1, L2 and L3 condition, (b) films deposited at L4, L5 and L6 condition, (c) films deposited at L7, L8 and L9 condition and (d) enlarged view of rectangular in (c) (■: Ni_3Al , □ Ni_3Ta, ●: Ni_4W, ○: Ni_4Mo, ▲: Cr_3Ni_2).

substrate. In addition, using a higher pulse energy under the same substrate temperature tended to increase the behavior of the non-epitaxy.

The mobility and thermal energy of depositing atoms mainly depend on the substrate temperature and pulse energy. The increased mobility and thermal energy of depositing atoms at relatively high substrate temperatures and pulse energies will enhance the surface and volume diffusion of adatoms more during the deposition process. This may allow many alloy elements such as Ta, W, Mo and Cr to be diffused into the γ' phase and form other phases besides the main γ'-Ni_3Al phase by replacing Al- or Ni-sites with these atoms. The site preference of replacing atoms was studied [52]. It was found that in Ni-Al-X (Ta, W, Mo or Cr) ternary alloys, Cr substitutes for both the nickel- and aluminum-sites and Ta, W, and Mo substitute primarily with the Al-site in Ni_3Al because it has a similar electronic configuration to Al. In the XRD results, considerably large peaks from Ni_3Ta are seen. According to [52], the heat of compound formation of Ni_3Ta is very similar to that of Ni_3Al compared to other compounds such as Ni_3Mo or Ni_3W. The similarity between the heats of compound formation may suggest that diffused Ta atoms in γ' phase replace Al atoms preferentially and produce more compounds with Ni atoms as compared with other alloy elements. Based on the Taguchi analysis in section 4.2.4, the effect of the substrate temperature on the crystallinity of the deposits are more significant than that of the pulse energy. This may indicate that the degree of diffusion of adatoms is more dependent on the substrate temperature once they stick to the surface.

It was proposed that the epitaxial growth of the deposits in the vapor deposition process is more likely to occur as the degree of the supersaturation decreases [63]. According to [63], at low supersaturations, only preferred sites can act as nucleation sites

to form a particular orientation for the epitaxial growth while at high supersaturations, random nucleation is more likely. In the PLD process, using the relatively low pulse energy is expected to generate a low supersaturation in the deposition area by reducing a partial vapor pressure due to a lower atom flux. In this study, the epitaxial growth only occurred when the lowest pulse energy (2 J/cm^2) was used. For the same substrate temperature, the degree of the epitaxy was reduced with increasing the pulse energy. This result may support the beneficial effect of the low supersaturation on the epitaxial growth of the deposit.

4.2.2 Analysis of microstructure

Figures 4.9 and 4.10 show the surface images of the films deposited at different conditions. As seen in figures 4.9 and 4.10, the films exhibited different surface structures depending upon the process parameters used. From the XRD results and surface images, it was considered that the similar surface structures led to the analogous XRD patterns. The film deposited at the L1 condition has a smooth surface in which uniformly distributed small particles of several tens of nano meters exist (figure 4.9 (a)). Figure 4.9 (c) and (d) show the etched surface image of the film deposited at the L1 condition. The Ni-matrix (γ phase, white area) and the cuboidal shape's γ' phase (dark area) precipitated in it (typical microstructure shown in the SC substrate) are seen in the figures. Based on the figure 4.9 (c) and (d), it is considered that the dark zones (circled by white color) shown in the figure 4.9 (a) and (c) are contributed from the γ' sites. Figures 4.9 (e) and 4.9 (f) show surface images deposited at the L2 and L3 condition, respectively. The size of particulates is larger than those seen for the L1 condition. The particle density

was noticeably greater for the L3 condition, which used the highest pulse energy under the same substrate temperature. It was seen that the deposited particles coalesced together and began to form island-like structures on the film surface.

The further extension of these islands seemed to produce the surface structure shown in the film deposited at the L4 condition (figure 4.10 (a)) using a relatively higher substrate temperature as compared to L1, L2, and L3. The islands combined with each other and formed a matrix with small cavities in it as shown in figure 4.10 (a). With the increase of the pulse energy, the islands almost covered the whole surface of the substrate, and the size of the particles in the islands increased (figure 4.10 (b)). With a further increase of the pulse energy, the flat and equiaxed particles disappeared and only granular particles (brighter spots in figure 4.10 (b)) grew further, as shown in figure 4.10 (c). With the further increase of the substrate temperature as compared to the L6, the granular type particles increased up to around 5 μm as shown in figure 4.10 (e) and 4.10 (f). These are partially linked to each and have an irregular shapes, as shown in the figures.

Etched film cross-section images are seen in figure 4.11. Figure 4.11 (a) shows a cross-section image of the film deposited at the L1 condition. Well arranged γ and γ' structure were seen from the film side to the substrate, and a clear boundary between the substrate and the film was not observed, which implies the deposited film has same microstructure as that of the SC substrate. The XRD result (figure 4.8 (a)) and the SEM image (figure 4.11 (a)) indicate that the homoepitaxial film growth occurred under the L1 condition.

Figure 4.11 (b) and (c) show the cross-section images of the films deposited under the L5 and L8 conditions. In figure 4.11 (c), blurry area on the film side is due to the inflow

of the resin which is used to fasten a sample. The microstrucutures of the irregular shape were found over the wide range of the cross section of the films. Due to the different microstructures between the film and substrate, the interfaces separating the films from the substrates clearly appeared as shown in the figures. This discontinuity in the microstructure of the interface regions shows that the films grew non-epitaxially.

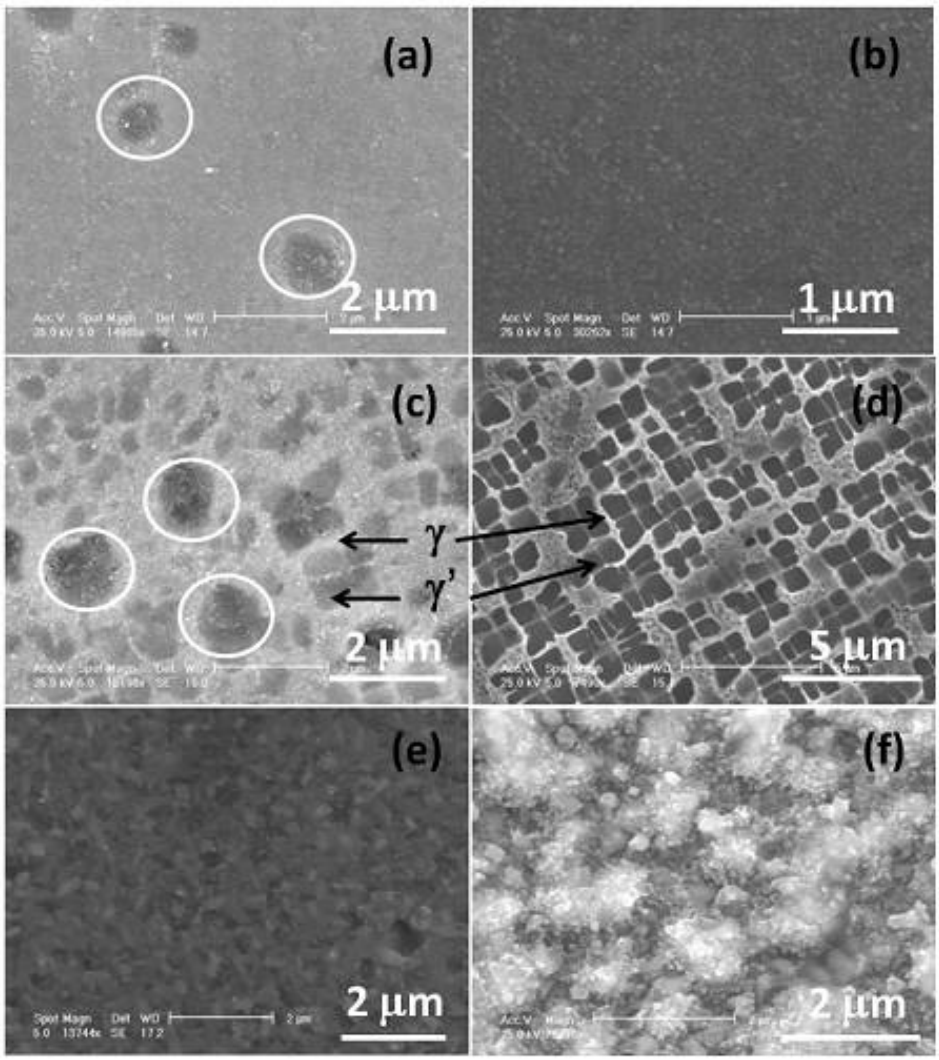

Figure 4.9: SEM film surface images: (a) & (b) L1 condition ((b) is high magnification), (c) & (d) etch treated surface (L1 condition, (c) has been etched more slightly), (e) L2 condition and (f) L3 condition.

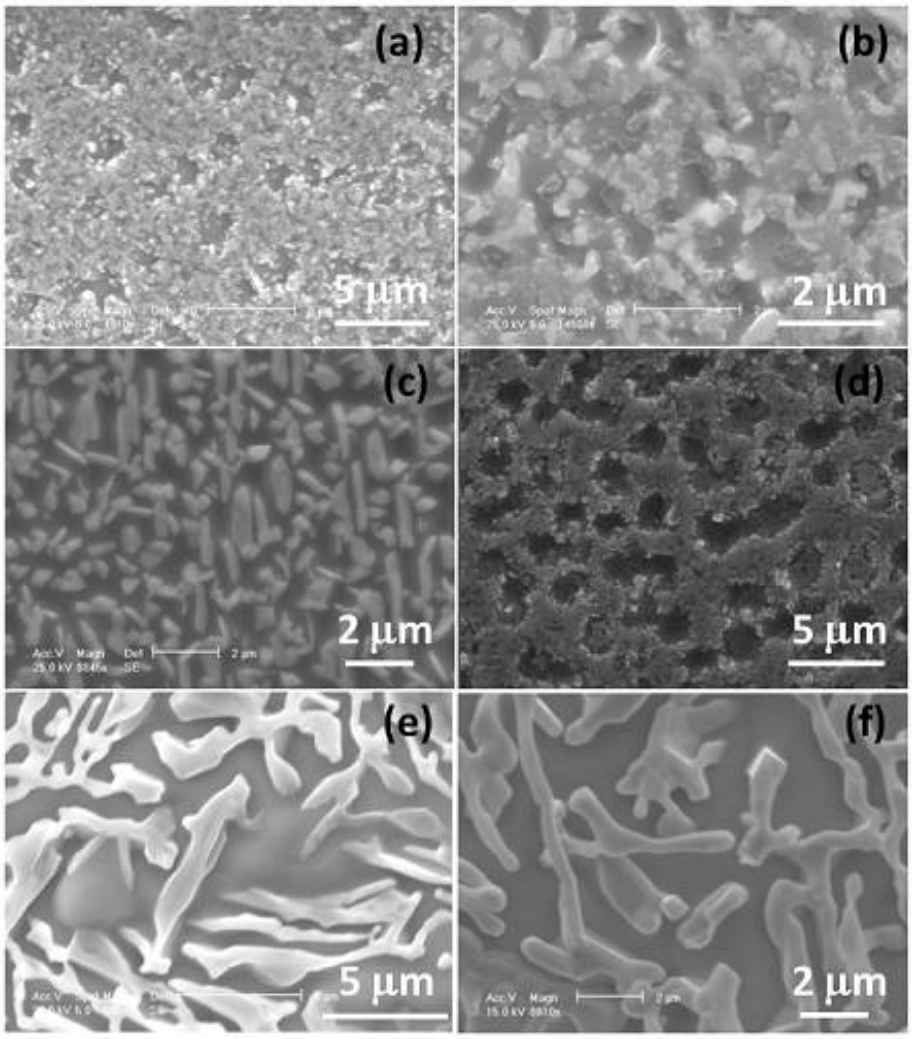

Figure 4.10: SEM film surface images: (a) L4 condition, (b) L5 condition, (c) L6 condition, (d) L7 condition, (e) L8 condition and (f) L9 condition.

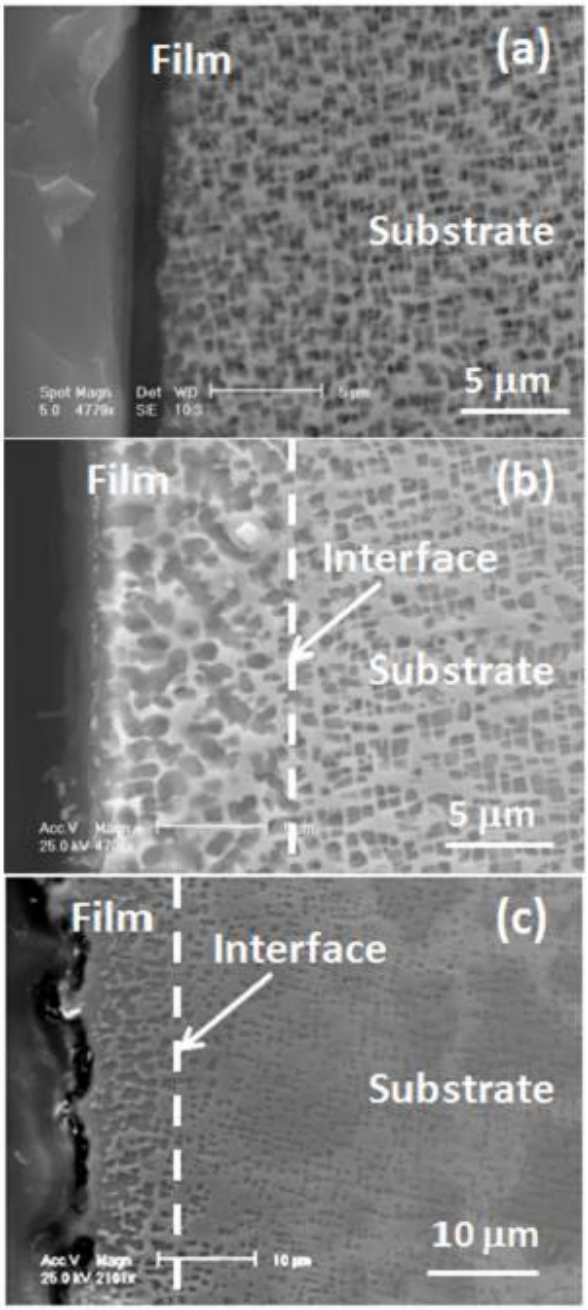

Figure 4.11: SEM film cross section images: (a) film deposited at the L1 condition, (b) film deposited at the L5 condition, and (d) film deposited at the L8 condition.

4.2.3 AFM surface morphology analysis of the SC film

Figure 4.12 shows the AFM surface morphology analysis of the SC film (produced under L1 condition). Figure 4.12 (a) and (b) show 3 and 2-dimensional film surface images, respectively. Small peaks shown in the 3-dimensional surface image are attributable to small particles which are uniformly distributed on the film surface as shown in figure 4.9 (b). The measured root mean square roughness is ~ 6 nm and the relative height difference at an arbitrary cross section is about 20-30 nm as shown in figure 4.12 (c).

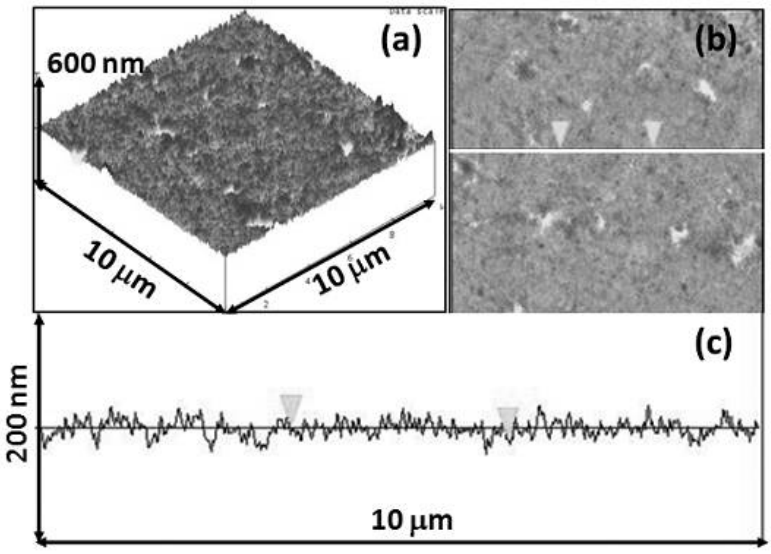

Figure 4.12: AFM image of the SC film: (a) 3-dimensional view, (b) 2-dimensional view ($10\times10\ \mu m^2$) and (c) surface profile at the section marked by a solid line in (b).

4.2.4 Effect of process variables on the process

In order to investigate the relative effect of individual variables on the process, the response of the process was defined as follows. When the deposited film shows the same

XRD peak pattern as that of the SC substrate, the response has a value "1". Additional count is added to the response whenever different film growth orientation or other phase is found in the XRD results (the higher response is, the stronger polycrystalline behavior the films have). By using this rule, the responses for all the experiments (from L1 to L9) designed by the Taguchi method were determined. Table 4.1 shows the response of all experiments.

The four graphs in figure 4.13 show the mean response at the each level of the individual process parameter. The four graphs indicate how much the response changes for a given variation (the range of the level) of an individual process parameter. As seen in the figure 4.13, the response of the process tends to vary significantly as the substrate temperature changes. It also varies more with the pulse energy as compared with the deposition time or pulse repetition rate. The deposition time has the least effect on the process. According to the results, it is clear that the variables which have significant influence on the process are the substrate temperature and pulse energy.

From Table 4.1, it is seen that the total amount of the beam energy applied (pulse energy fluence × deposition time × pulse repetition rate × focused beam spot area, 3 mm^2) has no clear relationship with the crytallinity of the deposits. For the same amount of the beam energy used (L2, L4, and L6), the deposits show different degrees of the crystallinity. This observation supports that the crystallinity of the deposits is more dependent on the substrate temperature or pulse energy fluence, which determine the mobility and the thermal energy of adatoms at the moment of deposition, than other variables such as pulse repetition rate or deposition time, which are more related to the total amount of the beam energy applied during the process.

Table 4.1: Response for each experiment.

	Temperature (℃)	Pulse energy fluence (J/cm^2)	Deposition time (min)	Pulse repetition rate (Hz)	Total amount of beam energy applied (J)	Response
L1	850	2	90	10	3,240	1
L2	850	3	120	20	12,960	2
L3	850	4	150	30	32,400	4
L4	900	2	120	30	12,960	4
L5	900	3	150	10	8,100	6
L6	900	4	90	20	12,960	6
L7	950	2	150	20	10,800	4
L8	950	3	90	30	14,580	11
L9	950	4	120	10	8,640	10

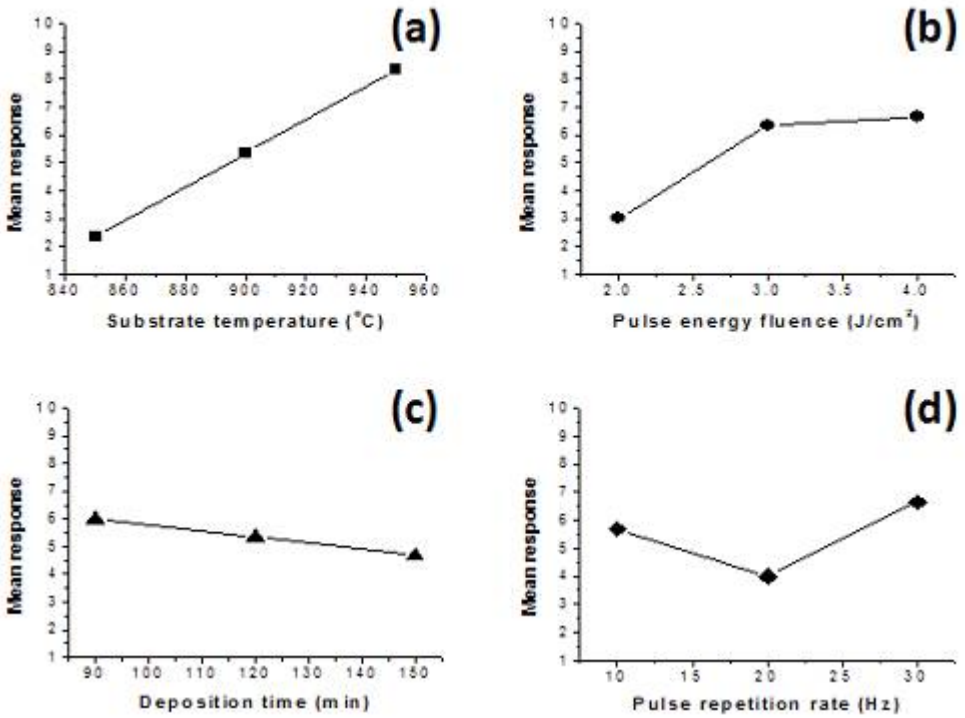

Figure 4.13: The mean response for individual process parameter: (a) mean response vs. substrate temperature (^oC), (b) mean response vs. pulse energy fluence (J/cm^2), (c) mean response vs. deposition time (min) and (d) mean response vs. pulse repetition rate (Hz).

4.3 Drilling of Inconel 718 by a diode-pumped solid state Nd:YAG laser

4.3.1 Effect of process parameters on hole quality

After sixteen experiments designed by the Taguchi method were completed, the laser-drilled holes were characterized to investigate the effect of the process parameters on the hole quality.

Once all responses (real values) of the drilling experiment had been obtained (drilling time, exit hole diameter, hole taper, and recast thickness), they were normalized to values between 1 and 10 with 10 representing the highest quality. For example, the highest hole quality index 10 was assigned to the sample with the shortest drilling time, and the drilling time of other samples were normalized based on this value. Likewise, the highest quality index 10 was assigned to the sample with the largest exit hole size, and the exit hole size of other samples were normalized based on this value; therefore, each hole had an individual hole quality index (IHQI) according to four criteria (drilling time, exit hole size, hole taper and recast thickness), each ranging from 1 to 10 (1= worst quality, 10= best quality). These IHQIs were then averaged to obtain a total hole quality index (THQI) for each hole.

The goal was to maximize IHQIs and THQI. To this end, the effects of varied process parameters on the IHQI and THQI were analyzed. In particular, signal-to-noise ratios (SNRs) for the IHQIs and THQI were analyzed in accordance with a larger-is-better approach using the following equation:

$$SNR = -10log_{10}\left[\frac{1}{n}\sum_{i=1}^{n}\frac{1}{y_i^2}\right]. \quad (4\text{-}1)$$

In this equation, 'n' represents the total number of tests in a trial (n=1 in this study), and 'y_i' represents the response (IHQI and THQI). Figure 4.14 (raw data for figure 4.14 is seen in APPENDIX B) shows the effects of process parameters on the IHQIs. The highest SNR of each parameter gives the optimum condition to get the best IHQI. The most significant findings from the experiments are summarized below.

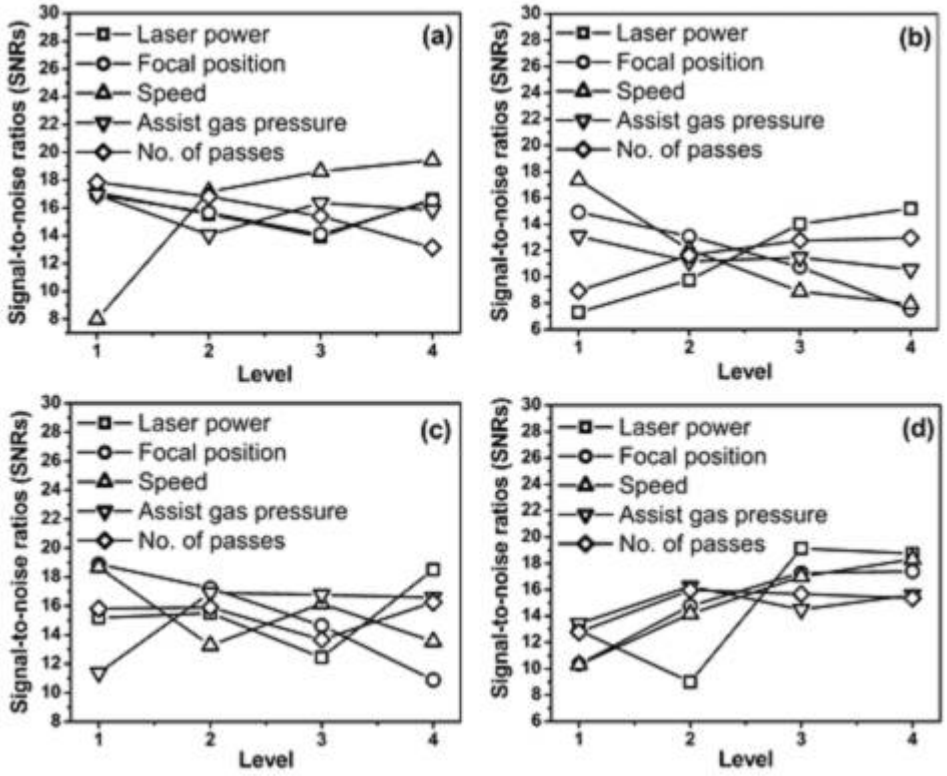

Figure 4.14: Effect of parameters on (a) drilling time, (b) exit hole diameter, (c) hole taper and (d) recast layer thickness

4.3.1.1 Drilling time

The clear tendency of the SNR is merely seen for drilling speed and number of passes since the drilling time is only affected by speed and number of passes. The results indicate that high speed and small number of passes reduce the drilling time.

4.3.1.2 Exit hole diameter

It is revealed that high laser power and low speed are the two main factors to increase the exit hole size. This is due to absorption of more laser energy by the material at high power, which results in further removal of the material. Also, a deeper penetration of the laser beam at lower beam scanning speed contributes to an increase of the eixt hole. Locating beam the focal position on the workpiece surface (i.e., focal position is 0 mm) was also of help to enlarge the exit hole. Setting the focal position on the workpiece surface yields the smallest beam spot size and the maximum energy intensity of the laser beam which is favorable to removal of the material at the initial stage of the process. In addition, the beam diameter becomes wider as the beam passes through its focal position due to the divergence of the beam. The widest beam diameter at the bottom surface of the workpiece is obtained when the beam is focused on the top surface of the workpiece (i.e., focal position is 0 mm). This expands the exit hole at the later phase of the process; thus, using a focal position = 0 mm was useful to get the larger exit holes. As the number of drilling passes increased, which was accompanied by the increase of drilling time, exit holes became wider. The results failed to show that using Ar as the assist gas was advantageous to enlarging exit holes under any of the experimental conditions included in

this study. In this study, the Ar gas just played a role as the cooling source, which reduces drilling performance by cooling down the workpiece (see section 4.3.2.2).

4.3.1.3 Hole taper

In general, the entry hole is greater than the exit hole in laser drilling for two reasons. First, the entry part of a hole tends to be exposed to the laser beam to a greater degree than the exit hole. Second, the erosion of the entry side by the molten materials occurs due to recoil pressure. This is responsible for the presence of the hole taper in laser-drilled holes. As illustrated in figure 4.14 (b), exit holes increase in size under low speed and high laser power, which, in turn, results in the decrease of the hole taper. Entry holes become smaller in size as the beam focal position gets closer to the surface of the workpiece due to the smaller beam spot size on the surface. (Intuitively, the largest entry hole will be obtained when the focal position is -3 mm and the smallest entry hole size is obtained when the focal position is 0 mm); thus, as the focal position gets closer to the workpiece surface, the hole taper will become smaller because of both the decreased entry hole size and the increased exit hole size. It was observed that using the Ar assist gas lessened hole taper. Of importance, this was not as a result of the increase of the exit hole size (see figure 4.14 (b)). Instead, it was primarily due to the decrease of the entry hole size. It could be suggested that using the Ar as an assist gas didn't contribute to hole expansion and it served more as a source to cool down the workpiece.

4.3.1.4 Recast layer thickness

A recast layer is formed within a hole if molten material is not blown away by explosion, and by the assist gas, or by re-deposited materials that form as the liquid metal between laser pulses.

As shown in figure 4.15, the recast layer thickness varies in depth. For all samples, the recast layer at the entrance side is generally the thickest, and it becomes thinner as the hole gets closer to the exit side. The entry area is generally more exposed to laser beam during the process (more chance to melt the hole wall at the entrance side) and re-deposition of removed materials starts from the entry area (accumulation of re-deposited materials at the entry area is larger than that at other locations). These are why the recast layer decreases with increasing hole depth.

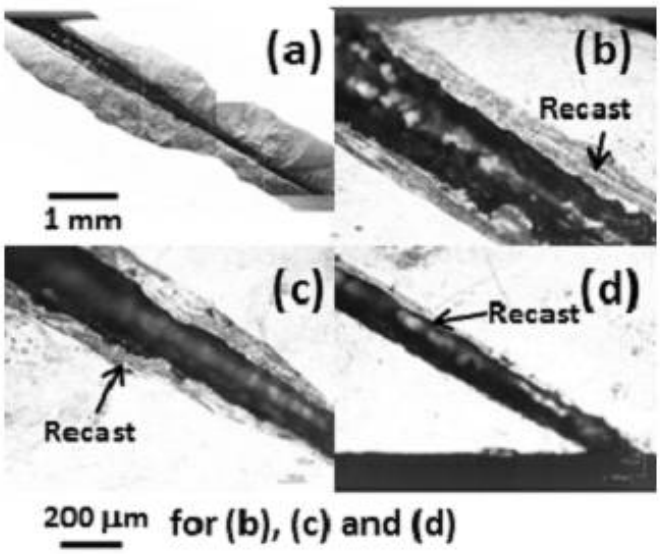

Figure 4.15: (a) Entire hole cross section (generated from experiment no. 13 in Table 3.5) and recast at the (b) entry side, (c) middle, and (d) exit side of the hole.

Figure 4.16 shows high magnification images of the recast layer. The recast layer is typically composed of several thin layers as shown in this figure. The thickness of each layer is approximately 5-10 μm. These thin layers are attributed to a byproduct of the re-melting and re-solidification of the hole wall and re-deposited layers due to a repetitive interaction of the laser beam with the walls of the hole.

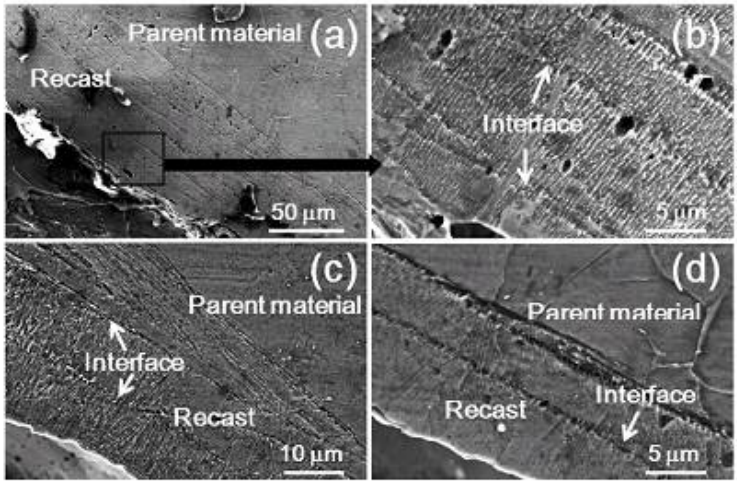

Figure 4.16: (a) High magnification SEM image of the recast (generated from experiment no. 13 in Table 3.5) and recast at the (b) entry side, (c) middle, and (d) exit side of the hole.

The observed recast layers are primarily composed of fine columnar dendrites, which differ from the equiaxed grain structures shown in the parent material. As seen in the figures, the growth direction of the columnar dendrites is nearly perpendicular to the hole wall. This indicated that cooling mostly occurred via the hole wall during the solidification process. Elemental composition of the recast was almost identical to the parent material compositions. This occurred because the inert Ar assist gas suppressed oxidation. Table 4.2 shows elemental composition data of the recast and parent material.

Table 4.2: Elemental composition data of the parent material and recast.

	Composition (wt %)								
	Ni	Cr	Fe	Ti	Mo	Nb	Ta	Al	O
Parent material	52.60	18.29	18.99	1.04	3.27	4.66	0.27	0.67	0.21
Recast	51.72	18.33	18.32	1.21	3.26	5.58	0.60	0.73	0.26

Figure 4.14 (d) shows that high laser power above 65 W is favorable to reduce the recast layer. In the nanosecond laser drilling process, both expulsion of the melt and vaporization are generally two important material removal mechanisms. In this experiment, increased laser power enhanced the contributions of vaporization to the material removal mechanism, and therefore reduced the recast layer by diminishing molten material formation. The low speed was shown to increase the recast layer in this study. At low speed, a laser beam could go down further in the workpiece. Under this condition, the hole of a relatively large hole depth to width ratio (deep and narrow hole) is likely to be formed. This geometrical characteristic of the hole could restrict the ejection of molten debris from the hole and enable re-deposit on the hole wall during the process. The assist gas also seemed to reduce the recast layer; however, its influence was not substantial under the range of gas pressures tested in this study.

4.3.1.5 Effect of process parameters on THQI

The THQI was calculated using the IHQIs, and the optimum set of process parameters to improve hole quality was obtained. The effects of process parameters on the THQI are summarized in Table 4.3. It was found that the laser power had the most significant influence on the THQI, and the focal position had the second greatest influence factor.

The effects of the other three variables were small (see Rank in Table 4.3). The optimum set of parameters, that is, the set of parameters with the highest SNR, and its impact on the total hole quality are presented in Table 4.4.

Table 4.3: Signal-to-noise ratios (SNRs) for THQI and rank of effects.

Level	Laser power	Focal position	Speed	Ar assist gas pressure	No. of passes
1	14.85	16.29	15.39	15.23	15.32
2	14.29	16.12	15.44	16.00	15.75
3	16.46	15.63	16.15	15.86	15.89
4	17.55	15.10	16.16	16.05	16.17
Delta[a]	3.25	1.19	0.77	0.82	0.85
Rank	1	2	5	4	3

[a] Difference between the highest and lowest signal-to noise ratio.
- Rank is determined based on Delta.

Table 4.4: Optimum drilling parameters and their main effect on the improvement of the THQI.

Parameter	Optimum level	Main effects on the improvement of the THQI
Laser power	4 (70 W)	Increase of exit hole size and decrease of hole taper and recast layer thickness
Focal position	1 (0 mm)	Increase of exit hole size and decrease of hole taper
Speed	4 (8 mm/s)	Decrease of drilling time and recast layer thickness
Ar assist gas pressure	4 (100 KPa)	Decrease of recast layer thickness and hole taper
No. of passes	4 (54)	Increase of exit hole size

- The main effects on the improvement of the hole quality are described from section 4.3.1.1 to section 4.3.1.4.

4.3.2 Investigation of drilling performance

For the real application of laser drilling, economical efficiency of the process is important. In other words, producing holes in the shortest time is desirable in real

applications. Enhancing the drilling performance is therefore indispensible. In the following sections, the results of the subsequent experiments to examine drilling performance are presented. Drilling performance was compared based on exit hole diameter and drilling time. In particular, better performance was defined as producing the largest exit in a shorter time.

4.3.2.1 Comparison of three drilling modes

A series of drilling experiments using three drilling modes, helical, percussion, and trepan drilling, were carried out. A 7.5 % duty cycle laser setting was used for the trials. In the case of the helical drilling, the process conditions which produced the greatest performance in the previous experiments (section 4.3.1) were adopted. These were as follows: 70 W laser power, 0 mm focal position, and 8 mm/s travel speed. Using these conditions, several experiments were performed. Figure 4.17 shows the results of the experiments. The exit hole size increased with increasing the No. of drilling passes. Under the 30 drilling passes taking the smallest drilling time (~4.97 s), the largest exit was generated when Ar gas was not used. This was because the Ar gas only played a role as a cooling source. The entry hole obtained in this condition was ~ 0.653 mm. As mentioned earlier, this revealed again that using Ar as the assist gas was not useful to enlarge exit holes. The large increase of the exit hole in the case of fifty four drilling passes is probably due to the effect of heat accumulated during the relatively long drilling process.

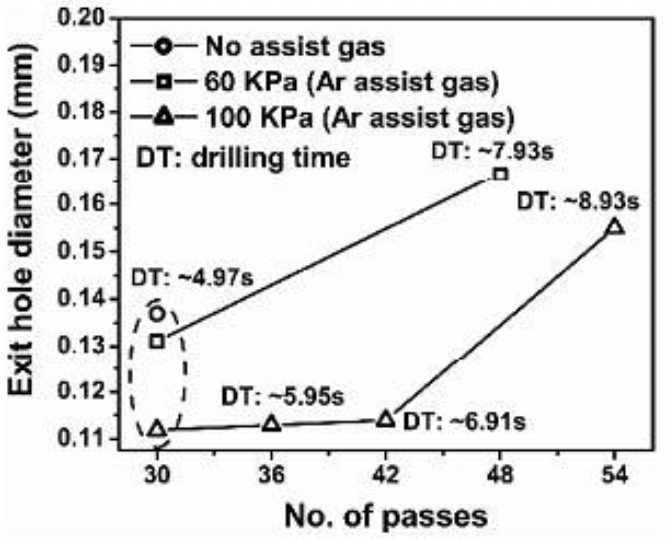

Figure 4.17: Results of the helical drilling experiment (laser power: 70 W, focal position: 0 mm, speed: 8 mm/s).

Figure 4.18 shows the results of the percussion laser drilling experiments. The percussion laser drilling experiments were performed at 70 W laser power, several different focal positions, and two different drilling durations (~5 and 10 s). Experiments with and without the Ar assist gas were evaluated and the results were compared to one another. The Ar assist gas was not generally beneficial in enhancing the drilling performance as in the case of the helical drilling due to the cooling of the workpiece by convection as explained previously. The exit hole generally increased with locating the focal position closer to the workpiece surface. In this case, the high intensity beam was applied to the workpiece at the initial stage of the process, which enhanced drilling performance. The beam diameter becomes wider at the bottom surface of the workpiece as the focal position is set closer to the top surface of the workpiece. This may explain why the exit hole is larger. For 100 KPa Ar assist gas and 10 s drilling time, variation in the exit hole size is small. The relatively long drilling time (10 s) produces much larger

exit hole than 5 s drilling time at -3 mm beam focal position; however, the exit hole slightly increases as the focal position is set closer to the top surface of the workpiece. The convection cooling by the Ar gas may suppress expansion of the exit hole.

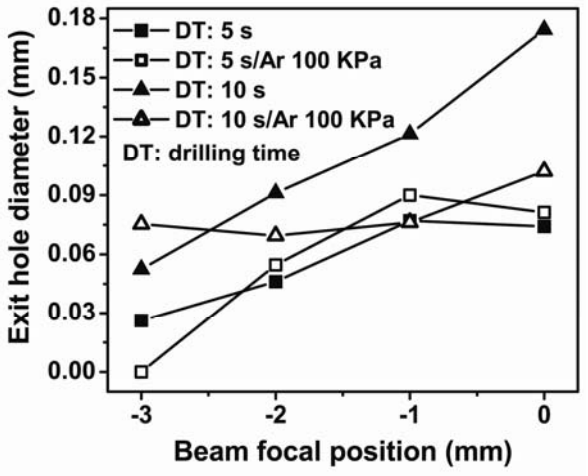

Figure 4.18: Results of the percussion drilling experiment (laser power: 70 W).

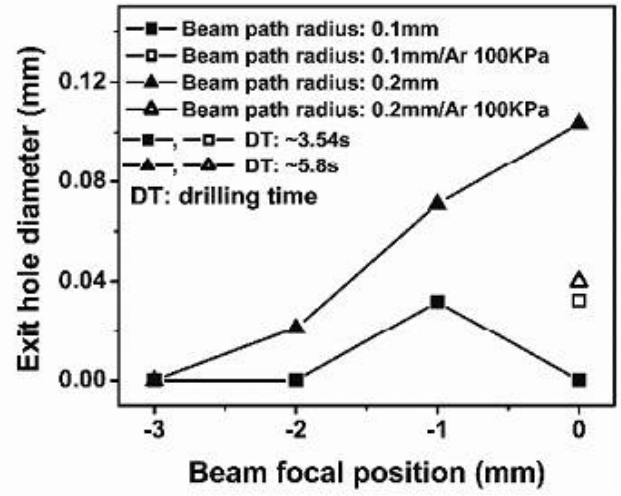

Figure 4.19: Results of the trepan drilling experiment (laser power: 70 W, speed: 8 mm/s, no. of passes: 30).

In most cases, entry holes in the percussion drilling were smaller in size than those produced by the helical drilling method because the beam was positioned at one point without moving around during the process, and multiple passes were not applied during percussion drilling. Entry holes increased with locating the focal position deeper from the workpiece surface, and yet, this also produced smaller exit holes.

Finally, the performance of the laser trepanning was also investigated. The experiments were conducted at 70 W laser power, 8mm/s speed, two beam trajectory radii, 0.1 and 0.2 mm, and several different beam focal positions. In particular, the Ar assist gas was used for the case of 0 mm beam focal position which is expected to give the largest exit hole from the results of percussion drilling experiments. Thirty passes were used for all the experiments. Entry hole sizes varied in the range of 0.456-0.901 mm for the experimental conditions used herein. Consistent with expectations, as the beam path became wider and the focal position got deeper, entry holes became larger. The results for the exit hole diameter are displayed in figure 4.19. The largest exit hole (~0.1 mm diameter) was obtained at 70 W laser power, 0.2 mm beam path radius, 0 mm focal position, 8 mm/s speed and 30 passes (drilling time: ~5.8 s). The entry hole diameter obtained under this condition was ~0.643 mm. For the beam path radius of 0.1 mm (black square), it is considered that -1 mm focal position produces the largest exit hole by providing an appropriate combination for beam intensity and beam diameter at the bottom surface.

From this series of experiments, it was found that the helical drilling produced the best performance (produced the larger exit hole with less drilling time) under the experimental conditions included in this study. It is considered that various beam trajectory radii with a

gradual increase in the case of the helical drilling contributes to effective material removal by providing the relatively wider scan area of the laser beam compared to other techniques.

4.3.2.2 Effect of O2 gas

The effect of the O_2 assist gas on drilling performance was also investigated. Experiments with the Ar assist gas were also conducted for comparison. The helical drilling technique and a 7.5 % duty cycle laser setting were used in these experiments, and each experiment was repeated 2 times. Drilling time for all experiments was ~4.97 s due to fixed speed (8 mm/s) and no of passes (30). The average and standard deviation error are shown in figure 4.20.

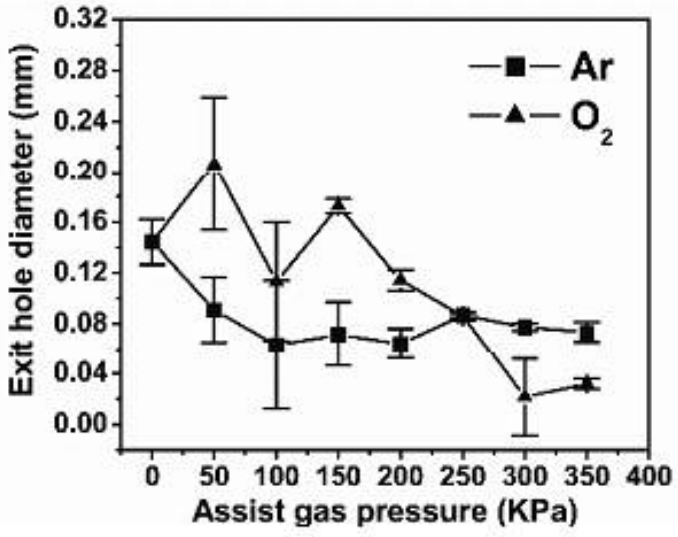

Figure 4.20: Effect of the assist gas on the exit hole diameter (laser power: 70W, focal position: 0 mm, speed: 8 mm/s, no. of passes: 30).

As shown in the figure 4.20, using the Ar assist gas was not at all useful for enlargement of the exit hole as before. However, using O_2 as the assist gas was a great help to enhancing drilling performance at gas pressure of 50 KPa. The largest exit hole, ~0.24 mm, was obtained at 70 W, 0 mm focal position, 50 KPa O_2 assist gas pressure, 8 mm/s speed and 30 passes.

Using O_2 as the assist gas promotes the oxidation at the exposed area. This oxidation process delivers more energy to the workpiece by exothermic reaction, which leads to better drilling efficiency. The enhancement of drilling performance by using O_2 assist gas was also reported in reference [75]. In this experiment, 50 KPa O_2 pressure produced the best drilling performance; however, increase of the O_2 pressure more than 50 KPa resulted in the loss of the drilling efficiency. This may be due to the rapid convective cooling of the workpiece by forced convection from the fast gas flow. The wt% of O_2 in the recast layer was measured by an energy dispersive spectrometer (EDS). The average and standard deviation error of the measurements are shown in the figure 4.21. There was a significant increase of wt% in the recast layer when O_2 was used as the assist gas. Due to the effect of the oxygen in the air, more oxygen was detected in the recast in the case of no gas when compared to the Ar assist gas. Among three main elements (Ni, Cr and Fe) of the Inconel 718, the amount of Ni in the recast layer was significantly reduced as compared to the amount of Ni in parent material for O_2 assist gas. However, the relatively small reduction of Fe and the minimal increase of Cr were observed in the recast regions as shown in the inset of the figure 4.21. This implied that the Cr was preferentially oxidized compared to other elements. Once the chromium oxide is formed, it tends to prevent the inflow of more oxygen into a material; therefore, the recast layer produced

with the oxygen assist gas could be an effective shield against oxidation. The wt% of O_2 did not vary much under the range of O_2 pressure tested in this study, which, in turn, indicated that the recast was fully oxidized at 50 KPa O_2 pressure already. This indicated that extra O_2 gas beyond that had no contribution to the oxidation process and it caused rapid convective cooling of the workpiece, which lowered drilling performance.

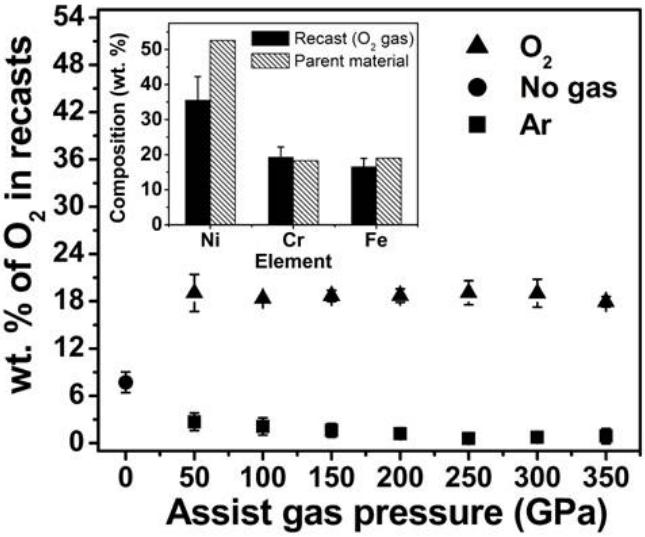

Figure 4.21: wt% of the O_2 in recasts (laser power: 70 W, focal position: 0 mm, speed: 8 mm/s, no. of passes: 30). Inset: composition of three main elements of Inconel 718 in the recast (for O_2 assist gas).

4.3.2.3 Comparison of two laser settings

The drilling performance at two different laser duty cycles was investigated. For this experiment, a 7.5 % (500 Hz pulse repetition rate, 150 μs pulse duration) and 10 % (500 Hz pulse repetition rate, 200 μs pulse duration) duty cycle settings were used by adjusting the duration of the pulse (The duty cycle is defined by the ratio of the pulse

duration to the pulse period). The drilling performance was compared for four different experimental conditions as shown in figure 4.22. Also, the helical drilling method was used in this experiment. In particular, the effect of the moving focal position on the exit hole size was also considered. In this case, the focal position was moved up to 3 mm into the part during the process. The main goal of this method is to maintain high laser beam intensity at the interaction region of the laser-workpiece. Each experiment was repeated 2 times, and average value and standard deviation error are shown in the figure 4.22. Drilling time for all experiments was ~4.87 s due to the fixed speed (8 mm/s) and the number of passes (30).

In general, the drilling performance for all cases was enhanced using a 10 % duty cycle laser setting, as shown in the figure 4.22. In the case of a 7.5 % duty cycle laser setting, the drilling performance was enhanced using the moving focal position method as shown in figure 4.22 (a). As explained above, this is attributable to keeping high laser beam intensity at the interaction region of the laser-workpiece. Using both O_2 gas (50 KPa) and moving the focal position gave the best performance throughout the four different experiments. Moving the focal position method was not useful to improve drilling performance in the case of a 10 % duty cycle laser setting. Under the 10 % duty cycle, laser power itself may be high enough. As a result, a rate of increase of the drilling depth would be higher than a rate of variation of the focal position. This may relatively decrease the beam intensity more at the interaction region of the laser-workpiece compared to 7.5 % duty cycle. Figure 4.23 shows the cross section of the hole produced at a 10 % duty cycle laser setting (90 W laser power, 0 mm focal position, 50 KPa O_2 assist gas pressure, 8 mm/s speed, 30 passes, ~0.7 mm entry hole diameter, ~60 μm

recast thickness). High magnification SEM images show that the recast is composed of two types of layers. The inner part is a non-oxide layer which has the similar microstructure and elemental composition to those shown in figure 4.16 and Table 4.2. The outer part of the recast region is an oxide layer with an increased Cr content relative to the other main elements (Ni and Fe). Elemental composition data of the oxide layer are shown in Table 4.5.

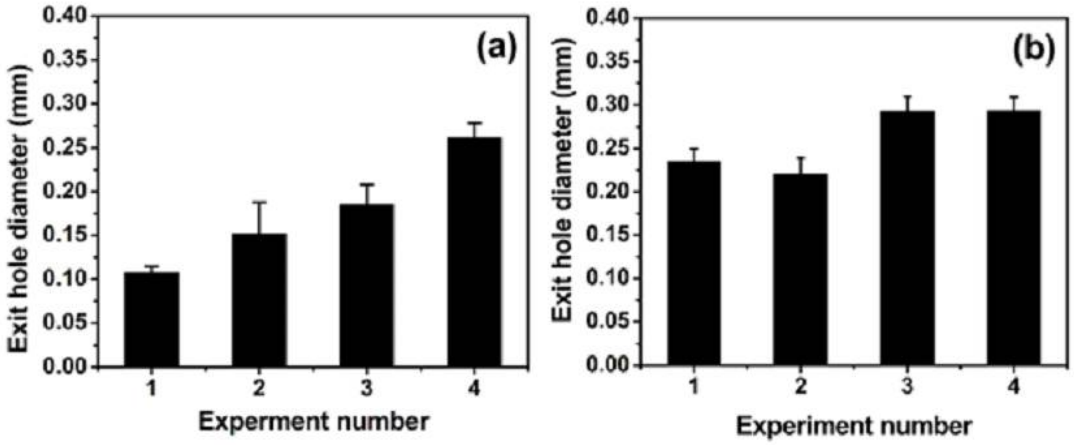

Figure 4.22: Investigation of the drilling performance: (a) 7.5 % duty cycle (70 W, 8 mm/s, 30 passes) and (b) 10 % duty cycle (90 W, 8 mm/s, 30 passes) (experiment 1: fixed focal position, 0 mm, and no assist gas, experiment 2: moving focal position and no assist gas, experiment 3: fixed focal position, 0 mm, and O_2 50 KPa, experiment 4: moving focal position and 50 KPa).

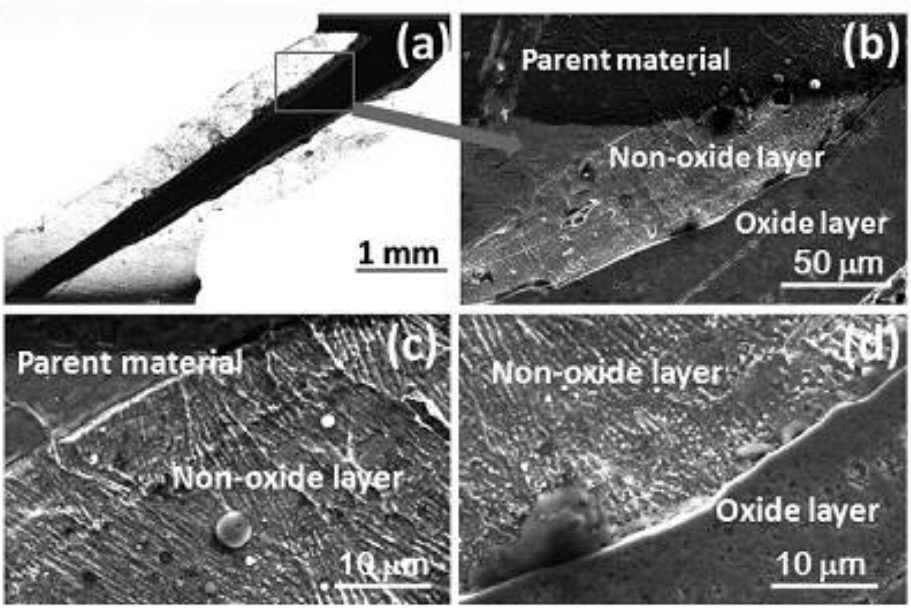

Figure 4.23: (a) Entire cross section of the hole produced at a 10 % duty cycle laser setting (90 W laser power, 0 mm focal position, 50 KPa O_2 assist gas pressure, 8 mm/s speed and 30 passes, ~4.97 s drilling time), (b) recast at entry side, (c) interface between parent material and non-oxide layer and (d) interface between non-oxide layer and oxide layer.

Table 4.5: Elemental composition data of the non-oxide and oxide layer.

	Composition (wt. %)								
	Ni	Cr	Fe	Ti	Mo	Nb	Ta	Al	O
Non-oxide layer	50.93	17.75	18.73	1.82	3.53	4.89	0.42	1.18	0.74
Oxide layer	23.41	22.94	16.24	1.38	3.14	9.05	1.30	0.97	21.56

4.4 Plasma diagnostics in laser drilling and DMD process

4.4.1 Plasma diagnostics in laser drilling process

Figure 4.24 shows the emission spectrum of the laser-induced Inconel 718 plasma obtained during the drilling process. The spectrum in the range of 526-540 nm is seen in the figure. Emission lines were identified by atomic line data base of the National Institute of Standards and Technology (NIST) [108]. Most of the lines in figure 4.24 are neutral CrI lines. In particular, the above spectral range was chosen so as to leverage parameters from [109] in order to determine electron number density. Two atomic CrI lines were selected to measure the line intensity and determine both the electron temperature and electron number density of the Inconel 718 plasma. Table 4.6 shows the spectral data of the lines selected.

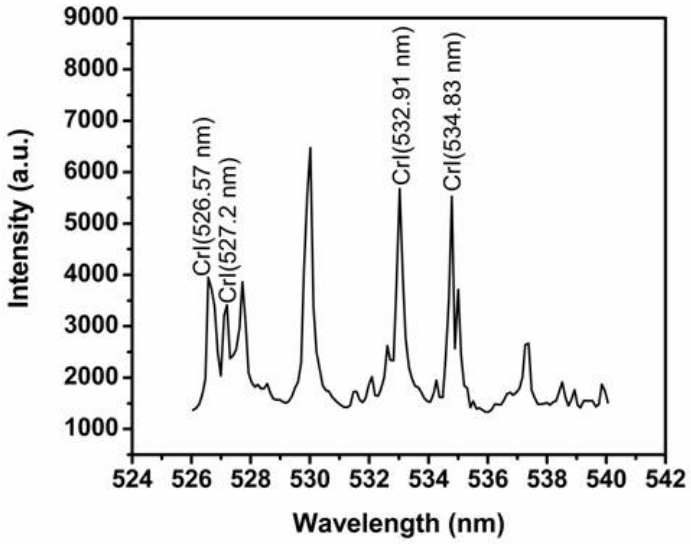

Figure 4.24: Emission spectrum of Inconel 718 for between 526-540 nm.

Table 4.6: Upper level data on for atomic CrI lines.

Wavelength (nm)	Energy (eV)	g (degeneracy)	A (transition probability, 10^6/s)
532.91	5.239	9	22.5
534.83	3.321	7	1.7

The intensity of a given spectral line I_{mn}, which is induced by transition from upper level m to lower level n, can be described as

$$I_{mn} = N_m A_{mn} h\upsilon_{mn,} \tag{4-2}$$

where N_m is the population density of the state m, A_{mn} is the transition probability, h is Planck's constant, and υ_{mn} is the frequency of the spectral line that results upon transition from level m to level n. A_{mn}, h, and υ_{mn} are constants for a given transition. The above relation indicates that the intensity of a given spectral line is proportional to the population density, that is, the number of atoms associated with the given transition in the plasma; thus, the line intensity is related to the amount of material in plasma.

The temporal behavior of the line intensity and drilling depth for different laser scanning speeds and powers are shown in figures 4.25 and 4.26. The line intensity measured is generally very high at the very early stage of the drilling process; however, it drops significantly after the second or third measurement (after ~ 0.04-0.06 s). This can be ascribed to several factors. First, the focused high power density beam initially removes a large amount of material (a rate of the increase of the drilling depth is very high at the early stage as shown in the figures 4.25 (b) and 4.26 (b)); however, the rate of material removal quickly decreases due to the decrease of the laser beam intensity by

beam defocusing as the drilling depth increase. Second, material removal could be reduced as well due to the further beam energy loss by the plasma inside the cavity that produced as the drilling depth increases. Finally, the plasma core, which has a high particle density, continuously moves down as the drilling depth increases during the process. This also causes the reduction of the intensity.

The line intensity becomes small with decreasing the speed as shown in figure 4.25 (a). At lower speed, the laser beam can go deeper into the workpiece. Due to this, the plasma core stays in a position much lower than the measurement location; therefore, the intensity is smaller at lower speeds. As figures 4.26 (a) and (b) display, laser power is positively correlated with intensity because more material is removed when the laser power is increased.

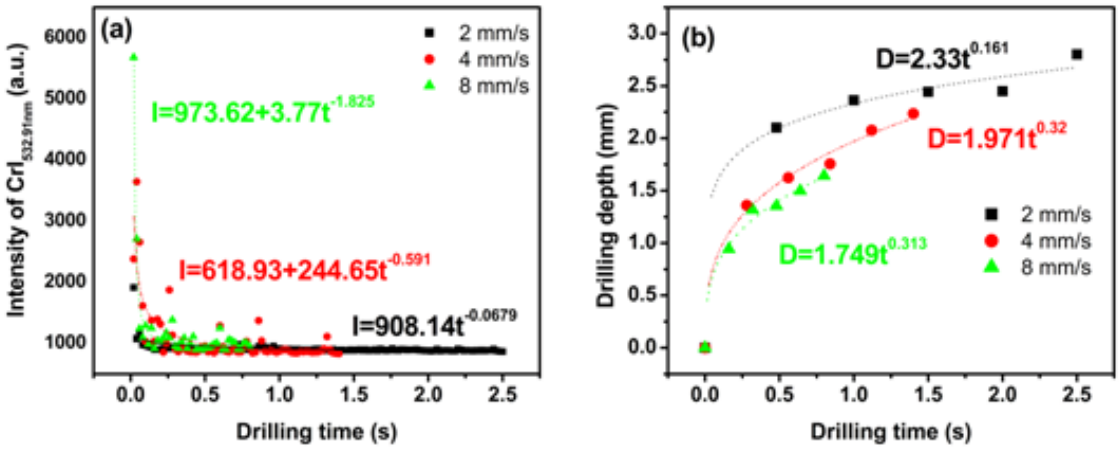

Figure 4.25: Temporal history of (a) the line intensity and (b) the drilling depth at different speeds (under constant laser power of 50 W).

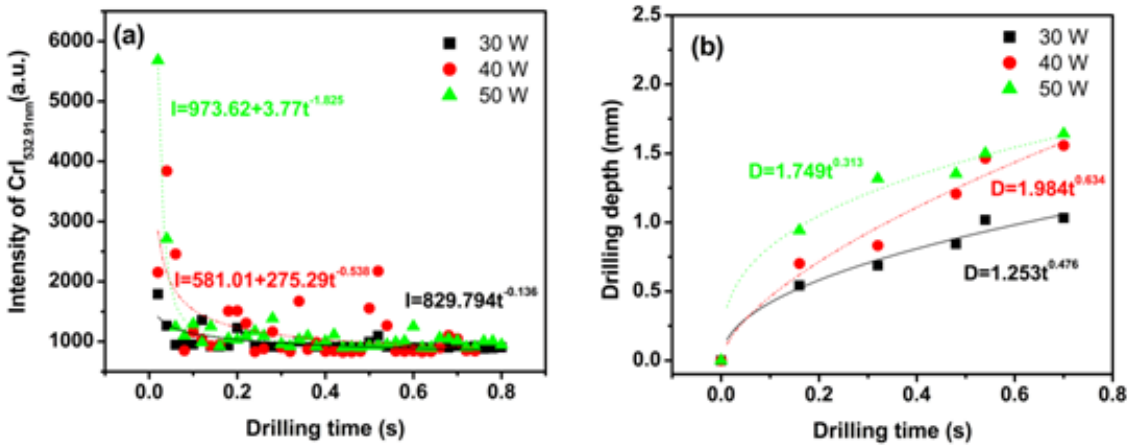

Figure 4.26: Temporal history of (a) the line intensity and (b) the drilling depth at different laser powers (under constant speed of 8 mm/s).

Line intensity histories were analyzed in combination with the drilling depth measured. Figure 4.27 presents the correlation between the line intensity and the drilling depth. At 2 mm/s speed, the line intensity decreases linearly with increasing of the drilling depth as shown in figure 4.27 (a). However, as the slopes of the curve fit lines for relatively higher speed (4 and 8 mm/s) indicates, there are two regions showing different patterns of decrease in line intensity as a function of the drilling depth. Sharp slope shown in the first region is due to significant decrease in line intensity at the early stage of the drilling process. The results for varying power are shown in figure 4.27 (b). The slopes of the curve fit lines at the early stage are steeper at relatively higher than lower power (i.e., 40 and 50 W). The same as before, this is because line intensity decreases more at the early stage of drilling. The slope at the early stage clearly tends to become steeper as laser power increases. As expected from figure 4.26 (a), this is related to the fact that in the early stage of drilling, higher material removal rate is achieved at higher laser power.

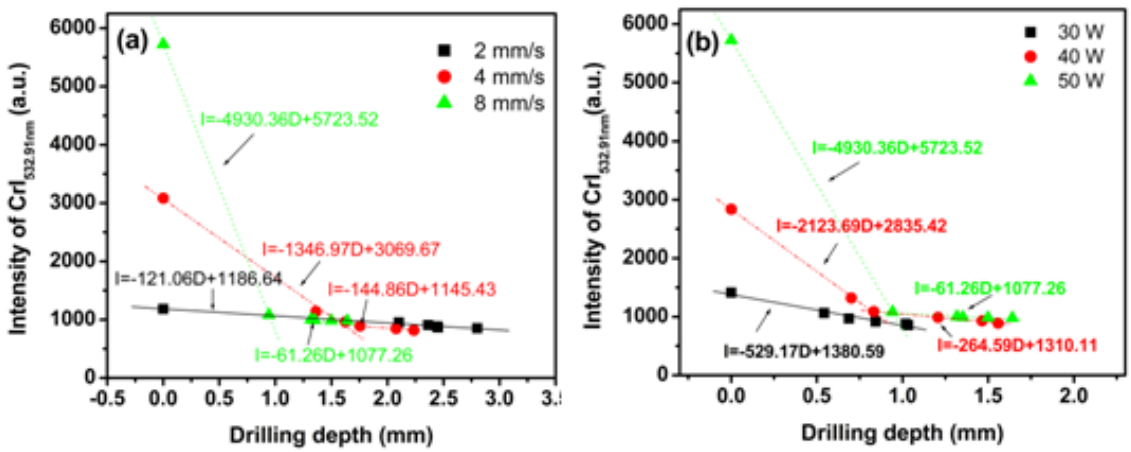

Figure 4.27: Correlation between line intensity and drilling depth (a) for different speeds and (b) for different laser powers.

In describing the plasma in this study, it is assumed that that the plasma is in local thermodynamic equilibrium (LTE) state. In the LTE condition, the population of free electrons has a Maxwell-Boltzmann velocity distribution, and excitation and de-excitation are more probable by collision process than by radiative process.

Under the assumptions above, the temperature of the plasma can be estimated using a ratio of the relative intensity of spectral lines of the same species as given by [110].

$$\frac{I_1}{I_2} = \frac{g_1 A_1 \lambda_2}{g_2 A_2 \lambda_1} \exp\left[-\left(\frac{E_1 - E_2}{kT_e}\right)\right]. \tag{4-3}$$

In this equation, T_e, I, A, g, E, λ, and k represent the electron temperature in (K), the line intensity, the transition probability in (s^{-1}), the statistical weight, the energy of the excited state (eV), the wavelength (nm), and Boltzmann's constant in (eVK^{-1}),

respectively. The temperature calculated must satisfy the LTE condition. The condition where plasma is in the LTE state can be fulfilled by the following criterion [28].

$$N_e \geq 1.6 \times 10^{12} T_e^{1/2} \Delta E^3, \quad (4\text{-}4)$$

where N_e is the lower limit of electron number density (cm^{-3}), T_e is the electron temperature (K) and ΔE is the energy gap (eV). In this study, the lower limit of the electron number density for the highest temperature (~9200 K) obtained is ~1.08×10^{15} cm^{-3}. This is smaller than values of the electron number density determined (~5×10^{15}-~8×10^{15} cm^{-3}) in this study, which thus meets the LTE condition here.

Figure 4.28 shows how the electron temperature of the plasma is associated with drilling depth. The temperature shown in the figure is the average temperature obtained during each drilling pass, and it is expressed as a function of the hole depth drilled during each drilling pass. As displayed in the figure, the temperature tends to decrease as the drilling depth increases. This is mainly due to the fact that plasma core, which is the hottest part in the plasma plume, continuously moves down as the drilling depth increases. In other words, the location of plasma sampled moves from the core to the outer part, which is relatively colder as the drilling depth increases.

Similar to the line intensity, the temperature generally showed a sharp decrease at the early stage of the process. After that, minimal variation in the temperature is seen. The standard deviation during the initiation of the drilling process is very high since the temperature varies greatly during the first drilling pass. As shown in the figures 4.25 (b) and 4.26 (b), the drilling depth increases at a higher rate during the first drilling pass.

This significantly changes the plasma sampling location. As a result, the temperature would vary greatly during the first drilling pass.

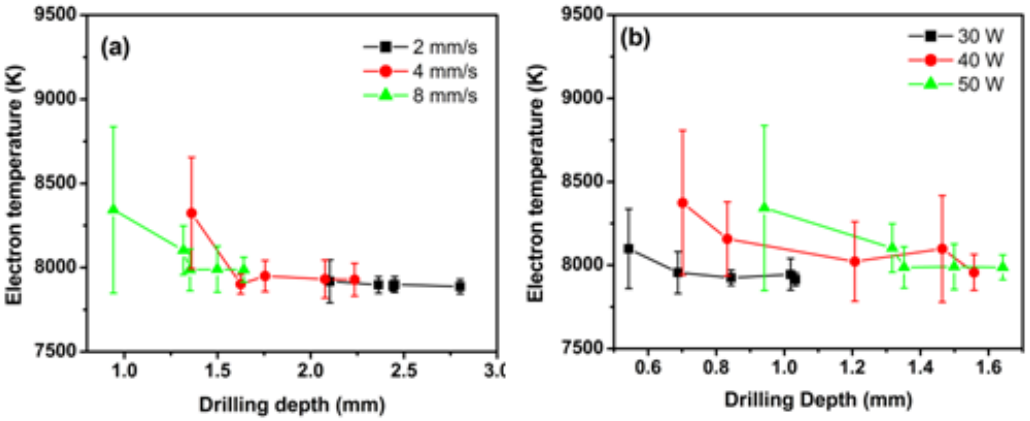

Figure 4.28: Electron temperature as a function of drilling depth (a) for different speeds and (b) for different laser powers.

Under the same power (50 W), the highest temperature is obtained at the highest speed (8 mm/s). This is because the laser beam ablates material nearer the plasma sampling location at higher speed. In figure 4.28 (b), the average temperature corresponding to the first datum in the case of the 40 and 50 W is the almost same. In general, plasma temperature is expected to be higher when higher laser power is used; however, for the 50 W laser power, plasma sampling location is further away from a plasma core because of the deeper drilling depth compared to the 40 W laser power as shown in the figure. This would level off the temperature.

The maximum temperatures (obtained at the very early stage of the drilling process, see APPENDIX C) at different laser powers are ~8500, ~9000 and ~9200 K for 30, 40

and 50 W, respectively. The maximum temperature increases with the laser power because material is removed per pulse at larger laser energies.

Not only the electron temperature, but also the electron number density, is an important parameter used to describe the plasma state and validate the LTE condition. In general, the electron number density of a plasma can be obtained by measuring the width of the Stark-broadened spectral line. The source of the Stark broadening results from the collision between radiating atoms and charged particles. The shape of the Stark-broadened emission lines takes the form of the Lorentzian function as follows:

$$y = y_o + \frac{2a}{\pi}\frac{\Delta\lambda_{1/2}}{4(x - x_c) + \Delta\lambda_{1/2}^2}, \tag{4-5}$$

where $\Delta\lambda_{1/2}$ is the full width at half maximum (FWHM), x_c is the center wavelength, a is the integrated area of the emission line, and y_o is the background emission. These parameters can be obtained from fitting the Stark-broadened emission lines.

The FWHM of the Stark broadened line ($\Delta\lambda_{1/2}$) is related to the electron number density by the following equation [79].

$$\Delta\lambda_{1/2} = 2W\left(\frac{N_e}{10^{16}}\right)\left[1 + 1.75A\left(\frac{N_e}{10^{16}}\right)^{1/4} \times \left(1 - \frac{3}{4}N_D^{-1/3}\right)\right], \tag{4-6}$$

where N_e is the electron number density, W is the electron impact-width parameter and A is the ion-broadening parameter. Both are expressed as a function of temperature. N_D is the number of particles in the Debye sphere.

The contribution from ion broadening, given by the second term in Eq. 4-6, is typically very small, accounting from less than 5% of the total variation [79]; therefore, it was not considered in this study. Accordingly, Eq. 4-6 can be simplified to the following equation:

$$\Delta\lambda_{1/2} = 2W\left(\frac{N_e}{10^{16}}\right) \quad (4\text{-}7)$$

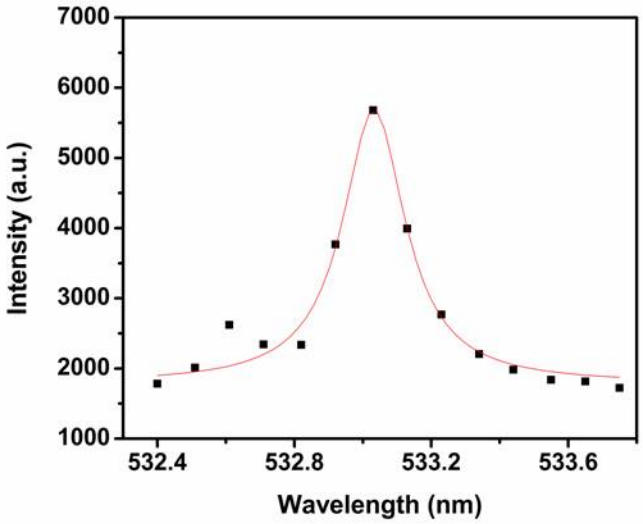

Figure 4.29: The Lorentzian fit of the Stark broadened CrI (532.91 nm) line.

The equation above was used to determine the electron number density in this study. For the calculation of electron density, the Stark-broadened neutral CrI (532.91 nm) line, which is well-isolated from other spectral lines, is fit to a Lorentzian function. The Lorentzian fit to the observed CrI (532.91 nm) line is depicted in figure 4.29. The electron impact-width parameters (W) for the chosen line, interpolated for temperature, were obtained from [109].

The Doppler broadening also could be a source of the line broadening [82]. Using the following equation, potential impact of how Doppler line broadening, resulting from thermal motion of the emitting atoms, would affect the shape of the emission line in this present study was examined.

$$\Delta\lambda_D = \frac{\lambda_c}{c}\sqrt{\frac{2kT}{m}}, \tag{4-8}$$

where λ_c is the center wavelength (nm), c is the speed of the light (m/s), T is the temperature (K), k is Boltzmann's constant ($g \cdot m^2/s^2$) and m is the atomic weight (amu), respectively. The calculated Doppler-broadened width ($\Delta\lambda_D$) is in the range of 0.0028-0.003 nm for the range 7800-9200 K, which were the temperatures measured in this study. Compared with the Stark width (~0.2 nm), the Doppler-broadened width is much smaller, indicating that the effect of the Doppler broadening is negligible in this study.

There is another line broadening mechanism called natural broadening, which results from the energy spread (or frequency spread) in excited and de-excited levels. In general, the effect of the natural broadening is smaller than that of the Doppler broadening by several orders in magnitude; therefore, the effect of the natural line broadening is not considered either. Thus, Stark broadening seems to be the dominant mechanism for the spectral line broadening seen in this study, and it is the only effect considered in this study.

Figure 4.30 shows the electron number density as a function of drilling depth. The electron number densities shown in the figure are the average of data obtained during each drilling pass. For accurate determination of N_e, only the data with good fitting

quality were used (generally, data with peak intensity above 1000). The calculated electron number densities calculated vary in a similar manner to the electron temperature. For example, the electron number density decreases as drilling depth increases. This indicates that as drilling depth increases, the intensity of laser beam decreases because the beam gets defocused. This, in turn, results in the decrease of material removal. In addition, the decrease in the electron number density is partially due to the variation in the plasma sampling location because an increase in drilling depth moves the plasma sampling location from the core to the outer edge of the plasma. Specifically, particle density in plasma tends to decrease as the sampling location moves from the core to the outer region.

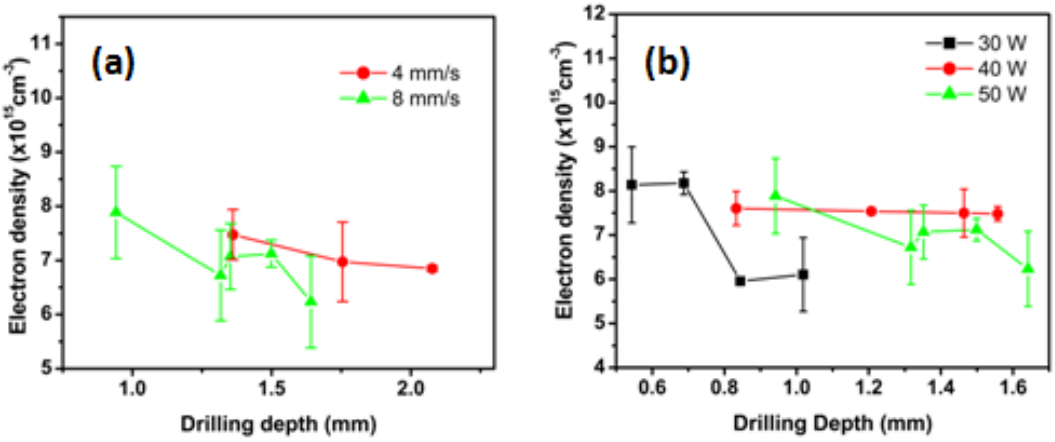

Figure 4.30: Electron number density as a function of drilling depth (a) for different speeds and (b) for different laser powers.

4.4.2 Plasma diagnostics in DMD process

In this study, the correlation between the ratios of emission line intensities and the ratios of elemental compositions in deposits was investigated for two main elements of Inconel 718, Ni and Cr. For this study, representative atomic lines for Ni and Cr were carefully selected from the emission spectra shown in figure 4.31. Lines were identified based on [108]. One NiI (352.45 nm) line and Two CrI lines (396.36 nm and 399.11 nm) were chosen to determine the ratio (NiI/CrI) of the line intensity. These lines are relatively strong and do not overlap with other lines. They also have high transition probabilities, allowing easy detection of the lines. Table 4.7 shows the spectral data of the lines selected.

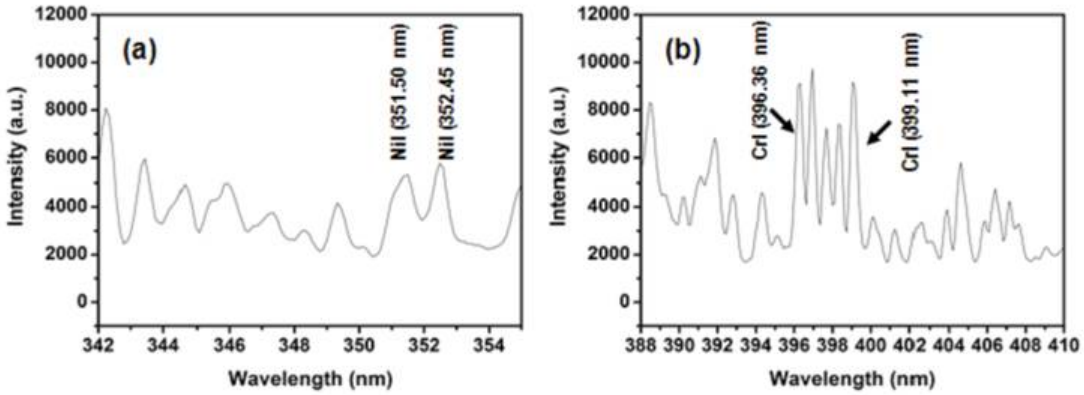

Figure 4.31: Emission spectrum of Inconel 718 for wavelength between (a) 342-355 nm and (b) 388-410 nm region.

Table 4.7: Spectral data for the nickel and chromium lines selected.

Wavelength (nm)	Upper energy level (eV)	Lower energy Level (eV)	g (degeneracy)	A (10^7/s)
NiI, 352.45	3.5419	0.0253	5	10.0
CrI, 396.36	5.6709	2.5439	15	13.0
CrI, 399.11	5.6491	2.5436	7	10.7

In this section, analysis for the quantitative correlation between the line intensity ratio and elemental composition ratio is presented. In order to describe the phenomena relating to melt pool temperature, the dimensionless number composed of material properties and important process parameters is introduced. The dimensionless number used in this study is as follows:

$$\frac{Pd}{\alpha f u} = \frac{P\left(d/u\right)[\mathrm{J}]}{\alpha f[\mathrm{J}]}, \tag{4-9}$$

where P is the laser power (W), d is the beam diameter (constant d is used in this study) (m), f is the powder feed rate (kg/s), and u is the laser scanning speed (m/s), and α is the thermal diffusivity (m^2/s). d/u denotes the laser interaction time. By rearranging parameters, the dimensionless number can be expressed as the ratio of applied energy (numerator) to energy loss (denominator) for the process (left hand side of Eq. 4-9). For a given laser energy, a large α (thermal diffusivity) and powder feed rate would result in a small dimensionless number. Under the condition, the melt pool temperature is expected to decrease because of greater heat loss to the substrate and laser energy absorption by larger mass. By contrast, for relatively small energy loss (large dimensionless number), the melt pool temperature is expected to increase.

Figure 4.32 shows Ni/Cr composition ratio on the layers deposited under different process conditions indicated by the dimensionless number. Each data point corresponds

to the average value obtained under each process condition (indicated by individual dimensionless number). Ni/Cr composition ratio increases with increasing dimensionless number as shown in figure 4.32.

This increase is primarily the result of a decrease of the Cr concentration with increasing dimensionless number, which is expected to increase the melt pool temperature as explained previously. The increase of the melt pool temperature may reduce the Cr concentration because Cr is expected to preferentially evaporate compared to Ni. Cr has a lower boiling point than Ni, 2944K versus 3186K, respectively. The high vapor temperature that results as the melt pool temperature increases may also reduce the concentration of the Cr in the deposited layer through the pre-evaporation and rapid oxidation of the Cr atoms in powder before powder drop on the melt pool.

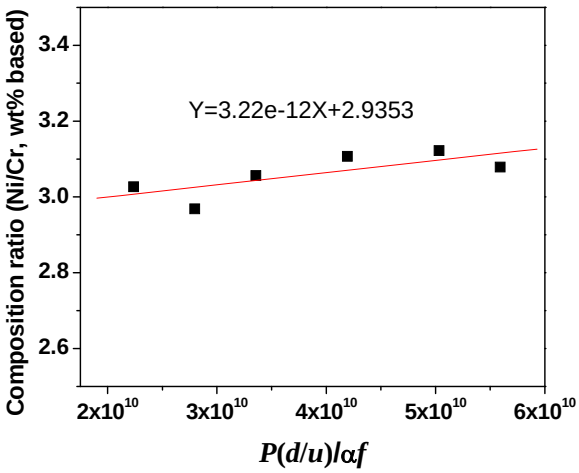

Figure 4.32: Ni/Cr composition ratio as a function of the dimensionless number.

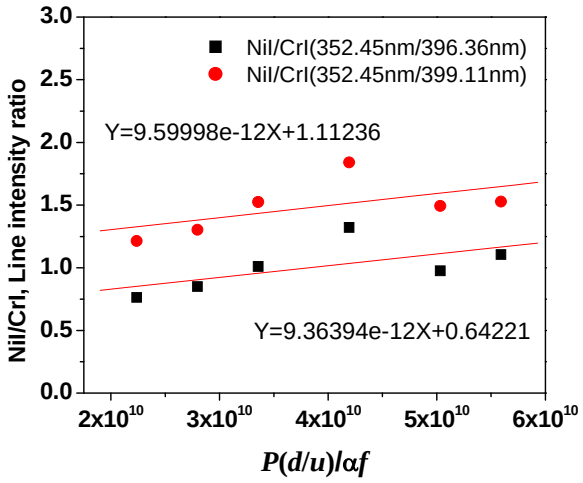

Figure 4.33: NiI/CrI line intensity ratio as a function of the dimensionless number.

Figure 4.33 shows NiI/CrI line intensity ratio as a function of the dimensionless number. As seen in the figure, the NiI/CrI line intensity ratio has a proportional relationship with the dimensionless number. The reason for the larger intensity ratio in the middle is not clear. Measurement error resulting from unstable factors (non-uniform powder feeding, fluctuation in laser power and its effect on the interaction with plasma, etc.) may play a role for that. As mentioned above, the increase of the dimensionless number will increase the temperature of the melt pool. Higher melt pool temperature will result in a higher plasma temperature. It is known that Cr is primarily oxidized among the elements constituting Ni-base alloys when solid-state Ni-base alloys are exposed to a hot oxidation environment [111, 112]. In fact, Cr has a lower ionization potential compared to Ni, therefore, it can be more easily ionized in the plasma and interact with oxygen to form oxides. Table 4.8 shows the ionization potential for Cr and Ni. The oxygen residing near laser-material interaction region could promote the oxidation of Cr atoms in plasma/plume with increasing temperature. This will preferentially decrease the

population of the pure Cr atom in plasma/plume and relatively further reduce the intensity of CrI line. As a result, the NiI/CrI line intensity ratio increases with increasing the dimensionless number.

Table 4.8: Ionization potential for Cr and Ni.

Element	1st ionization potential	2nd ionization potential
Ni	737.1 kJ/mole	1753.0 kJ/mole
Cr	652.9 kJ/mole	1590.6 kJ/mole

The correlation between line the intensity ratio and composition ratio is obtained by combining the two empirical correlations shown in figures 4.32 and 4.33. The line intensity ratio has a proportional relationship with the composition ratio as shown in figure 4.34 because of the similar behavior of both parameters for the dimensionless number.

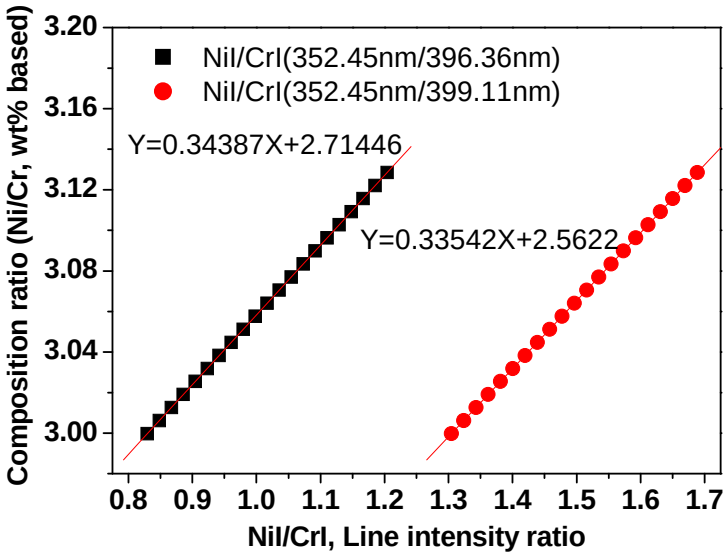

Figure 4.34: Correlation between line intensity ratio and composition ratio.

4.5 Numerical simulation of pulsed laser drilling

4.5.1 Case study for the effect of pulse format on the laser drilling process

4.5.1.1 Case study 1: numerical simulation for comparison of drilling performance between a conventional pulse format and pulse format incorporating beam modulation

Three different pulse formats have been designed to investigate the effect of pulse format on laser drilling performance. Table 4.9 and figure 4.35 show detailed descriptions of the pulse formats. One formal is the modulated laser beam which has a series of regularly spaced micro-pulses with high peak power within the envelope of the macro-pulse. Each micro-pulse has the same beam intensity. The other two pulse formats employ single pulses with different pulse widths. For each, simulation is carried out using the same average power (3 kW). The energy per pulse (in the case of the modulated beam, this means the summation of energy of all micro-pulses within one macro-pulse) is also the same due to the use of the same pulse repetition rate. A 500 μm beam diameter and 3 mm workpiece thickness have been used for this simulation.

Table 4.9: Simulation parameters for three different pulse formats.

Classification	Case	Pulse repetition rate	Pulse width	Beam intensity
Modulated beam (No. of micro-pulses in one macro-pulse: 15)	1	1 kHz	- Macro-pulse width: 150 μs - Micro-pulse width: 200 ns - Micro-pulse spacing: 10 μs	5.09296248×10^{8} W/cm^2
Non-modulated beam	2	1 kHz	150 μs	1.01859249×10^{7} W/cm^2
	3	1 kHz	500 μs	3.0557775×10^{6} W/cm^2

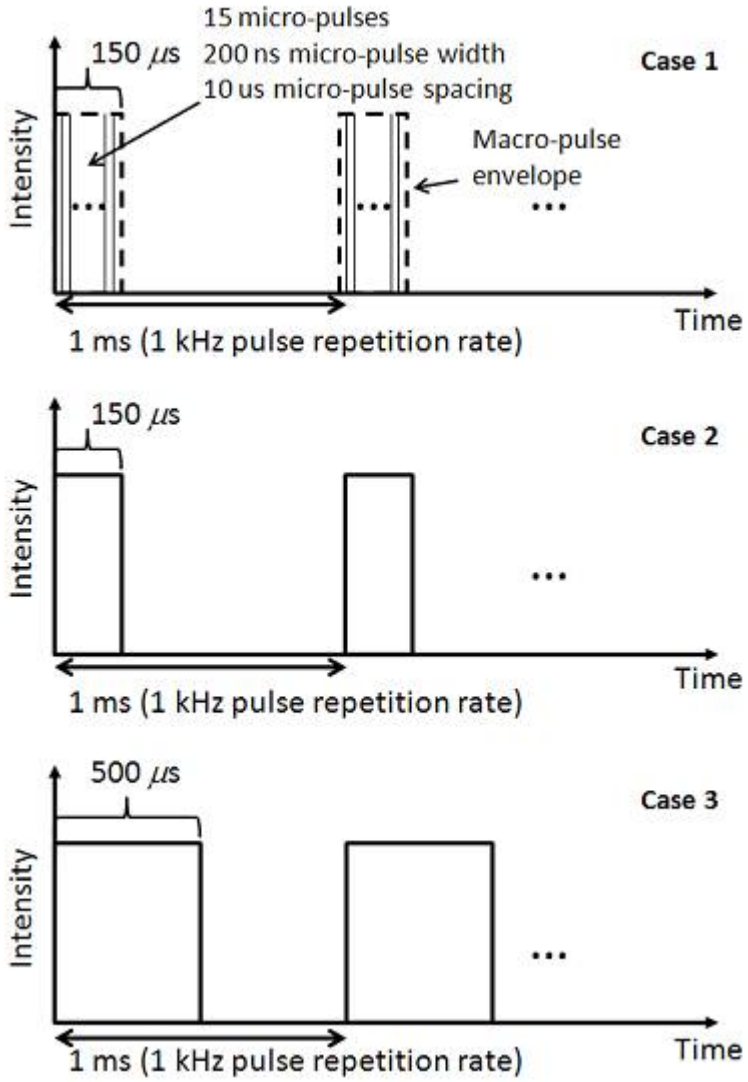

Figure 4.35: Schematic description of pulse formats studied.

Figure 4.36 shows the effective laser absorptivity (the ratio of the laser energy absorbed by the cavity to total laser energy) for laser-created cavities as a function of the drilling time. Laser energy absorption of the laser-created cavity increased as a hole depth increased through multiple reflections of laser beam inside the cavity. As shown in the

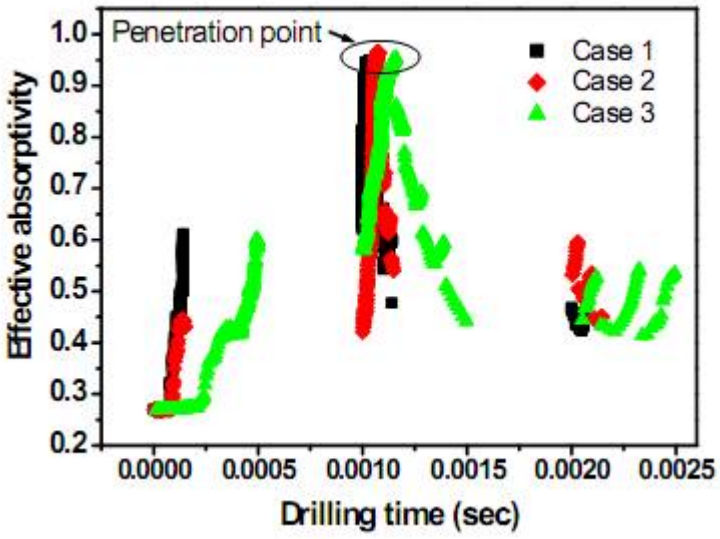

Figure 4.36: Temporal profile of effective laser absorptivity by a laser-created cavity.

figure, almost 95% of the laser energy is absorbed by the cavity just before hole penetration. After penetration, it tends to decreases because energy loss occurs through the exit hole. Figure 4.37 shows temperature profiles at the liquid / vapour surface along the radial direction at the moment of hole penetration. For the three different pulse formats, the surface temperature increased as the applied beam intensity increased (from case 3 to case 1). The surface temperature is usually far beyond the normal boiling point as shown in the figure due to the irradiation by high power density beam. In the case of the modulated laser beam (case1), the surface temperature for the considerable portion of the irradiation area is in the regime of homogeneous boiling; however, this phenomenon is only limited to the central zone (the center of the cavity) of the hole for case 2 and 3, which use non-modulated beams.

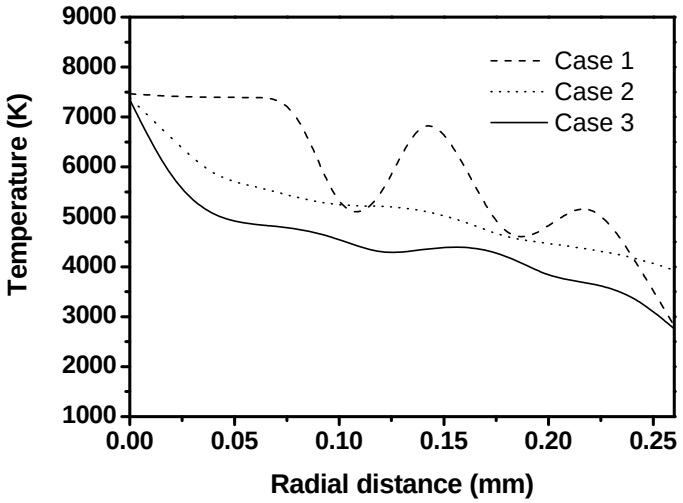

Figure 4.37: Surface temperature profile along the radial direction.

Figure 4.38 shows laser-created hole profiles at different drilling times. It is seen that the modulated pulse format (case 1) yields the highest drilling rate consistently at a given time until a hole is penetrated among three different pulse formats. From the graphs for case 1 and case 2, it is observed that using the modulated beam with relatively high beam intensity enhances the drilling rate under the same duty ratio (pulse width × pulse repletion rate) of the laser.

Figure 4.39 shows a hole penetration time. For all cases, hole penetration occurs during the 2nd macro pulse. The modulated beam takes the least time to penetrate the hole. The above results suggest that the modulated beam with a high peak power can be efficiently adopted in manufacturing to reduce the process time. Among two non-modulated beams, the case 2 with relatively shorter pulse width and higher intensity also requires less time to penetrate the hole; however, as can be seen from figure 4.40, the case 2 spends more accumulated laser energy to penetrate hole.

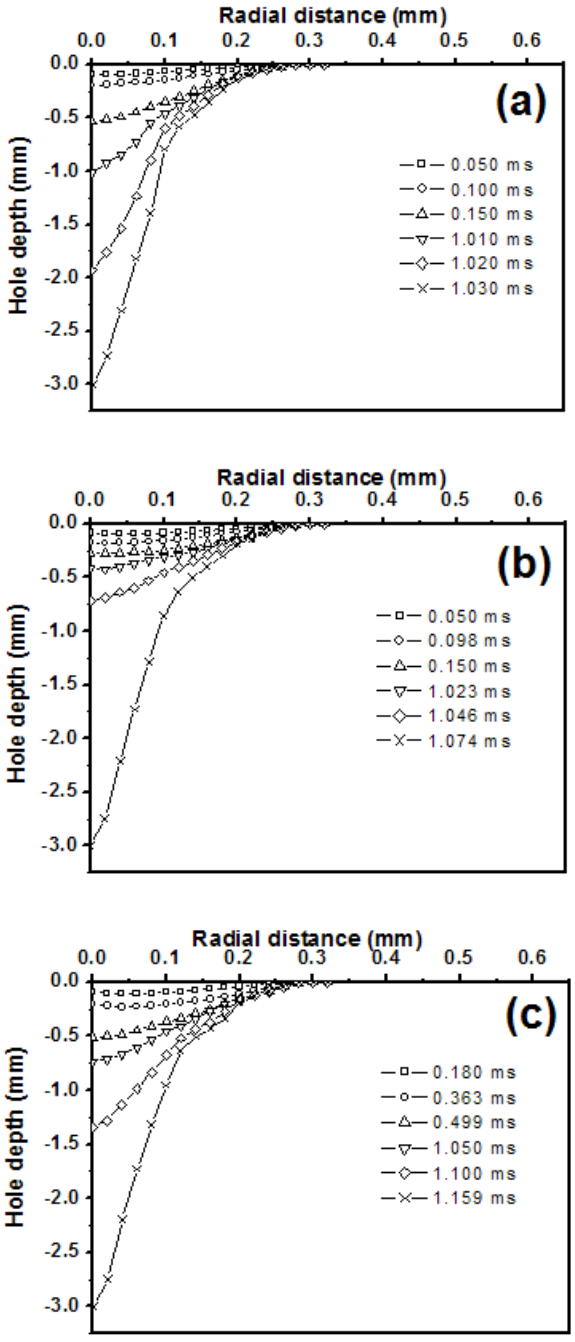

Figure 4.38: Temporal cavity profile for (a) case 1, (b) case 2, and (c) case 3.

Since the energy per pulse is same for both cases, case 2 will spend pulse energy further for a given time (spending of a greater fraction of the pulse energy within 150 μs)

compared to case 3 with longer pulse width (500 μs). Thus, the faster hole penetration in the case 2 can be ascribed to the more use of the laser energy compared to the case 3 during the irradiation of the 2nd pulse.

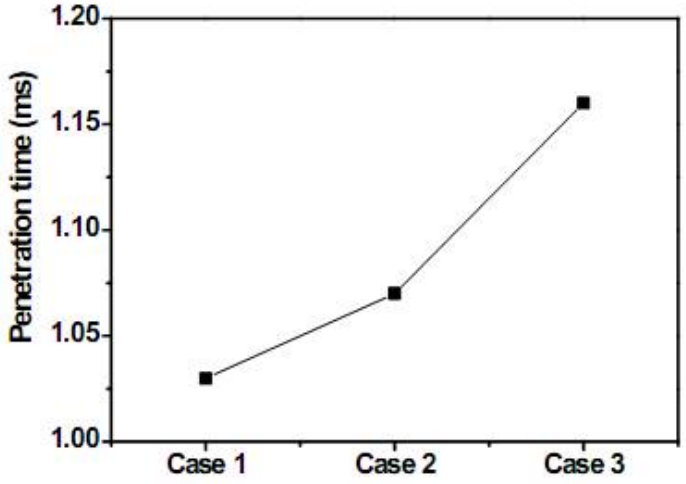

Figure 4.39: Hole penetration time.

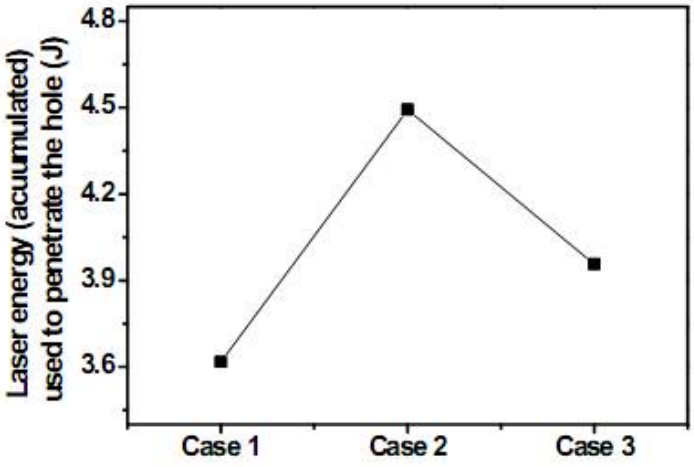

Figure 4.40: Accumulated laser energy used to penetrate a hole.

Also, faster heating of the material under the higher beam intensity may contribute to a reduction in the hole penetration time for the case 2. As shown from figure 4.39 and 4.40, the modulated pulse format enhances drilling performance. It is also more effective in the utilization of the laser energy.

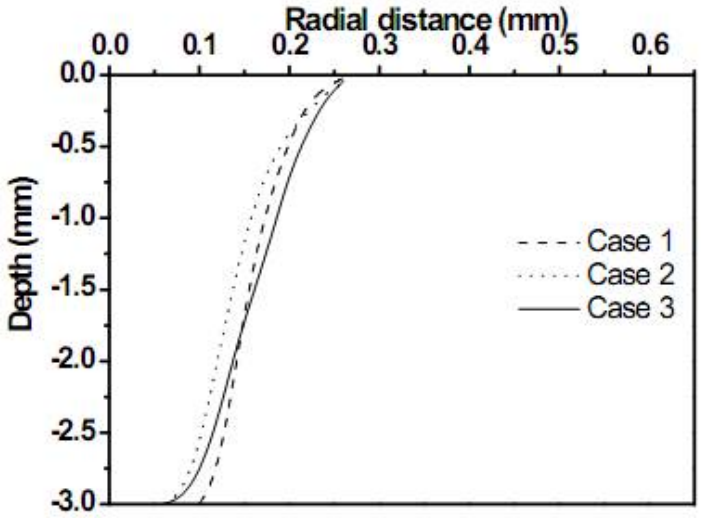

Figure 4.41: Hole shape after the 2nd pulse (the 2nd macro pulse envelope for case 1).

Figure 4.41 shows the profile of the holes created by different pulse formats after the 2nd pulse irradiation. It is seen that for the same drilling time and same accumulated laser energy, the modulated beam using relatively high beam intensity and short pulse width produces a larger exit hole. After the 2nd pulse, the size of the exit hole is same for case 2 and 3; however, the width of the cavity at a given depth is larger in case 3 than in case 2. This could be explained by the surface recession speed. Figure 4.42 shows the surface recession speed as a function of the radial distance. The surface recession speed tends to vary more gently from the central location to the edge under the lower beam intensity as shown in the figure. This gentle variation in the surface recession speed for the lower

intensity beam (case 3) is more likely to produce the wider cavity due to the gradual increase of the cavity depth along the radial direction. On the other hand, a steep change of the surface recession speed (case 2) is likely to form the narrower cavity shape because of the relatively further increase of the hole depth at the central location.

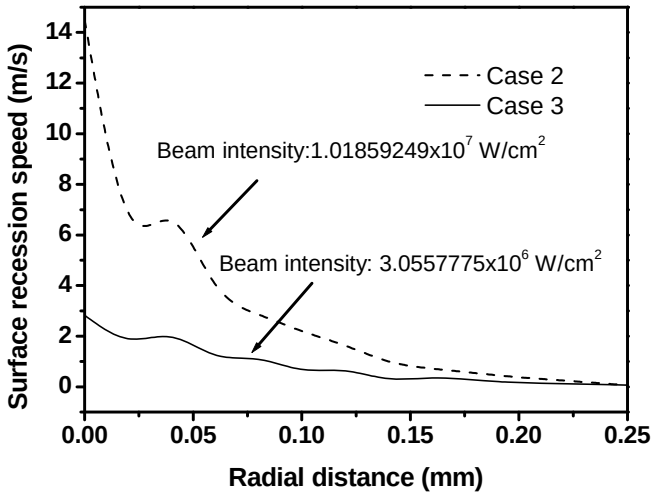

Figure 4.42: Surface recession speed captured at the same hole depth (0.5 mm).

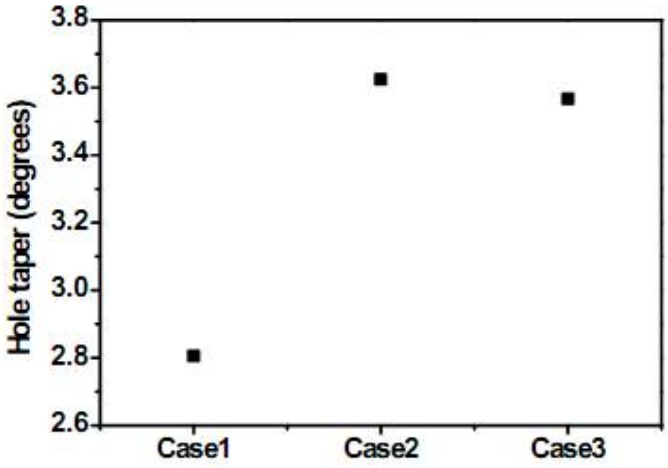

Figure 4.43: Hole taper for each pulse format case.

Figure 4.43 shows the numerical values of the hole taper for each case. Hole taper was determined using Eq. 3-1 and the results from figure 4.41. It is clearly seen that the modulated beam produces less hole taper because it generates a larger exit hole size.

The thickness of the recast layer is shown in figure 4.44. The liquid layer produced during the laser-material interaction solidifies and forms the recast when the irradiation is completed. The recast is generally considered as the defect which increases the chance of crack development at the hole wall. In addition, the thermophysical and mechanical properties of the recast could be different from those of the workpiece; therefore, minimizing the recast is desirable in laser-aided material processing.

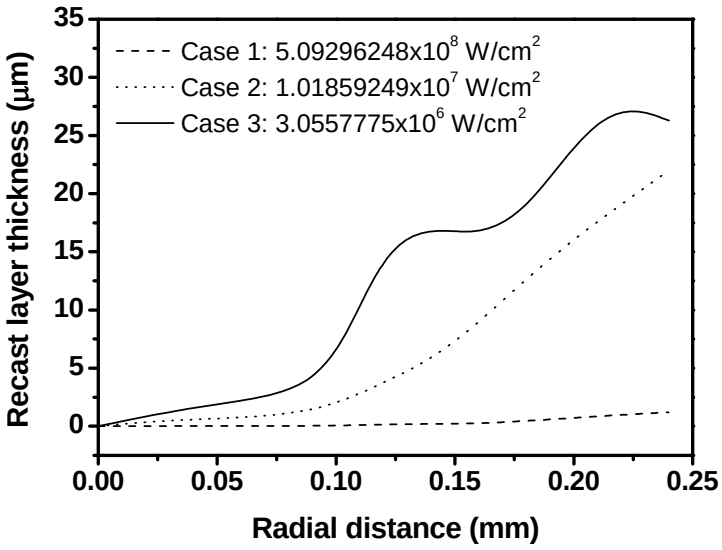

Figure 4.44: Recast layer thickness along the radial distance.

It is seen that the thickness of the recast has minimum value at the central location and it tends to increase with radial distance. A very thin recast layer (below 1 μm) is produced in the case of the modulated beam, which uses a higher beam intensity. The

recast layer thickness decreases with increasing beam intensity as shown in the figure. This is attributable to the fact that as the beam intensity increases, the process becomes more vaporization dominated, and liquid layer produced becomes thinner. The above result indicates that significant formation of the recast layer can be avoided by using a high peak power and short pulse laser.

4.5.1.2 Case study 2: numerical simulation for comparison of drilling performance between the DP-11 pulse format and a double pulse format

A double pulse, (sometimes referred as a super pulse, method has recently been explored for various laser systems to improve drilling [113-115]. It is reported that for a nanosecond pulsed laser, the double pulse method could increase drilling speed by several times compared to a conventional pulsed laser [116]. In the double pulse format, two closely spaced pulses burst at a high repetition rate (~10 kHz). A separation time of two neighboring pulses generally ranges from several nanoseconds to several hundred nanoseconds.

The DP-11 (this is the name of the model of the laser used in the drilling experiment, see section 3.3.1) type pulse format corresponds to the conventional modulated laser beam, which was case 1 shown in section 4.5.1.1, and the conditions of case 1 are used again for the DP-11 pulse format in this study. Table 4.10 and figure 4.45 provide details about the pulse formats used for this study.

Table 4.10: Pulse parameters for DP-11 and double pulse formats.

Classification	Pulse repetition rate	Pulse width
DP-11 pulse format (No. of micro-pulses in one macro-pulse: 15)	1 kHz	- Macro-pulse width: 150 μs - Micro-pulse width: 200 ns - Micro-pulse spacing: 10 μs
Double pulse format (or super pulse)	10 kHz	- 200 ns - Pulse spacing: 20 ns – 10 μs

A 500 μm beam diameter and 3 mm workpiece thickness are again used for the simulation. The simulation is carried out for various power levels. Table 4.11 shows the values of the beam intensity for various average powers.

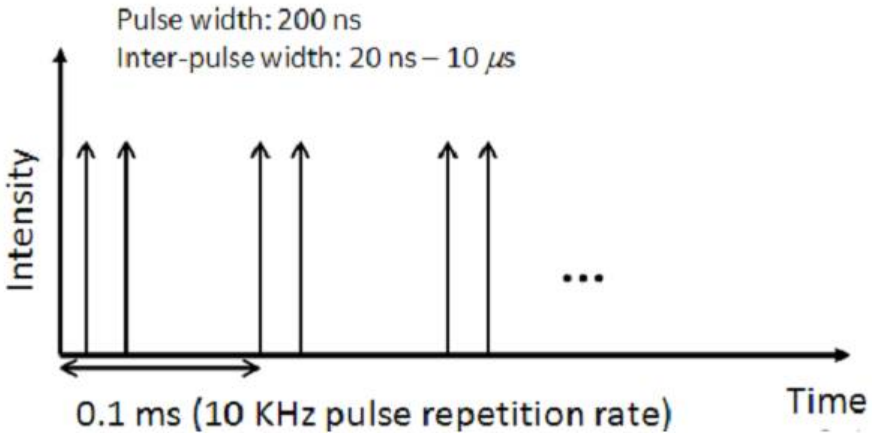

Figure 4.45: Schematic diagram of double pulse format.

Table 4.11: Beam intensity for average powers.

Power (kW)	Beam intensity (W/cm^2)	
	DP-11	Double pulse (DP)
3.5	5.941789561×10^8	4.45634217×10^8
3.25	5.51737602×10^8	4.13803201×10^8
3	5.09296248×10^8	3.81972186×10^8
2.5	4.24413540×10^8	3.18310155×10^8
2	3.39530832×10^8	2.54648124×10^8
1.5	2.54648124×10^8	1.90986093×10^8
0.75	1.27324062×10^8	9.5493046×10^7
0.375	6.3662031×10^7	4.7746523×10^7

Figure 4.46 shows the drilling depth obtained from 5 different drilling conditions (one for the DP-11 pulse format and four for the double pulse format) after 1 ms drilling time. As described on the horizontal axis in the figure, 4 different inter-pulse spaces were used to simulate the various double pulse conditions. This simulation is carried out using the same average power, 3 kW. As can be seen from the figure, the double pulse formats generally result in better drilling performance. In addition, the double pulse format uses less laser energy to penetrate a hole, as shown in figure 4.47, which in turn, is more effective in the use of the laser energy. In particular, the double pulse format with 20 ns pulse spacing yields the best performance due to the effect of more pre-heating resulting from the shorter cooling time. From figure 4.48, it is clearly seen that for 20 ns inter-pulse spacing surface temperature is already far beyond the boiling point before the irradiation of the consecutive pulse begins.

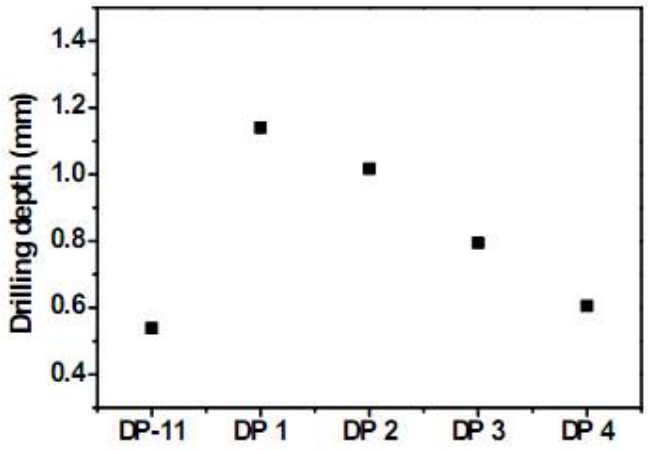

Figure 4.46: Drilling depth (after 1 ms) for various pulse formats: (DP 1, 2, 3 and 4 denote a double pulse format with 20 ns, 110 ns, 200 ns, and 10 μs inter-pulse spacing, respectively).

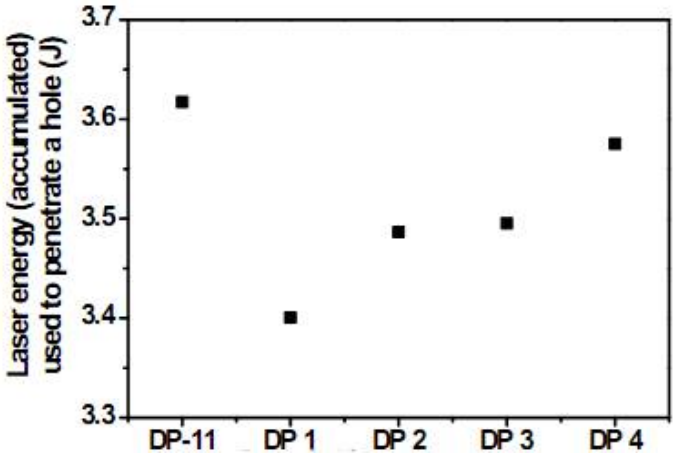

Figure 4.47: Accumulated laser energy used to penetrate a hole (DP 1, 2, 3 and 4 denote a double pulse format with 20 ns, 110 ns, 200 ns, and 10 μs inter-pulse spacing, respectively).

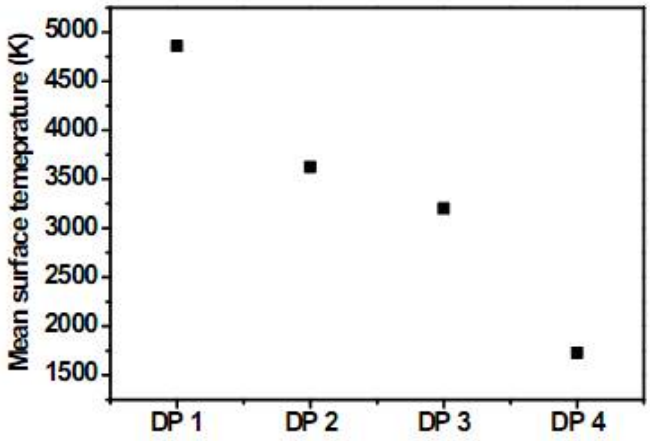

Figure 4.48: Mean surface temperature obtained at the end of the inter-pulse spacing after the leading pulse in the first pair of pulses (DP 1, 2, 3 and 4 denote a double pulse format with 20 ns, 110 ns, 200 ns, and 10 μ s inter-pulse spacing, respectively).

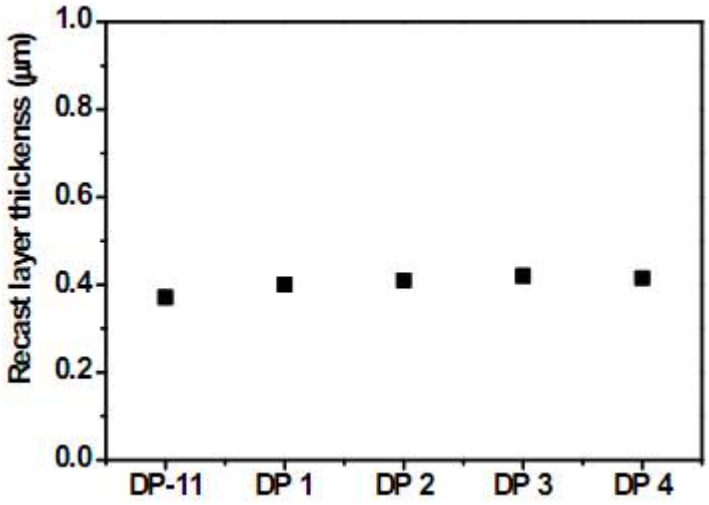

Figure 4.49: Recast layer thickness (DP 1, 2, 3 and 4 denote a double pulse format with 20 ns, 110 ns, 200 ns, and 10 μ s inter-pulse spacing, respectively).

The recast layer produced is generally very thin for all cases as shown in figure 4.49. A little bit thinner layer is obtained for the DP-11 pulse format because of using a higher beam intensity and more vaporization; however the noticeable difference in the recast thickness is not observed.

This case study is further carried out for various laser power levels. In the following simulation, the DP-11 pulse format is compared with the double pulse format with 20 ns inter-pulse spacing, which showed the best drilling rate among the four different conditions of the double pulse format shown earlier. Figure 4.50 shows the drilling depth after the drilling time of 1 ms. Since the accumulated laser energy every 1ms is same for two pulse formats, this allows a comparison of the drilling performance when utilizing the same amount of the laser energy. As shown in figure 4.50, the drilling performance of the two pulse formats depends on the laser power used. It is revealed that below 3 kW the performance of DP-11 is better than the double pulse format, however more than 3 kW the double pulse format shows the better drilling performance

The performance of the DP-11 pulse format tends to relatively decrease (separation in the drilling depth for two pulse format tends to decrease) from the laser power of 2 kW as shown in figure 4.50 (a). This indicates that the drilling depth (obtained under the same drilling time and the same amount of laser energy) for the double pulse format increases more from 2 kW as compared to the DP-11 pulse format. Eventually, the double pulse format generates a deeper hole from 3 kW as shown in figure 4.50 (b). As shown in figure 4.50, drilling depth increases significantly from the laser power of 3 kW. The enhanced multiple reflections of the laser beam with increasing hole depth contributes to the large increase of the drilling depth for high powers.

Figure 4.51 shows the hole penetration time at different power levels. Below 3 Kw, the DP-11 pulse format generally takes the less time to penetrate a hole; however, when laser power is greater than 3 kW, the double pulse format shows a shorter penetration time except at 3 kW. According to the result from simulation, the laser power of 3.25 kW (central point) may be near the transition region where the ability of two pulse formats (i.e., penetrating a hole in a shorter time) is switched. The shorter penetration time of the DP-11 pulse format in the case of the 3 kW power is attributable to the more utilization of the laser energy compared to the double pulse format for a given time as shown in figure 4.52. Figure 4.52 shows the accumulated laser energy used to penetrate a hole. At relatively low power levels, the DP-11 pulse format usually needs less energy to penetrate a hole, however it requires more laser energy than the double pulse format with increasing power as shown in the figure.

From the figures 4.51 and 4.52, it can be concluded that at the relatively high power (above 3 kW) the double pulse format not only reduces drilling time but also is effective in the utilization of the laser energy (i.e., total amount of the laser energy used to penetrate a hole is less), and below 2 kW the DP-11 pulse format results in better performance with respect to drilling time and laser energy utilization.

Under the given conditions for two pulse formats and the same average power, the beam intensity of the DP-11 pulse format is larger than that of the double pulse format as shown in Table 4.11. On the other hand, the double pulse format has the larger number of pulses than the DP-11 pulse format (i.e. the double pulse format has 20 pulses every 1 ms; however, the DP-11 pulse format has 15 pulses). Depending on the power (or beam

intensity) used, two pulse formats yield the different behavior in drilling performance as shown in the figures 4.50 through 4.52.

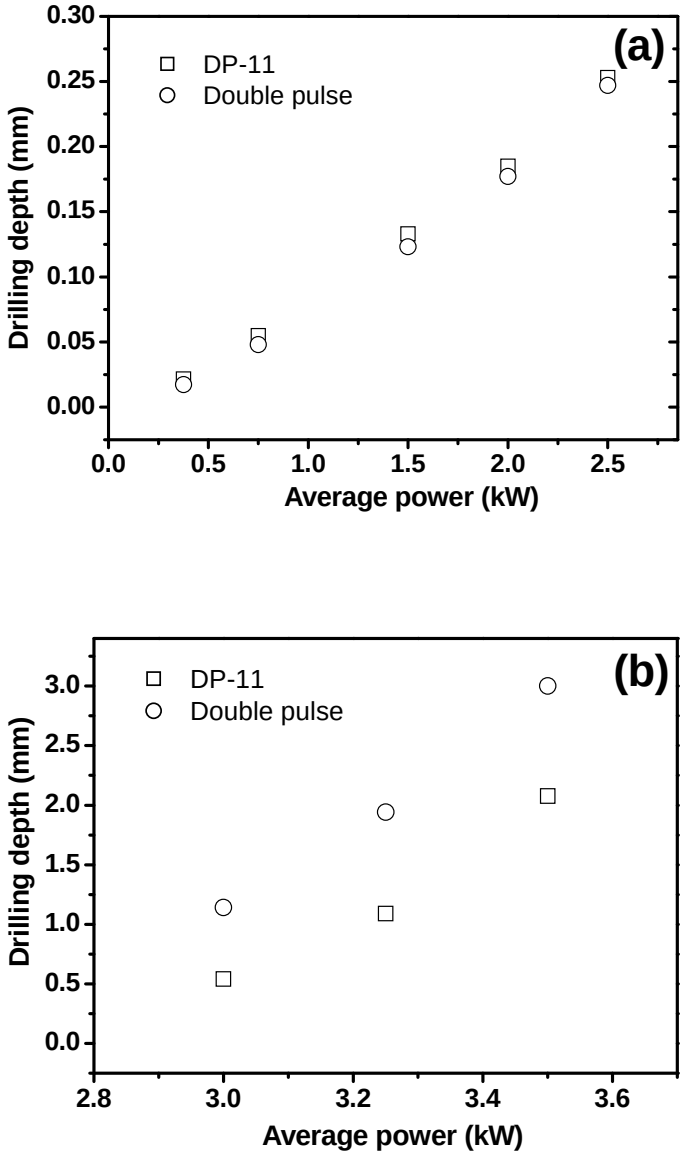

Figure 4.50: Drilling depth after 1 ms: (a) for the power range of 0.375 – 2.5 kW and (b) for the power range of 3 – 3.5 kW.

Based on results, increasing the number of pulses (or using the double pulse format) is more effective in the enhancement of the drilling performance at the relatively high

power (or high beam intensity) levels; however, increasing the intensity of the laser beam (or using the DP-11 format) improves the drilling performance more than increasing the number of pulses at the relatively low power levels.

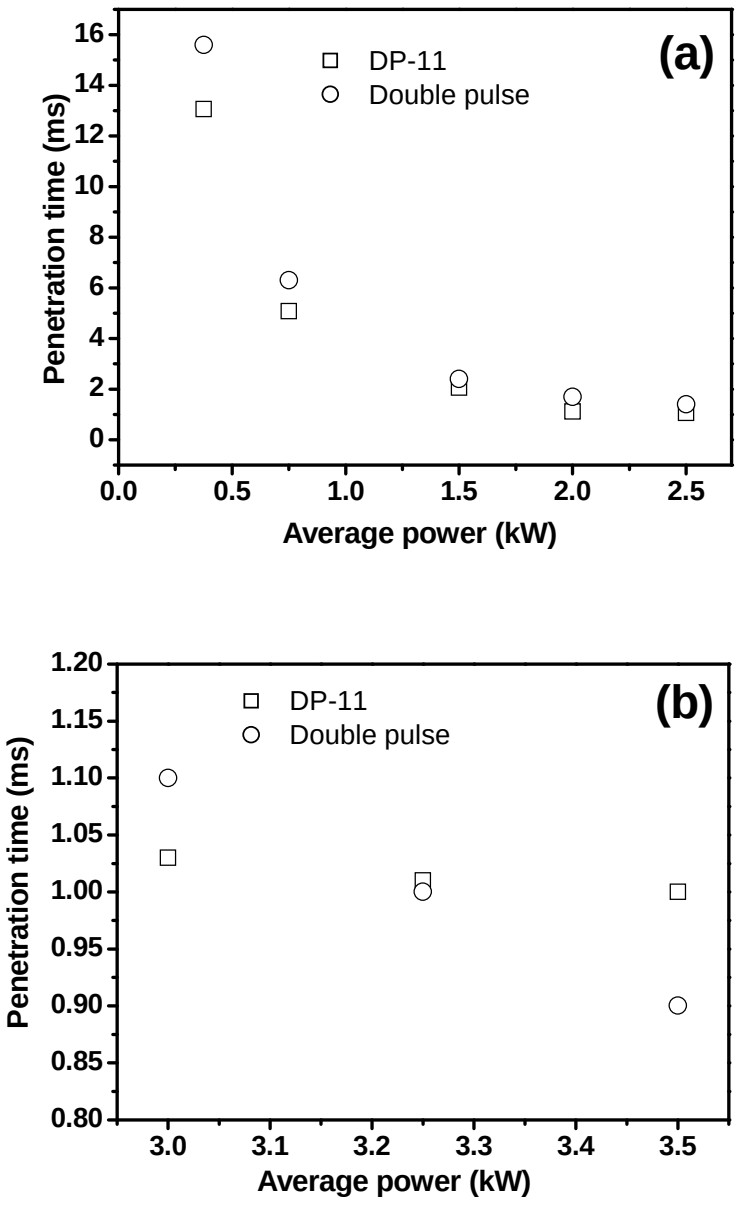

Figure 4.51: Penetration time: (a) for the power range of 0.375 – 2.5 kW and (b) for the power range of 3 – 3.5 kW.

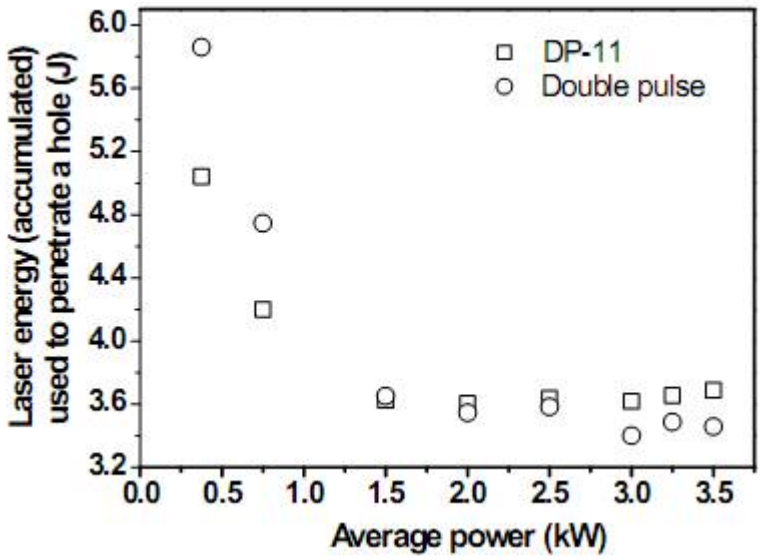

Figure 4.52: Accumulated laser energy used to penetrate a hole at different power levels.

4.5.2 Experimental validation of the computation model

In this section, work to validate the computation model is presented. The process conditions used for this work are shown in Table 4.12.The laser used in this experiment was the DP-11 mentioned in section 3.3.1.

Table 4.12: Process conditions used to validate the computation model.

Classification	Pulse width	Beam intensity
Without modulation	200 μs	1.70993×10^{6} W/cm^2
With modulation (20 micro pulses in one macro pulse)	200 μs (pulse width of micro-pulse: 200 ns)	8.5496529×10^{7} W/cm^2
Average power	65 W	
Pulse repetition rate	500 Hz	
Workpiece thickness	3 mm	
Beam spot size	220 μm	

In the simulation, a lower intensity was used to consider the effect of the plasma absorption. In order to consider the plasma absorption of the laser energy, an experiment measuring laser power behind the exit hole was carried out during the laser drilling process. For this experiment, the modulated laser beam and the conditions shown in Table 4.12 were used. The measured laser power tended to increase as the exit hole size increased, as shown in figure 4.53. The calculated values in the figure mean power passing through the hole of the corresponding size under the absence of the plasma (It is assumed that the beam has the Gaussian distribution). It is considered that the difference between the measured power and the calculated power is mostly due to the plasma absorption of the laser energy in the actual measurement. The difference between the measured power and the calculated power tends to decrease as hole size increases because of the weakened plasma caused by the hole expansion and reduced material removal. Based on this result, the plasma absorbed approximately 54 % of the laser power at the initial stage of hole break through (at the first data point in the figure 4.53). This reduced laser power is used as the input source for the simulation.

Figure 4.54 shows the comparison of the drilling depth between experimental data and numerical simulation. The cross sections of laser drilled holes are shown in figure 4.55. In the case of the modulated beam, the hole penetration time obtained in the experiment is around 0.6 s. The simulation well predicts this as shown in the figure. Unlike the modulated beam, the non-modulated beam using low beam intensity doesn't penetrate a hole in spite of the relatively long drilling time even though it uses the same average power. In the case of the non-modulated beam, it is found that after certain point the

workpiece just starts to glow without the further increase of the hole depth. It is considered that initially the effect from plasma is not significant, however the plasma absorption of the laser beam reduces beam intensity further due to the elevated interaction between the laser beam and plasma as the hole depth increase. Eventually, the beam intensity becomes not enough to remove material, and this seems to result in a cycle just repeating melting and solidification after a certain point.

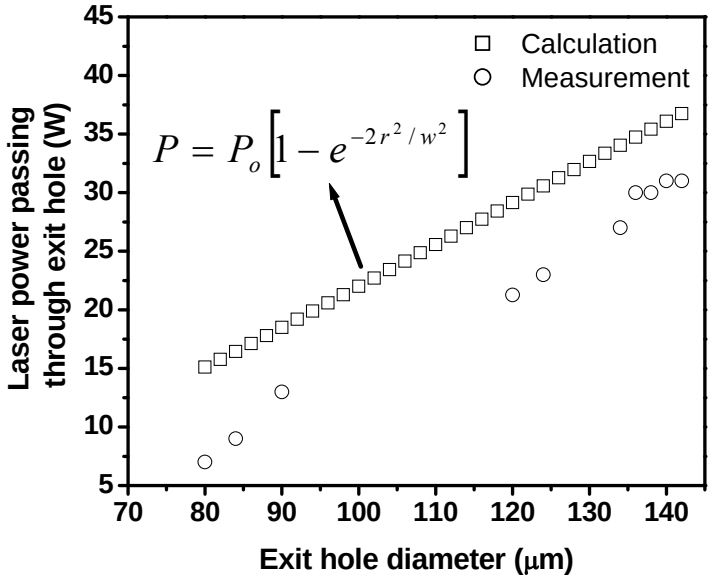

Figure 4.53: Laser power passing through the exit hole (*P* denotes laser power passing through a circle or hole of radius *r* and *w* denotes a size of beam radius).

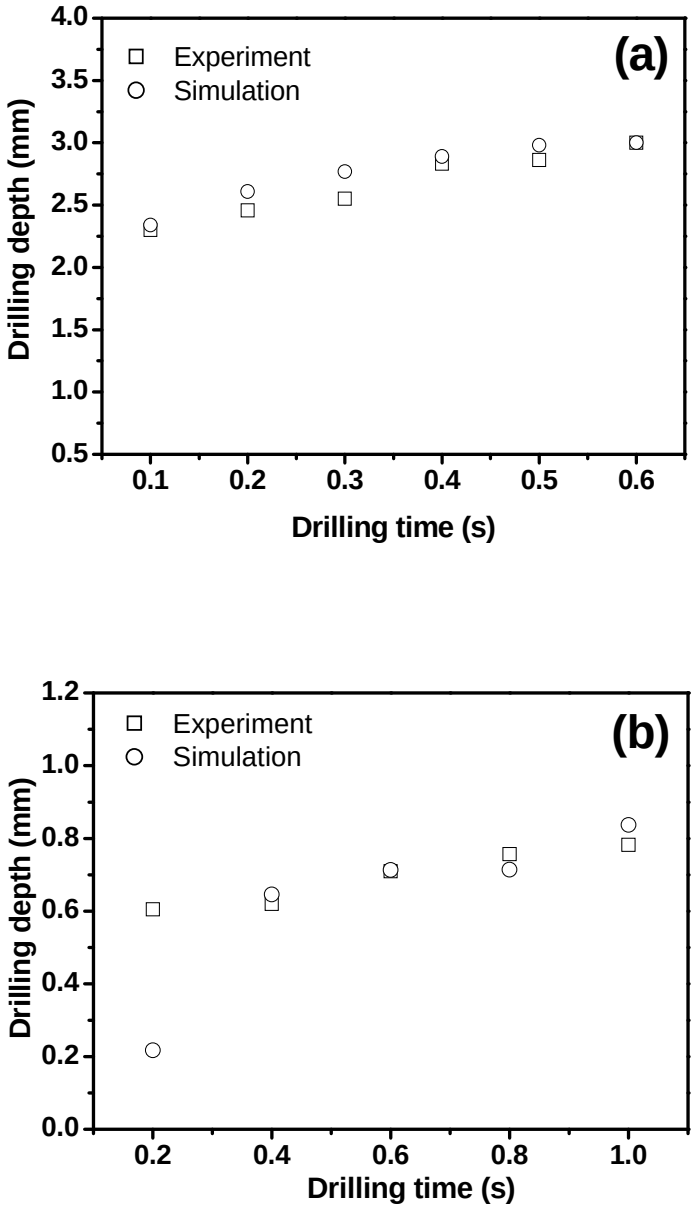

Figure 4.54: Comparison of drilling depth for: (a) the modulated beam and (b) the non-modulated beam.

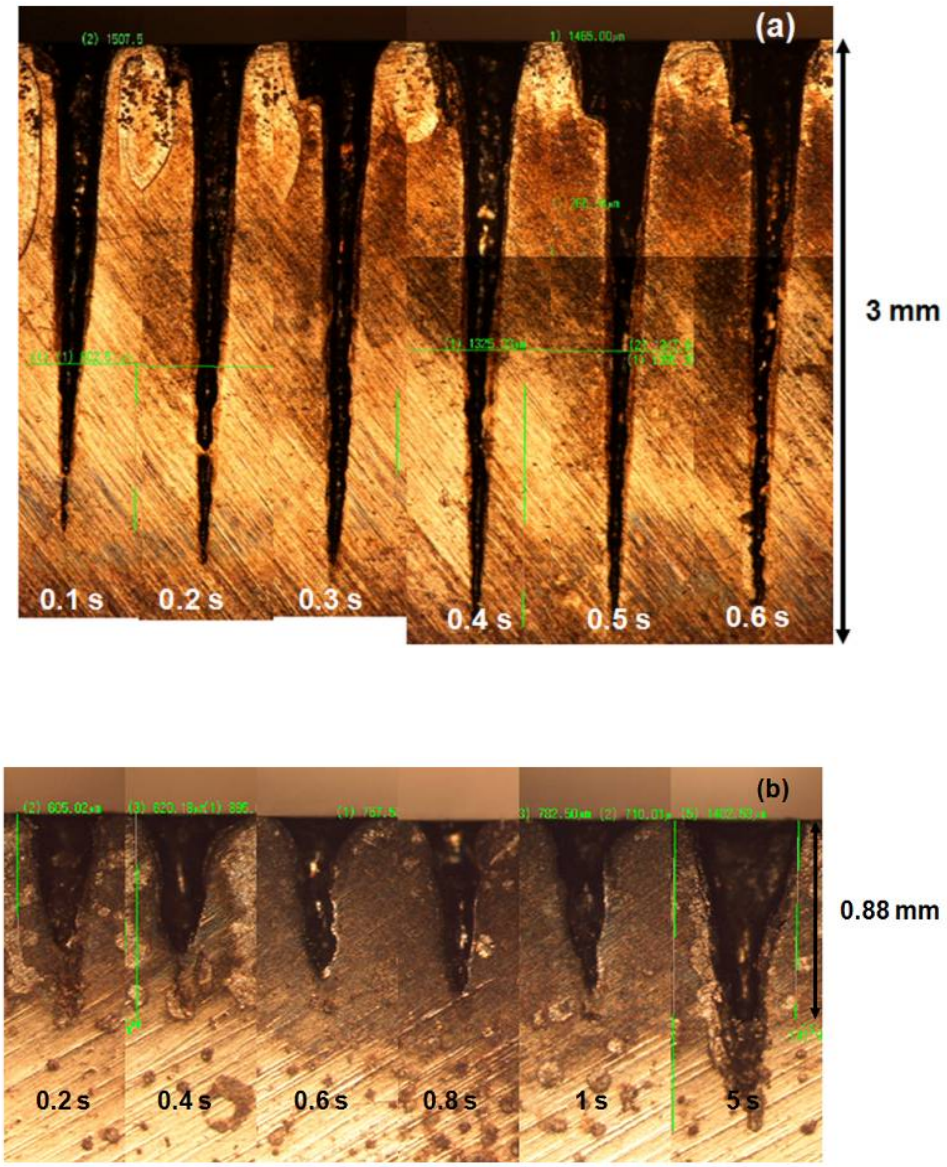

Figure 4.55: Hole cross section for : (a) the modulated beam and (b) the non-modulated beam.

CHAPTER 5

CONCLUSIONS AND FUTURE WORK

This chapter presents conclusions and some recommended future works for this study.

5.1 Pulsed laser deposition of yttria-stabilized zirconia (YSZ)

In this study, the performance of the pulsed laser deposition (PLD) technique to fabricate high quality YSZ films was evaluated by investigating the properties of the YSZ films produced. The important findings and conclusions of this study are summarized below:

- Very smooth YSZ films are obtained. The measured roughness of the film surface is in the range of 3.5–6.5 nm which is ~ 1% of the film thickness.

- YSZ films deposited are very dense. No cracks and pores are found in the films.

- The mechanical properties of the films turn out to be higher than that of the YSZ coatings produced by other technique such as the plasma-sprayed technique.

- In addition, the stoichiometry of the target is generally well preserved in films within ~ 1.5 %.

- Based on the results, it can be concluded that the PLD produces high quality YSZ films, and it is a potentially acceptable technique in the fabrication of YSZ films for the application of hard and protective coating.

5.2 Pulsed laser deposition of Ni-base superalloy

A single crystal (SC) Ni-base superalloy film was successfully produced on the SC Ni-base superalloy substrate with the same alloy composition by the pulsed laser deposition (PLD) process. Important findings and conclusions of the study are summarized below:

- The homoepitaxial growth of the SC Ni-base superalloy film occurred at the following process conditions: 850 ℃ substrate temperature, 2 J/cm^2 pulse energy, 10 Hz pulse repetition rate, and 90 min deposition time.

- The SC film has a smooth surface in which uniformly distributed small particles of several tens of nanometers exist.

- Films generally exhibited a strong polycrystalline characteristic as substrate temperature and pulse energy increased.

- Based on the Taguchi analysis, it can be concluded that the substrate temperature and pulse energy are the most significant process parameters influencing the structural characteristics of the films. Also, the influence of the pulse repletion rate and deposition time was not found to be significant.

5.3 Drilling of Inconel 718 by a diode-pumped solid state Nd:YAG laser

In this study, holes angled at 30^{o} to the workpiece surface were drilled in 3 mm thick Inconel 718 samples with a diode-pumped solid state Nd:YAG laser.

Important findings and conclusions of the study are summarized below:

- Based on the DOE results, it is concluded that higher laser power, lower speed, and closer placement of the focus to the workpiece surface produce larger exit hole and less tapered. The DOE results also showed that higher laser power, higher speed, and further positioning of the focal position away from the workpiece surface reduced the thickness of the recast layer.

- Under the experimental conditions used in this study, a helical drilling technique produces the best drilling performance among three drilling modes including helical, percussion, and trepan drilling.

- Using O_2 assist gas significantly enhances the drilling performance due to the contribution of the exothermic energy; however, using Ar as the assist gas is not useful to improve the drilling performance.

- Using both the helical drilling technique and O_2 assist gas at a high duty cycle (10 %) produces the best drilling performance while still keeping the drilling time under 5 s for the industrial application.

5.4 Plasma diagnostics during laser material processing

5.4.1 Plasma diagnostics during laser drilling process

In this study, the visible emission spectra of Inconel 718 plasma was obtained during laser drilling. An attempt was made to relate plasma parameters including line intensity, electron temperature, and electron number density to drilling depth. Important findings and conclusions of the study are summarized below:

- Correlations estimating the drilling depth are obtained for various process conditions by relating the line intensity with the drilling depth. The line intensity has an inverse proportional relationship with the drilling depth. It is found that the slope of the correlations tends to increase with increasing trepanning speed and laser power.

- It is found that the electron temperature measured is in the range of 7800-9200 K, and it tends to decrease with drilling depth due to the downward movement of plasma core.

- The electron number density measured varies from ~5×10^{15} to ~8×10^{15} cm^{-3}. The contribution of the Doppler broadening and natural broadening to the broadening of spectral line (CrI, 532.91 nm) is negligible compared to Stark broadening. The electron number density also tends to decrease with increasing drilling depth mostly due to the reduction of material removal.

5.4.2 Plasma diagnostics in DMD process

The emission spectra of the Inconel 718 in the near-UV was observed during the DMD process. The observed plasma was investigated to determine the elemental

composition of deposits created during the process. In order to describe the phenomena observed in relation to melt pool temperature, a dimensionless number composed of material property and important process parameters has been introduced. Important findings and conclusions of the study are summarized below:

- It is revealed that Ni/Cr composition ratio in deposits tends to increase with increasing dimensionless number due to the further increase of the evaporation rate of the Cr (more reduction of Cr concentration in deposits) and pre-evaporation / rapid oxidation of the Cr with increasing melt pool / vapor temperature.

- It is also observed that NiI/CrI line intensity ratio has a proportional relationship with the dimensionless number. This is attributable to the decrease of the population of the pure Cr atom in plume/plasma due to the promoted oxidation of Cr atoms with increasing temperature.

- The quantitative correlation predicting elemental composition during the DMD process has been developed by combining the two empirical correlations for the composition ratio and line intensity ratio. They have a proportional relationship because of the similar behavior with respect to the dimensionless number.

5.5 Numerical simulation of pulsed laser drilling

Numerical investigation of the effect of pulse format on the drilling performance has been carried out. Important findings and conclusions of the study are summarized below:

- A modulated beam using a short pulse and high beam intensity yielded higher drilling rates than the conventional pulsed laser under the same average power, and it is more effective in converting laser energy to material removal.

- In addition, the modulated beam produces the thinnest recast layer by creating a vaporization dominated process. For the same drilling time, the least tapered hole occurred when using a modulated beam. This is attributed to the fact that the exit hole size increased.

- Experiments carried out to validate the model showed an improvement in drilling performance for a modulated laser beam as well.

- Based on the results for comparison between the DP-11 pulse format and a double pulse format, increasing the number of pulses (or using the double pulse format) is more effective in enhancing drilling performance at relatively high power (or high beam intensity) levels; however, increasing the intensity of the laser beam (or using the DP-11 format) improves the drilling performance more than increasing the number of pulses at the relatively low power levels.

5.6 Future works

This research, along with its many advantages, has certain limitations too. The following are some of the limitations faced and some recommendations for future work.

- In this study, film deposition by pulsed laser deposition (PLD) was carried out on a small substrate (~1.5×1.5 cm^2). Increasing the deposition area (i.e. conventional silicon wafer size) and working to achieve uniform deposition on complex geometries are recommended for real application of this technique. Developing a multi-beam ablation system (either using multi-laser system or splitting one high power laser beam into two or three) will be necessary to provide a flexible process environment to achieve the above goals. This will also reduce processing time by increasing the deposition rate.

- By developing the single crystal (SC) deposition process for the Ni-base superalloy, this study opens up the possibility for the potential to utilize the PLD technique for repairing damaged single crystal turbine blades; however, there are some limitations in the current PLD setup for the industrial application of this technique. As mentioned earlier, real parts are generally much bigger than the substrates used in this study. They also have more complex geometry to deal with. Under the condition, heating the bigger part uniformly to an extreme temperature is a challenging task considering the limited space of the vacuum chamber. The development of a system that is able to combine extreme temperatures and bigger parts in a high quality vacuum would be one way to validate this method as an applicable technique.

- In laser drilling, the processing time used and hole size produced were acceptable for the industrial application; however, the recast layer produced still needs to be reduced further. Due to limitations in laser power and beam spot size in this study, percussion drilling is less effective in generation of the relatively large hole as compared with laser trepanning, but the percussion drilling generally produced much thinner recast layers. Using percussion drilling at high average powers (> 100 W) and the proper beam spot size is expected to produce holes with less recast and appropriate hole sizes.

- The plume/plasma generated in the DMD process is usually weak due to the use of the relatively low beam intensity. Below 10^5 W/cm^2 beam intensity, emission spectra was not detectable in this study. In this range, vaporization almost did not occur and only radiation from the glowing melt pool was seen. Using the spectral signal as a tool for composition monitoring seems to be improper for this range. Developing other

monitoring systems (i.e., measuring the melt pool temperature during the process) is probably necessary for the non-vaporization DMD process.

- In the numerical simulation, the effect of the plasma has not been taken into account in the model. Actual laser energy deposition on the hole wall can be reduced through the interaction between plasma and laser beam during the process (i.e., the inverse Bremsstrahlung effect). Incorporating plasma physics into the model is expected to improve the predictions.

- Finally, it is recommended that the depth of focus is considered in the model to reduce erroneous results for holes with a high aspect ratio.

APPENDICES

APPENDIX A

Analysis of variance (ANOVA) table for the results in figure 4.6.

Factor	Sum of squares (or Sum of variances)	Degree of Freedom	Mean of square (or Mean of variance)	F-value
Level	S_L=0.03738	DF_L=3	V_L=S_L/DF_L=0.012462	V_L/V_E=76.01
Error	S_E=0.00262	DF_E=16	V_E=S_E/DF_E=0.000164	

$$S_L = m\sum_{i=1}^{l}\left(\bar{x}_i - \bar{\bar{x}}\right)^2 \ , \quad S_E = \sum_{i=1}^{l}\sum_{j=1}^{m}\left(x_{ij} - \bar{x}_i\right)^2 \ , \quad DF_L = l\text{-}1, \text{ and } DF_E = l(m\text{-}1)$$

x_{ij}, $\bar{x}_i$, and $\bar{\bar{x}}$ are the individual response in level i, the mean of each level i, the overall mean, respectively. l (4) is the number of levels, and m (5) is the number of experiments within the level.

APPENDIX B

Raw data for figure 4.14

Experiment number	Drilling time (s)	Hole size (mm)		Hole taper (degree)	Recast layer thickness (mm)
		Entry	Exit		
1	18.55	0.593	0.131	2.206	0.301
2	11.83	0.552	0.049	2.403	0.214
3	10	0.573	0.021	2.639	0.164
4	8.99	0.620	0	2.961	0.118
5	15.04	0.560	0.123	2.088	0.290
6	24.66	0.573	0.170	1.922	0.282
7	6.93	0.671	0.033	3.046	0.215
8	7.58	0.576	0	2.749	0.232
9	8.8	0.565	0.105	2.198	0.150
10	5.96	0.617	0.051	2.701	0.120
11	27.8	0.735	0.243	2.350	0.145
12	13.54	0.799	0.096	3.353	0.113
13	8	0.545	0.138	1.944	0.124
14	11.38	0.637	0.1637	2.266	0.125
15	10.09	0.566	0.071	2.364	0.140
16	21.55	0.597	0.162	2.078	0.172

APPENDIX C

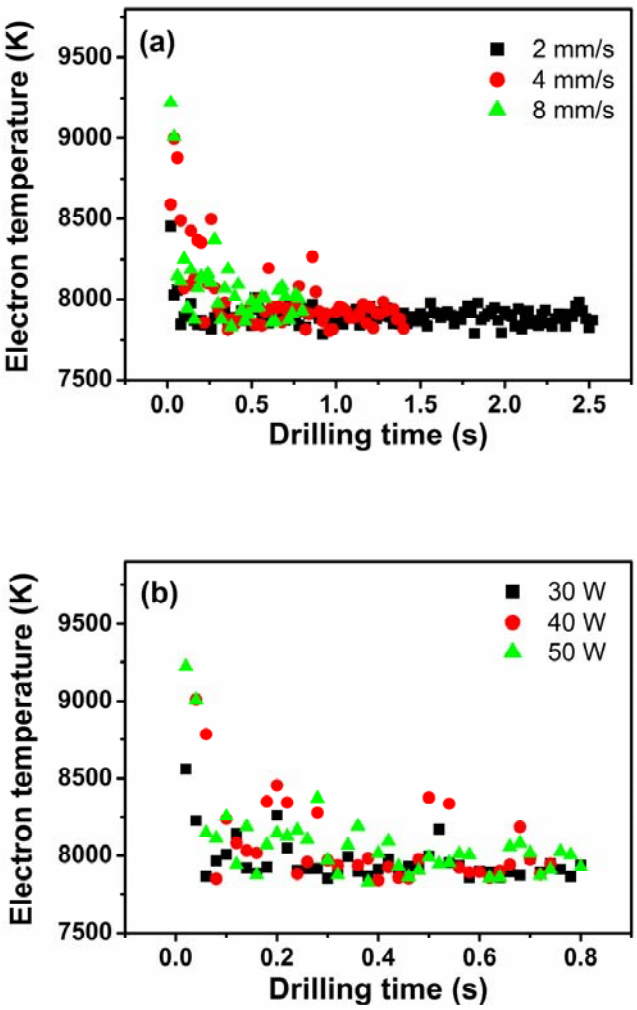

Electron temperature as a function of drilling time (a) for different speeds and (b) for different powers.

BIBLIOGRAPHY

[1] William M. Steen. *Laser Material Processing*. Springer, 2005.

[2] Marvin J. Weber. *Handbook of Laser Wavelengths*. CRC Press, 1999.

[3] John C. Ion. *Laser Processing of Engineering Materials*. Elsevier Butterworth-Heinemann, 2005.

[4] J. Mazumder. Overview of melt dynamics in laser processing. *Opt. Eng.*, 30(8):1208-1219, 1991.

[5] D. Dijkkamp, T. Venkatesan, X. D. Wu, S. A. Shaheen, N. Jisrawi, Y. H. Min-Lee, W. L. McLean and M. Croft. Preparation of Y-Ba-Cu oxide superconductor thin films using pulsed laser evaporation from high T_c bulk material. *Appl. Phys. Lett.*, 51(8):619-621, 1987.

[6] J.M. Blocher, Jr. Structure/property/process relationships in chemical vapor deposition CVD. *J. Vac. Sci. Technol.*, 11(4):680-684, 1974.

[7] W.A. Bryant. The fundamentals of chemical vapour deposition. *J. Mater. Sci.*, 12(7):1285-1306, 1977.

[8] Guy Antou, Ghislain Montavon, Francoise Hlawka, Alain Cornet and Christian Coddet. Characterizations of the pore-crack network architecture of thermal-sprayed coatings. *Mater. Charac.*, 53(5):361-372, 2004.

[9] C. Batista, A. Portinha, R.M. Ribeiro, V. Teixeira, M.F. Costa and C.R. Oliveira. Morphological and microstructural characterization of laser-glazed plasma-sprayed thermal barrier coatings. *Surf. Coat. Technol.*, 200(9):2929– 2937, 2006.

[10] J.T.M. De Hosson, J. Hooijmans and R. Popma. Sintering behaviour of nanoceramic coatings. *Surf. Eng.*, 16(3):245-249, 2000.

[11] A.A. Voevodin, J.G. Jones and J.S. Zabinski. Structural modification of single-axis-oriented ytrria-stabilized-zriconia films under zirconium ion bombardment. *Appl. Phys. Lett.*, 78(6):730-732, 2001.

[12] Y. Iijima, M. Hosaka, N. Tanabe, N. Sadakata, T. Saitoh, O. Kohno and K. Takeda. Growth structure of yttria-stabilized-zirconia films during off-normal ion-beam-assisted deposition. *J. Mater. Res.*, 13(11):3106-3112, 1998.

[13] N. Sonnenberg, A.S. Longo, M.J. Cima, B.P. Chang, K.G. Ressler, P.C. Mclntyre and Y.P. Liu. Preparation of biaxially aligned cubic zirconia films on pyrex glass substrates using ion-beam assisted deposition. *J. Appl. Phys.*, 74(2):1027-1033, 1993.

[14] Teiichi Kimura and Takashi Goto. Thermal conductivities of yttria-stabilized zirconia films measured by a laser-heating AC method. *Surf. Coat. Technol.*, 198:129-132, 2005.

[15] J.W. Lee, T.E. Schlesinger, A.K. Stamper, M. Migliuolo, D.W. Greve and D.E. Laughlin. Characterization of yttria-stabilized zirconium oxide buffer layers for high-temperature superconductor thin films. *J. Appl. Phys.*, 64(11):6502-6504, 1988.

[16] J.C. Delgado, F. Sanchez, R. Aguiar, Y. Maniette, C. Ferrater and M. Varela. ArF and KrF excimer laser deposition of yttria-stablized zirconia on Si(100). *Appl. Phys. Lett.*, 68(8):1048-1050, 1996.

[17] S.B. Qadri, J.S. Horwitz, D.B. Chrisey, E.P. Donovan and E.F. Skelton. Pulsed laser deposition and characterization of ZrO_2-Al_2O_3 films. *Surf. Coat. Technol.*, 86-87:149-152, 1996.

[18] R. Aguiar, V. Trik, F. Sanchez, C. Ferrater and M. Varela. Effects of wavelength, deposition rate and thickness on laser ablation deposited YSZ films on Si(100). *Thin Solid Films*, 304:225-228, 1997.

[19] C.H. Lei, G. Van Tendeloo, M. Siegert, J. Schubert and Ch. Buchal. Structural investigation of the epitaxial yittria-stabilized zirconia films deposited on (001) silicon by laser ablation. *J. Cryst. Growth*, 222:558-564, 2001.

[20] Douglas B. Chrisey and Graham K. Hubler. *Pulsed Laser Deposition of Thin Films*. John Wiley and Sons, Inc., 1994.

[21] C.Y. Yeo, S.C. Tam, S. Jana and Michael W.S. Lau. A technical review of the laser drilling of aerospace materials. *J. Mater. Process. Technol.*, 42:15-49, 1994.

[22] Todd J. Rockstroh, Doug Scheidt and Clarence Ash. Advances in laser drilling of turbine airfoils. *Industrial Laser Solutions for Manufacturing*, 17:8, 2002.

[23] K.T. Voisey and T.W. Clyne. Laser drilling of cooling holes through plasma sprayed thermal barrier coatings. *Surf. Coat. Technol.*, 176:296-306, 2004.

[24] J. Mazumder, D. Dutta, N. Kikuchi and A. Ghosh. Closed loop direct metal deposition: art to part. *Opt. Lasers Eng.*, 34:397-414, 2000.

[25] G.P. Dinda, A.K. Dasguta, and J. Mazumder. Laser aided direct metal deposition of Inconel 625 superalloy: Microstructural evolution and thermal stability. *Mater. Sci. Eng. A*, 509:98-104, 2009.

[26] L. Thivillon, Ph. Bertrand, B. Laget, and I. Smurov. Potential of direct metal deposition technology for manufacturing thick functionally graded coatings and parts for reactors components. *J. Nucl. Mater.*, 385(2):236-241, 2009.

[27] John F. Ready. *Effects of High Power Laser Radiation*. Academic Press Inc., New York, 1971.

[28] C. Argón and J.A. Aguilera. Characterization of laser induced plasmas by optical emission spectroscopy: A review of experimental and methods. *Spectrochim. Acta Part B*, 63: 893-916, 2008.

[29] R.W. Guard and J. H. Westbrook. Alloying behavior of Ni_3Al (γ' Phase). *Trans. Metall. Soc. AIME*, 215:807-814, 1959.

[30] Paul F. Jacobs. Aerospace Applications of Precision Trepanning. *Proc. of ICALEO '08*, Temecular, CA, Oct 20-23, 2008.

[31] C.L. Chan and J. Mazudmer. One-dimensional steady-state model for damage by vaporization and liquid expulsion due to laser-material interaction. *J. Appl. Phys.*, 62(11):4579-4586, 1987.

[32] Guenter Reisse, Steffen Weissmantel, Bernd Keiper and Ulrike Broulik. Deposition of optical coatings by pulsed laser ablation. *Appl. Surf. Sci.*, 96-98:752-759, 1996.

[33] J. Gottmann and E.W. Kreutz. Pulsed laser deposition of alumina and zirconia thin films on polymers and glass as optical and protective coatings. *Surf. Coat. Technol.*, 116-119:1189-1194, 1999.

[34] Ashok Kumar, L. Ganapathi, S.M. Kanetkar and J. Narayan. Single-chamber, in situ processing of superconducting $YBa_2Cu_3O_{7-\delta}$ thin films on stainless steel with yttria-stabilized zirconia buffer layer. *J. Appl. Phys.*, 69(4): 2410-2413, 1991.

[35] K.Y. Chen, G.J. Salamo, S. Afonso, X.L. Xu, Y.Q. Tang, Q. Xiong, F.T. Chan and L.W. Schaper. Fabrication of biaxially aligned $YBa_2Cu_3O_{7-x}$ thin films on glass substrates. *Physica C*, 267:355-360, 1996.

[36] J. Zhu and Z.G. Liu. Dielectric properties of YSZ high-*k* thin films fabricated at low temperature by pulsed laser deposition. *Mater. Lett.*, 57:4297– 4301, 2003.

[37] Hyo-Sok Ahn, Jang-Yup Kim and Dae-Soon Lim. Tribological behavior of plasma-sprayed zirconia coatings. *Wear*, 203-204:77-87, 1997.

[38] D.W. Stollberg, J.M. Hampikian, L. Riester and W.B. Carter. Nanoindentation measurements of combustion CVD Al_2O_3 and YSZ films. *Mater. Sci. Eng. A*, 359:112-118, 2003.

[39] Azar Nazeri and Syed B. Qadri. Alumina-stabilized zirconia coatings for high-temperature protection of turbine blades. *Surf. Coat. Technol*., 86-87:166-169, 1996.

[40] D.D. Hass, A.J. Slifka and H.N.G. Wadley. Low thermal conductivity vapor deposited zirconia microstructures. *Acta Mater.*, 49:973-983, 2001.

[41] Huang Chen, Xiaming Zhou and Chuanxian Ding. Investigation of the thermomechanical properties of a plasma-sprayed nanostructured zirconia coating. *J. Eur. Ceram. Soc.*, 23:1449-1455, 2003.

[42] Stephen Poulston, Roger A. Bennett, Paolo Faraldi, Timothy I. Hyde, Marco F. Pidria, Valerie Houel and Alison Wagland. Characterization of protective coatings for planar automotive gas sensors. *Sens. Actuat. B*, 110:209-217, 2005.

[43] A.S. Kao. Comparison of zirconia thin films sputtered from metal and compound targets by reactive ion-beam process. *J. Appl. Phys.*, 69(5):3309-3315, 1991.

[44] Peng Li, Jason Carroll and Jyoti Mazumder. Room temperature growth of biaxially aligned yttria-stabilized zirconia films on glass substrates by pulsed-laser deposition. *J. Phys. D: Appl. Phys.*, 36:1605–1608, 2003.

[45] E. Vasco, L. Vazquez, M. Aguilo and C. Zaldo. Epitaxial growth of Y-stabilized zirconia films on (100)InP substrates by pulsed laser deposition. *J. Cryst. Growth*, 209:883-889, 2000.

[46] F. Kokai, K. Amano, H. Ota, Y. Ochiai and F. Umemura. XeCl laser ablative deposition and characterization of yttria-stabilized zirconia thin films on glass and CeO_2-Sm_2O_3. *J. Appl. Phys.*, 72 (2):699-704, 1992.

[47] A.P. Caricato, G. Barucca, A. Di Cristoforo, G. Leggieri, A. Luches, G. Majni, M. Martino and P. Mengucci. Excimer pulsed laser deposition and annealing of YSZ nanometric films on Si substrates. *Appl. Surf. Sci*., 248:270-275, 2005.

[48] S.J. Wang, C.K. Ong, S.Y. Xu, P. Chen, W.C. Tjiu, J.W. Chai, A.C. Huan, W.J. Yoo, J.S. Lim, W. Feng and W.K. Choi. Crytalline zirconia oxide on silicon as alternative gate dielectrics. *Appl. Phys. Lett.*, 78(11):1604-1606, 2001.

[49] J. Gottmann, A. Husmann, T. Klotzbucher and E.W. Kreutz. Optical properties of alumina and zirconia thin films grown by pulsed laser deposition. *Surf. Coat. Technol*., 100-101:415-419, 1998.

[50] H. Sankur, J. Denatale, W. Gunning and J.G. Nelson. Dense crystalline ZrO_2 thin films deposited by pulsed-laser evaporation. *J. Vac. Sci. Technol. A*, 5(5):2869-2874, 1987.

[51] W. T. Loomis, T. W. Freeman and D. L. Sponseller. The Influence of Molybdenum on the phase in experimental nickel-base superalloys. *Metall. Trans*., 3: 989-1000, 1972.

[52] Shouichi Ochiai, Yoshihiro Oya and Tomoo Suzuki. Alloying behavior of Ni_3Al, Ni_3Ga, Ni_3Si and Ni_3Ge. *Acta metal.*, 32(2):289-298, 1984.

[53] A. Onyszko, K. Kubiak and J. Sieniawski. Turbine blades of the single crystal nickel based CMSX-6 superalloy, *J. Achiev. Mater. Manuf. Eng.*, 32(1):66-69, 2009.

[54] M. Gäumann, C. Bezencon, P. Canalis and W. Kurz. Single-crystal laser deposition of superalloys: processing-microstructure maps. *Acta mater.*, 49:1051-1062, 2001.

[55] L. Felberbaum, K. Voisey, M. Gäumann, B. Viguier and A. Mortensen. Thermal fatigue of single-crystalline superally CMSX-4: a comparison of epitaxial laser-deposited material with the base single crystal. *Mater. Sci. Eng. A*, 299:152-156, 2001.

[56] C. Bezencon, A. Schnell and W. Kurz. Epitaxial deposition of MCrAlY coatings on a Ni-base superalloy by laser cladding. *Scrip. Mater.*, 49:705-709, 2003.

[57] R.K. Singh, Deepika Bhattacharya, S. Sharan, P. Tiwari and J. Narayan. Fabrication of Ni-Al thin films by the pulsed laser deposition. *J. Mater. Res.*, 7 (10):2639-2642, 1992.

[58] R. Banerjee, G.B. Thompson, P.M. Anderson and H.L. Fraser. Sputter deposited nanocrystallyne Ni-25Al alloy thin films and Ni/Ni_3Al multilayers. *Thin Solid Films*, 424:93-98, 2003.

[59] P.de Almeida, R. Schäublin, A. Almazouzi, M. Victoria and F. Lévy. Microstructure and growth modes of stoichiometric NiAl and Ni_3Al thin films deposited by r.f.-magnetron sputtering. *Thin Solid Films*, 368: 26-34, 2000.

[60] Ulrich Klug. Pulsed Laser Deposition of Ni-Al Based Single Crystal Superalloys. *Master Thesis*, 2003, University of Michigan, Department of Mechanical Engineering.

[61] Joonghan Shin and J. Mazumder. Deposition of the Ni-base superalloy films by pulsed excimer laser. *Proc. of ICALEO '07*, Orlando, FL, Oct 29- Nov 1, 2007.

[62] C. R. M. Grovenor, H. T. G. Hentzell and D. A. Smith. The Development of Grain Structure during Growth of Metallic Films. *Acta metal.*, 32(5):773-781, 1984.

[63] K. L. Moazed, in J. C. Anderson (ed.). *The Use of Thin Films in Physical Investigations*. p.203. Academic Press Inc., New York, 1963.

[64] L.I. Maissel and R. Glang. *Hand Book of Thin Film Technology*. MaGraw-Hill, Inc., New York, 1970.

[65] M. Ghoreishi, D.K.Y. Low and L. Li. Comparative statistical analysis of hole taper and circularity in laser percussion drilling. *Int. J. Mach. Tool. Manuf.*, 42:985-995, 2002.

[66] S. Bandyopadhyay, J.K. Sarin Sundar, G. Sundararajan and S.V. Joshi. Geometrical features and metallurgical characteristics of Nd:YAG laser drilled holes in thick IN718. *J. Mater. Process. Technol.*, 127:83-95, 2002.

[67] A.H. Wang, W.Y. Wang, Z.K. Bai, C.S. Xie, D.W. Zeng and W.L. Song. YAG laser percussion drilling of a functional multi-layer thin plate. *Opt. Laser Tech.*, 39:840–845, 2007.

[68] N. Masmitai and P.K. Philip. Investigations on laser percussion drilling of some thermoplastic polymers. *J. Mater. Process. Technol.*, 185:198-203, 2007.

[69] Wen-Tung Chien and Shiann-Chin Hou. Investigating the recast layer formed during the laser trepan drilling of Inconnel 718 using the Taguchi method. *Int. J. Adv. Manuf. Technol.*, 33:308-316, 2007.

[70] Qiang Li, Yijun Zheng, Zhiyong Wang and Tiechuan Zuo. A novel high-peak power double AO Q-switches pulse Nd:YAG laser for drilling. *Opt. Laser Tech.*, 37:357–362, 2005.

[71] A. Corcoran, L. Sexton, B. Seanman, P. Ryan and G. Byrne. The laser drilling of muti-layer aerospace material systems. *J. Mater. Process. Technol.*, 123:100-106, 2002.

[72] D.K.Y. Low, L. Li and P.J. Byrd. The effects of process parameters on spatter deposition in laser percussion drilling. *Opt. Laser Tech.*, 32:347-354, 2000.

[73] D.K.Y. Low, L. Li and A.G. Corfe. Effects of assist gas on the physical characteristics of spatter during laser percussion drilling of NIMONIC 263 alloy. *Appl. Surf. Sci.*, 154–155:689–695, 2000.

[74] S.C. Tam, C.Y. Yeo, S. Jana, Michael W.S. Lau, Lennie E.N. Lim, L.J. Yang and Yusoff Md Noor. Optimization of laser deep-hole drilling of Inconel 718 using the Taguchi method. *J. Mater. Process. Technol.*, 37:741-757, 1993.

[75] M. Li, T.P. Duffey and J. Mazumder. Spatially and temporally resolved temperature measurements of plasma generated in percussion drilling with a diode-pumped Nd:YAG laser. *J. Appl. Phys.,* 84(8):4122-4127, 1998.

[76] J. Thomas Knudtson, William B. Green and David G. Sutton. The UV-visible spectroscopy of laser-produced aluminum plasmas. *J. Appl. Phys.*, 61(10):4771-4780, 1987.

[77] F.J. Gordillo-Vazquez, A. Perea, J.A. Chaos, J. Gonzalo and C.N. Afonso. Temporal and spatial evolution of the electronic density and temperature of the plasma produced by laser ablation of $LiNbO_3$. *Appl. Phys. Lett.*, 78(1):7-9, 2001.

[78] V. Kumar and R.K. Thareja. Studies of eximer-laser-produce copper plasma in the presence of background gas. *J. Appl. Phys*., 67(7):3260-3263, 1990.

[79] H.C. Liu, X.L. Mao, J.H. Yoo and R.E. Russo. Early phase laser induced plasma diagnostics and mass removal during single-pulse laser ablation of silicon. *Spectrochim. Acta Part B*, 54:1607-1624, 1999.

[80] M. Milan and J.J. Laserna. Diagnostics of silicon plasmas produced by visible nanosecond laser ablation. *Spectrochim. Acta Part B*, 56:275-288, 2001.

[81] Nek M. Shaikh, B. Rashid, S. Hafeez, Y. Jamil and M.A. Baig. Measurement of electron density and temperature of a laser-induced zinc plasma. *J. Phys. D:Appl. Phys.*, 39: 1384-1391, 2006.

[82] D. Lacroix, G. Jeandel and C. Boudot. Spectroscopic characterization of laser-induced plasma created during welding with a pulsed Nd:YAG laser. *J. Appl. Phys*., 81(10): 6599-6606, 1997.

[83] Sudhir Kum Tewari. *Plasma optical emission spectroscopy of laser cladding for process control and oxidation behavior of laser clad NbAl alloys*. PhD thesis, University of Illinois at Urbana-champaign, 1995.

[84] Louis St-Onge, Mohamad Sabsabi and Paolo Cielo. Quantitative analysis of additives in solid zinc alloys by laser-induced plasma spectrometry**.** *J. Anal. At. Spectrom.*, 12:997-1004, 1997.

[85] Q.L. Zhang, J.P. Zhang, C.Y. Liang, B.T. Li, X. Li, Q.L. Guo and G.S. Fu. Compositional analysis of ferroelectric films coated with carbon layer using laser-induced plasmas spectroscopy. *Appl. Surf. Sci*., 255(17):7669-7671, 2009.

[86] M. von Allmen. Laser drilling velocity in metals. *J. Appl. Phys.*, 47(12):5460-5463, 1976.

[87] A. Kar and J. Mazumder. Two-dimensional model for material damage due to melting and vaporization during laser irradiation. *J. Appl. Phys*., 68(8): 3884-3891, 1990.

[88] A. Kar, T. Rockstroh and J. Mazumder. Two-dimensional model for laser-induced materials damage: Effects of assist gas and multiple reflections inside the cavity. *J. Appl. Phys.*, 71 (6):2560-2569, 1992.

[89] P. Solana, P Kapadia, J.M. Dowden and P.J. Marsden. An analytical model for the laser drilling of metals with absorption within the vapour. *J. Phys. D: Appl. Phys.,* 32:942-952, 1999.

[90] C.F. Cheng, Y.C. Tsui and T.W. Clyne. Application of a three-dimensional heat flow model to treat laser drilling of carbon fibre composites. *Acta Mater.*, 46(12):4273-4285, 1998.

[91] J.C.J. Verhoeven, J.K.M. Jansen, R.M.M. Mattheij and W.R. Smith. Modeling laser induced melting. *Math. Comput. Modeling*, 37:419-437, 2003.

[92] R.K. Ganesh and A. Faghri. A generalized thermal modeling for laser drilling process-II. Numerical simulation and results. *Int. J. Heat Mass Transfer.*, 40(14):3361-3373, 1997.

[93] Yuwen Zhang and A. Faghri. Vaporization, melting and heat conduction in the laser drilling process. *Int. J. Heat Mass Transfer*, 42:1775-1790, 1999.

[94] Ram K. Ganesh, Wallace W. Bowley, Robert R. Bellantone and Yukap Hahn. A model for laser hole drilling in metals. *J. Comput. Phys.*, 125:161-176, 1996.

[95] H. Ki. *Modeling and measurement of process with liquid-vapor interface created by high power density lasers*. PhD thesis, University of Michigan at Ann Arbor, 2001.

[96] H. Ki, P. Mohanty and J. Mazumder. Modeling of high-density laser material interaction using fast level set method. *J. Phys. D: Appl. Phys.*, 34:364-372, 2001.

[97] S.Tin and T.M. Pollock. Stabilization of thermosolutal convective instabilities in Ni-based single-crystal superalloys: Carbide precipitation and rayleigh numbers. *Metall. Mater. Trans. A*, 34 (9):1953-1967, 2003.

[98] S. Osher and J.A. Sethian. Front propagating with curvature-dependent speed: algorithms based on Hamilton-Jacobi formulations. *J. Comput. Phys*., 79:12-49, 1988.

[99] C.J. Knight. Theoretical modeling of rapid surface vaporization with back pressure. *AIAA J*., 17(5):519-523, 1979.

[100] A. Bogaerts, Z. Chen, Rennat Gijbels and A. Vertes. Laser ablation for analytical sampling: What can we learn from modeling?. *Spectrochim. Acta Part B*, 58:1867-1893, 2003.

[101] Warren M. Rohsenow and J. P. Hartnett. *Hand book of heat transfer*, McGraw-Hill Inc., 1973.

[102] Kenneth C. Mills, Yehia M. Youssef, Zushu Li and Yuchu SU. Calculation of Thermophysical Properties of Ni-based Superalloys. *ISIJ International*, 46(5):623-632, 2006.

[103] D. N. Nikolaev, V. Ya. Ternovoi, A. A. Pyalling and A. S. Filimonov. Near-Critical-Point Thermodynamics from Shock Experiments with Porous Ni Samples. *Int. J. Thermophys*., 23(5):1311-1318, 2002.

[104] M. Schneider, L. Berthe, R. Fabbro and M. Muller. Measurement of Laser Absorptivity for Operating Parameters Characteristic of Laser Drilling Regime. *J. Phys. D: Appl. Phys*., 41:1-6, 2008.

[105] C. Domb. *The Critical Point*. Taylor & Francis, London, 1996.

[106] T. Yamamoto. *Synthesis and characterization of nanocrystalline Nb-aluminides by laser ablation technique*. PhD thesis, University of Illinois at Urbana-champaign, 1998.

[107] H. Chen, X. Zhou and C. Ding. Investigation of the thermomechanical properties of a plasma-sprayed nanostructured zirconia coating. *J. Eur. Ceram. Soc*., 23(9):1449-1455, 2003.

[108] The National Institute of Standards and Technology (NIST), NIST Atomic Line Data base, http://physics.nist.gov/PhysRefData/ASD/index.html.

[109] M.S. Dimitrijevic, T. Ryabchikova, L.C. Popovic, D. Shulyak and S. Khan. On the influence of Stark broadening on CrI lines in stella atmospheres. *A & A*, 435:1191-1198, 2005.

[110] G. Abdellatif and H. Imam. A study of the laser plasma parameters at different laser wavelengths. *Spectrochim. Acta Part B*, 57:1155–1165, 2002.

[111] Q.M. Wang, Y.J. Tang, M.H. Guo, P.L. Ke, J. Gong, C. Sun and L.S. Wen. Thermal shock cycling behavior of NiCoCrAlYSiB coatings on Ni-base superalloys: I. Accelerated oxidation attack. *Mater. Sci. Eng. A*, 406:337–349, 2005.

[112] Roger C. Reed. *The superalloys: fundamentals and applications*. Cambridge University Press, 2006.

[113] Lehane C. and Kwok H.S.. Enhanced drilling using a dual-pulse Nd:YAG laser. *Appl. Phys. A*, 73:45-48, 2001.

[114] C. Hartmann, A. Gillner, Ü Aydin, R. Noll, T. Fehr, C. Gehlen and R Poprawe. Investigation on laser micro ablation of metals using ns-multipulses. *J. Phys. Conference series*, 59:440-444, 2007.

[115] C. Hartmann, T. Fehr, M. Brajdic and A. Gillner. Investigation on Laser Micro Ablation of Steel Using Short and Ultrashort IR Multipulses. *JLMN-Journal of Laser micro/Nanoengineering*, 2(1):44-48, 2007.

[116] Forsman A.C., Banks P.S., Perry M.D., Campbell E.M., Dodell A.L. and Armas M.S.. Double-pulse machining as a technique for the enhancement of material removal rates in laser machining of metals. *J. Appl. Phys*., 98:1-6, 2005.